

**U.S. DEPARTMENT OF COMMERCE
National Technical Information Service
PB-272 054**

A Preliminary Description of Stresses in Railroad Rail

Battelle Columbus Labs, Ohio

Prepared for

Transportation Systems Center, Cambridge, Mass

Nov 76

PB 272 054

REPORT NO. FRA-ORD-76-294

**A PRELIMINARY DESCRIPTION OF STRESSES
IN RAILROAD RAIL**

Thomas G. Johns
Kent B. Davies

Battelle's Columbus Laboratories
505 King Avenue
Columbus OH 43201



NOVEMBER 1976

INTERIM REPORT

DOCUMENT IS AVAILABLE TO THE U.S. PUBLIC
THROUGH THE NATIONAL TECHNICAL
INFORMATION SERVICE, SPRINGFIELD,
VIRGINIA 22161

Prepared for
**U.S. DEPARTMENT OF TRANSPORTATION
FEDERAL RAILROAD ADMINISTRATION
Research and Development
Washington DC 20590**

NOTICE

This document is disseminated under the sponsorship of the Department of Transportation in the interest of information exchange. The United States Government assumes no liability for its contents or use thereof.

NOTICE

The United States Government does not endorse products or manufacturers. Trade or manufacturers' names appear herein solely because they are considered essential to the object of this report.

1. Report No FRA-ORD-76-294		2. Government Accession No		3. Recipient's Catalog No	
4. Title and Subtitle A PRELIMINARY DESCRIPTION OF STRESSES IN RAILROAD RAIL				5. Report Date November 1976	
7. Author(s) Thomas G. Johns and Kent B. Davies				6. Performing Organization Code	
9. Performing Organization Name and Address Battelle's Columbus Laboratories* 505 King Avenue Columbus OH 43201				8. Performing Organization Report No DOT-TSC-FRA-76-23 G-6266-0101	
12. Sponsoring Agency Name and Address U.S. Department of Transportation Federal Railroad Administration Research and Development Washington DC 20590				10. Work Unit No. (TRAIS) RR619/R7323	
				11. Contract or Grant No DOT-TSC-1038	
				13. Type of Report and Period Covered Interim Report July - October 1975	
15. Supplementary Notes *Under contract to:				U.S. Department of Transportation Transportation Systems Center Kendall Square Cambridge MA 02142	
16. Abstract <p>One portion of the Federal Railroad Administration's (FRA) Track Performance Improvement Program is the development of engineering and analytic techniques required for the design and maintenance of railroad track of increased integrity and safety. Under the program management of the Transportation Systems Center (TSC), one portion of this program predicts the reliability of rail in track. A necessary requirement for the development of these techniques is the ability of determining the stress and strain history of the rails in service. This is necessary to form a more comprehensive basis for a quantitative understanding of flaw initiation and growth. This report is one of a series of reports that provide a comprehensive description of stresses in rail required for predicting the reliability of rail in track structures. It provides a description of stresses encountered in railroad rails compiled from information available in the literature before 1976.</p>					
17. Key Words Rail, Rail Stress, Stress, Flexural Stresses, Contact Stresses, Plastic Flow, Railroad Track			18. Distribution Statement DOCUMENT IS AVAILABLE TO THE U.S. PUBLIC THROUGH THE NATIONAL TECHNICAL INFORMATION SERVICE, SPRINGFIELD, VIRGINIA 22161		
19. Security Classif. (of this report) Unclassified		20. Security Classif. (of this page) Unclassified		21. No. of Pages 136	22. Price PC A07-A01

PRFFACE

This report presents the results of the literature review portion of a program on an Engineering Analysis of Stresses in Railroad Rails. It has been prepared by Bechtelle's Columbus Laboratories (BCL) under Contract DOT-TSC-1038 for the Transportation Systems Center (TSC) and the Department of Transportation. The program was conducted under the technical direction of Mr. Donald McConnell, Code 612, at the Transportation Systems Center.

This report is one of a series prepared to provide a comprehensive description of the stresses in rail required for predicting reliability of rail in track structures.

The cooperation and assistance of Mr. Donald McConnell, Mr. Roger Steele of TSC, Dr. Sam Sampath, Mr. Raymond E. Mesloh, and Mr. Robert H. Prause of BCL is gratefully acknowledged. The results reported are necessarily quite dependent on previous work which has been reported in the literature, and the authors are grateful to the several authors and publishers who granted permission for the use of copies of that material.

METRIC CONVERSION FACTORS

Approximate Conversions to Metric Measures			Approximate Conversions from Metric Measures					
Symbol	When You Know	Multiply by	To Find	Symbol	When You Know	Multiply by	To Find	Symbol
LENGTH								
m	meters	2.5	centimeters	cm	centimeters	0.04	inches	in
ft	feet	30	centimeters	in	inches	2.5	centimeters	cm
yds	yards	91	centimeters	m	meters	0.9	yards	yds
mi	miles	1.6	kilometers	km	kilometers	0.6	miles	mi
AREA								
sq ft	square feet	0.9	square centimeters	sq cm	square centimeters	11	square inches	sq in
sq yds	square yards	0.8	square meters	sq m	square meters	1.2	square yards	sq yds
sq mi	square miles	2.6	square kilometers	sq km	square kilometers	0.4	square miles	sq mi
acres	acres	0.4	hectares	hectares	hectares	2.5	acres	acres
MASS (weight)								
gms	grams	20	grams	gms	grams	0.035	ounces	oz
pkts	pounds	0.45	kilograms	kg	kilograms	2.2	pounds	pkts
short tons	short tons	0.9	tonnes (1000 kg)	tonnes	tonnes	1.1	short tons	short tons
VOLUME								
liters	liters	1.05	milliliters	ml	milliliters	0.03	fluid ounces	fl oz
ml	milliliters	16	milliliters	ml	milliliters	2.1	oz	oz
qt	quarts	0.95	liters	l	liters	1.06	quarts	qt
gal	gallons	3.8	liters	l	liters	0.26	gallons	gal
cu ft	cubic feet	0.03	liters	l	liters	36	cubic feet	cu ft
cu yds	cubic yards	0.76	cubic meters	cu m	cubic meters	1.3	cubic yards	cu yds
TEMPERATURE (cent)								
Fahrenheit temperature	5/9 (after subtracting 32)		Celsius temperature	C	Celsius temperature	9/5 (then add 32)	Fahrenheit temperature	F

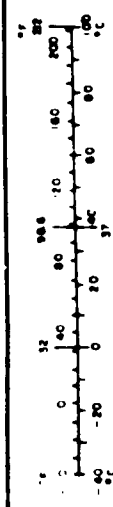


TABLE OF CONTENTS

	<u>Page</u>
1. INTRODUCTION.	1
1.1 General Nature of Rail Problems.	1
1.2 General Discussion of Stress Cycles in Rails/Description of Basic Load Histories in Rail Due to Rolling Loads.	4
1.3 Summary of Rail Stresses, Analyses and Measurement Techniques	7
1.3.1 Flexural Stresses	7
1.3.2 Thermal Stresses.	9
1.3.3 Contact Stresses.	9
1.3.4 Residual Stresses	10
2. FLEXURAL STRESSES	12
2.1 Basic Flexural Action.	12
2.2 Stresses Due to Vertical Bending	12
2.2.1. Analytical Treatments.	12
2.2.2. Comparison Between Calculated and Experimental Results	27
2.3 Lateral Bending and Twist.	27
2.3.1 Eccentric Vertical Load	27
2.3.2 Stresses Due to Lateral Loads	32
2.4 Dynamic Flexural Stresses in Rails	34
2.4.1 Analytical Treatments	34
2.4.2 Comparison Between Calculated and Experimental Results	38
3. STRESS CONCENTRATIONS--WEB AND FILLET STRESSES.	45
3.1 Introduction	45
3.2 Summary of Previous Experimental Studies	45
3.3 Calculation of Fillet Stresses	52
3.4 Effects of Wear on Web and Fillet Stresses	52
4. THERMAL STRESSES.	60
4.1 Discussion	60
4.2 Effect on Total Stress State	63
5. CONTACT STRESSES IN RAIL.	65
5.1 Normal Elastic Contact Stresses.	65

TABLE OF CONTENTS (Continued)

	Page
5.2 Surface Traction or Elastic Shearing Forces	82
6. RESIDUAL STRESSES IN RAILS	90
6.1 Development of Residual Stresses in Rail Heads	90
6.2 Determination of Stresses Due to Plastic Deformation	93
7. A DESCRIPTION OF METHODOLOGY FOR THE DEVELOPMENT OF A RAIL STRESS MODEL	110
7.1 Full Rail Model	110
7.2 Normal Contact Stress Model	112
7.3 Elastic and Elastic-Plastic Head Models	114
7.4 Residual Stress Shakedown Model	114
7.5 Finite Element Head Model	115
REFERENCES	118
APPENDIX - REPORT OF INVENTIONS	125

LIST OF TABLES

<u>Table</u>	<u>Page</u>
1. Types of Most Commonly Encountered Rail Defects.	2
2. Typical Maximum and Minimum Stresses in a 132-lb Rail Head Under a Vertical Wheel Load of 19,000 lb	6
3. Typical Data for Characteristic Lengths for X_1 and X_2	17
4. Lundgren's Input Variables	23
5. Maximum Range of Measured Stress in the Upper Fillet Area.	56
6. Theoretical Shakedown Load for Various Surface Traction T.	100

LIST OF FIGURES

<u>Figure</u>	<u>Page</u>
1. Stress History in Rail Head Due to Rolling Load.	5
2. Infinite Rail with Central Point Load.	13
3. Maximum Allowable Tie Spacing For Winkler Model.	15
4. Normalized Rail Deflection and Bending Moment Curves	15
5. Depressed end Lift Off Regions at Various Wheel Loads Using the Winkler Theory	20
6. Finite Element Track Models.	22
7. Geometrical Configuration in PSA Simulation.	24
8. Longitudinal Bending Stress from 30,000-lb Vertical Load P.S. 130-lb Rail in Track	26
9. Comparison of Calculated Longitudinal Stresses with Experimental Results	28
10. Experimental Longitudinal Stress Distribution Under Central Load	28
11. Experimental Longitudinal Stress Distribution Under Eccentric Load	29
12. Experimental Longitudinal Stress Distribution Under Inclined Load.	29
13. Rail with Eccentric Vertical Load.	30
14. Analysis of Rail Subjected to Eccentric Vertical Loading	30
15. Additional (Dynamic) Deflection Produced by Flat Spot on Wheel or Low Spot on Rail	36
16. Dynamic Compliance Measured for Various Track Stiffnesses.	39

LIST OF FIGURES (Continued)

<u>Figure</u>	<u>Page</u>
17. Location of Strain Gages on Rails.	41
18. Profiles of the Three Lengths of Ground Flat Spots on a 33-in. Wheel.	41
19. Typical Records of Rail Stress at 10 and 80 MPH with Round Wheels - Full Load, 100-lb Rail.	42
20. Typical Records of Rail Stress at 6 and 65 MPH with 4-1/2-in. Flat Spot-Full Load, 100-lb Rail.	42
21. Longitudinal Stress in Rail Base Due to Flat Spots at Three Ranges of Speed and Three Loads - 100-lb and 131-lb Rails	43
22. Simultaneous Stresses in the Base and in the Inner and Outer Web Faces of a 100-lb N.H. Rail As a 33-inch Wheel With a 2-1/2-inch Flat Spot Moves Past the Gages	44
23. Web Vertical Stresses in PS130 and PS131 Rail.	46
24. Connected Photoelastic Determination of Tangential Stress in PS130 Rail	47
25. Web and Fillet Stress in 112-lb RE Rail.	48
26. Measured Stresses in 112-lb RE Rail Over Middle of Tie For Static Load of 40,000-lb Controlled Loading Condi- tions as Indicated on Rail Head.	50
27. Measured Stresses in 131-lb RE Rail Over Middle of Tie For Static Load of 40,000-lb Controlled Loading Conditions as Indicated on Rail Head.	51
28. Stress Concentration Factors for Bending and Direct Stress	53
29. Bending Moment and Direct Stress For Rail Section.	54
30. Measured Web and Fillet Stresses in the Web of 100 RE Rail With Concentric and Eccentric Loading	57
31. Measured Web and Fillet Stresses in the Web of 115 RE Rail With Concentric and Eccentric Loading	57
32. Measured Web and Fillet Stresses in the Web of 132 RE Rail with Concentrated Eccentric Loading	58
33. Measured Web and Fillet Stresses in the Web of 140 RE Rail with Concentric and Eccentric Loading	58
34. Comparison of Measured and Calculated Vertical Stresses at Gage Locations 2a - 12a in the Upper Web Fillets With 3/4-inch Eccentric Load of 40,000-lb.	59
35. Rail Model for Thermal Elongation.	61
36. Thermal Stress as a Function of Temperature Variation for Total Restraint.	64
37. Stresses Developed in 132-lb RE Rail Head at Depth of 0.15 Inch Due to 33-Inch Diameter Wheel and Wheel Load of 19,000 lb	64

LIST OF FIGURES (Continued)

Figure	Page
38. Wheel/Rail Contact as Elliptical in Contact	67
39. Stresses and Deflections Between A Wheel and Rail in Contact	69
40. Elastic Stress Distribution in Rail Head Under the Wheel.	71
41. Typical Measured and Theoretical Static-Strain Dis- tribution Below the Surface of Contact Along the Line $y = 0$ and $z/a = 0.236$	72
42. Maximum Compressive, Octahedral Shear, and Alternating Transverse Shear Stress for New 33-Inch Diameter Wheel and Rail Having 10-Inch Crown Radius	72
43. Three-Dimensional Model of Rail Head After Martin and Hay.	75
44. Elastic Stress Distribution From Martin and Hay and Analytical Solutions	76
45. Stress Contours for 132-lb RE Rail and 19,000-lb Wheel Load	77
46. Frocht Photoelastic Model and Test Setup of 132-lb RE Rail and 33-Inch Diameter Worn Wheel	78
47. Elastic Stress Distribution From Frocht and Analytical Half Space Solutions (30,000 lb Wheel Load, 132-lb RE Rail, 33-Inch Worn Wheel).	90
48. ORE Photoelastic Model of U36 Rail	81
49. Elastic Stress Distribution From ORE Photoelastic Models	81
50. Form of Surface Contact Stresses and Subsurface Shear for a Misaligned Roller and Rail	93
51. Form of the Shear Stress Distribution Found by Carter For Rolling Contact.	83
52. Influence of the Component of Friction in the Partial Slip of Cylinders.	83
53. Measured and Theoretical Surface Traction Stresses	85
54. Lines of Constant Octahedral Shear Stress τ_G/σ_{max} Beneath the Contact Area Between the Cylinders.	86
55. Lines of Constant Octahedral Shear Stress, τ_G/σ_{max} Beneath the Contact Area Between the Spheres	87
56. Longitudinal, Vertical, and Transverse Residual Stress in New and Used Rail Beneath the Centerline of Contact . .	91
57. Hardness Profile of Nonheat-Treated Standard Rail Specimen No. 828	92

LIST OF FIGURES (Continued)

<u>Figure</u>	<u>Page</u>
58. Residual Longitudinal Stress For Analytical and Experimental Rail Models	94
59. Stress Field at Shakedown Limit in Cylinder Contacting A Plane.	97
60. Variations of the Stress Components (a) σ_x , (b) σ_y , (c) σ_z , and (d) τ_{xy} With x at a Constant Depth, $y = -a$, and Load $P_0 = 5.5k \cdot xy$	98
61. Buildup of Residual Stress $(\sigma_x)_r$ and $(\sigma_z)_r$ with Repeated Passage of the Load.	99
62. Critical Residual Stresses Necessary to Produce Shakedown.	101
63. Stress Ratio Plotted Against Depth Comparison of Experimental Results with Theoretical Predictions.	101
64. Contact Stress Distribution Between Indentor Having Surface Contours in Various Stages of Deformation or Wear $W=r^a$	104
65. Finite Element Model of Rail Head (ORE C53/RP9).	105
66. Residual Stress as a Function of Depth Below Surface.	106
67. Residual Stresses Developed Using (a) Stablien, (b) Rosenthal-Norten, (c) ORE Hole Drilling Technique	107
68. Residual Stress Components in 132-lb RE Rail Head, $P = 19,000$ lb, $K = 55,000$ Psi.	108
69. Buildup of σ_x Residual Stress at Node A.	109
70. Flow Diagram for Track Structures Reliability Model.	111
71. Three-Dimensional Finite-Element Mesh of Rail End.	113
72. Logic Diagram of Loading Sequences for Residual Stress Rail Model.	116
73. Central Rail Defects	117

LIST OF FIGURES (Continued)

<u>Figure</u>	<u>Page</u>
58. Residual Longitudinal Stress for Analytical and Experimental Rail Models	94
59. Stress Field at Shakedown Limit in Cylinder Contacting A Plane.	97
60. Variations of the Stress Components (a) σ_x , (b) σ_y , (c) σ_z , and (d) τ_{xy} With x at a Constant Depth, $y^x = -a$, and Load $P_0 = 5.5k^xy$	98
61. Buildup of Residual Stress $(\sigma_x)_r$ and $(\sigma_z)_r$ with Repeated Passage of the Load.	99
62. Critical Residual Stresses Necessary to Produce Shakedown.	101
63. Stress Ratio Plotted Against Depth Comparison of Experimental Results with Theoretical Predictions.	101
64. Contact Stress Distribution Between Indentor Having Surface Contours in Various Stages of Deformation or Wear $w=r^a$	104
65. Finite Element Model of Rail Head (ORE C53/RP9).	105
66. Residual Stress as a Function of Depth Below Surface.	106
67. Residual Stresses Developed Using (a) Stablien, (b) Rosenthal-Norten, (c) ORE Hole Drilling Technique	107
68. Residual Stress Components in 132-lb RE Rail Head, $P = 19,000$ lb, $K = 55,000$ Psi.	108
69. Buildup of σ_x Residual Stress at Node A.	109
70. Flow Diagram for Track Structures Reliability Model.	111
71. Three-Dimensional Finite-Element Mesh of Rail End.	113
72. Logic Diagram of Loading Sequences for Residual Stress Rail Model.	116
73. Central Rail Defects	117

1. INTRODUCTION


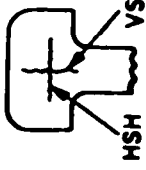
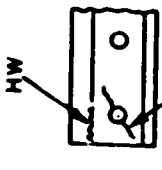

1.1 GENERAL NATURE OF RAIL PROBLEMS

In recent years, railroads in the United States have annually experienced over 800 derailments attributable to broken rails and which have resulted in over 60 million dollars of damage each year^[1]. These derailments occur despite a substantial inspection program by the railroads and contract inspection services which collectively locate and identify nearly 200,000 defective rails annually^[2]. The replacement of these flawed rails involves removal of over 100,000 tons of rail. In addition, old rail is being replaced at the rate of nearly 700,000 tons per year^[3]. Despite these actions, the rate of occurrence of flawed rail is increasing yearly. Furthermore, rail failures rank as one of the single most severe causes of accidents^[4].

The types of defects most commonly encountered are summarized in Table 1 with a ranking of the percentage cause of derailments and frequency of detection^[5]. The actions required by Federal regulation^[6] for train operation until a defective rail is replaced are also listed. Rail end failures represent the most troublesome category but may not be the most dangerous in terms of derailments. FRA statistics^[1] suggests that approximately 22 percent of all derailments result from failure of one or more components at the joint region as opposed to the 17 percent shown in the table for rail failure alone at the joint region. Transverse fissures are detected less frequently but appear to account for a disproportionately large number of derailments. Vertical/horizontal split heads and detail/compound fractures, which are characterized by a crack which travels some distance along the rail before it turns to run transversely, constitute the last major category with a severity between that of the transverse fissure and that of the rail end defects.

The behavior of cracks under the railroad load environment is not well documented. However, what information is readily available^[7] suggests that a transverse fissure may grow slowly to be somewhat more than 20 percent of the rail head cross section area before growth becomes rapid and rupture of the entire rail occurs suddenly. Sometimes more than one transverse fissure will develop in a given rail. In contrast, bolt hole cracks have been reported to have 'slow growth' crack lengths ranging from fractions of an inch up to several inches in length^[8]. The time required to grow to four or more inches in length

TABLE 1. TYPES OF MOST COMMONLY ENCOUNTERED RAIL DEFECTS

DEFECT	LOCATION/SHAPE	DETAIL/Δ DETECT	SIZE	ACTION REQUIRED UNTIL DEFECTIVE RAIL IS REPLACED
TRANSVERSE FISSURE		24%/12%	HEAD AREA (a) < 100% (b) 100% (+)	10 mph MAX. VISUAL SUPERVISION
VERTICAL/ HORIZONTAL SPLIT HEAD		26%/18%	LENGTH (a) < 2"	50 mph OR LESS* ; INSPECT IN 90 DAYS
			(b) 2" TO 4"	30 mph OR LESS* ; INSPECT IN 30 DAYS
			(c) > 4"	10 mph MAX.
BOLT HOLE/ HEAD WEB SEPARATION		17%/56%	(d) CHUNK MISSING	VISUAL SUPERVISION
			LENGTH (a) < 1/2"	50 mph OR LESS* ; INSPECT IN 90 DAYS
			(b) 1/2" TO { 3" (HW) - 1/2" (BH)	30 mph OR LESS* ; INSPECT IN 30 DAYS
			(c) > { 3" (HW) - 1/2" (BH)	10 mph MAX.
DETAIL FRACTURE/ COMPOUND FISSURE		8%/5%	(d) CHUNK MISSING	VISUAL SUPERVISION
			HEAD AREA (a) < 20% (DF)	30 mph OR LESS* UNTIL JOINT BARS ARE APPLIED AND THEN 50 mph OR LESS*
			20% TO 100% (DF) < 100% (DF)	10 mph OR LESS* UNTIL JOINT BARS ARE APPLIED AND THEN 50 mph OR LESS* 10 mph MAX.
			(b) 100% (+)	VISUAL SUPERVISION

Δ SPERRY DATA, 1967-1973 AVG.
* SET BY CLASS OF TRACK

appears to be as much as several years in some cases and can depend strongly on the mechanical integrity of the joint, rail support conditions, and location of the rail in the track (i.e. on curves). The vertical split head may grow to be several feet in length before it can be observed on the surface of the rail head [7]. Once an internal crack has reached a free surface, the growth rate usually will increase but rail rupture will not necessarily occur immediately.

Understanding the growth of rail flaws is dependent on knowledge of both the material characteristics of rail steels and the varying states of stress within the rail. The failure characteristics of high carbon steels, such as those employed in rail, are largely unknown. Some steels of this type show a strong effect of high stress intensity fatigue cycles on increasing apparent fracture toughness [9]. In addition, retardation effects have been observed in a number of alloys [10,11]. Retardation is influenced by such variables as stress intensity range, stress ratio, and number of cycles at high load.

Although the growth of cracks in rail steel in other than a Mode I manner has not been well established, a substantial interaction between Mode I and II types of loading on fracture has been observed for AISI 4340 steel [12]. In addition, shear fields acting in conjunction with tensile fields have been observed to have a disproportionately detrimental effect on crack growth rate in 6061-T6 [13]. Consequently, the development of a description of rail failure is dependent on an adequate description of the stress fields established within the rail by external loads and constrained thermal expansion and contraction.

Concern with the stresses in rail has resulted in numerous investigations, largely experimental in nature, over the last fifty years. Many of these studies are associated with the investigation of specific problems such as high head-web fillet stresses, which have subsequently been eliminated by redesign of the rail cross-section. Many of these laboratory and field experiments predate contemporary stress analysis techniques which could have provided for the interpretation and generalization of the developed data.

This report is one of the series of reports to provide a comprehensive description of the stresses in rail required for predicting reliability of rail in track structures. Contained herein is a description of stresses encountered in railroad rails in regions away from rail joints or in sections of continuously welded rails as compiled from information available in the

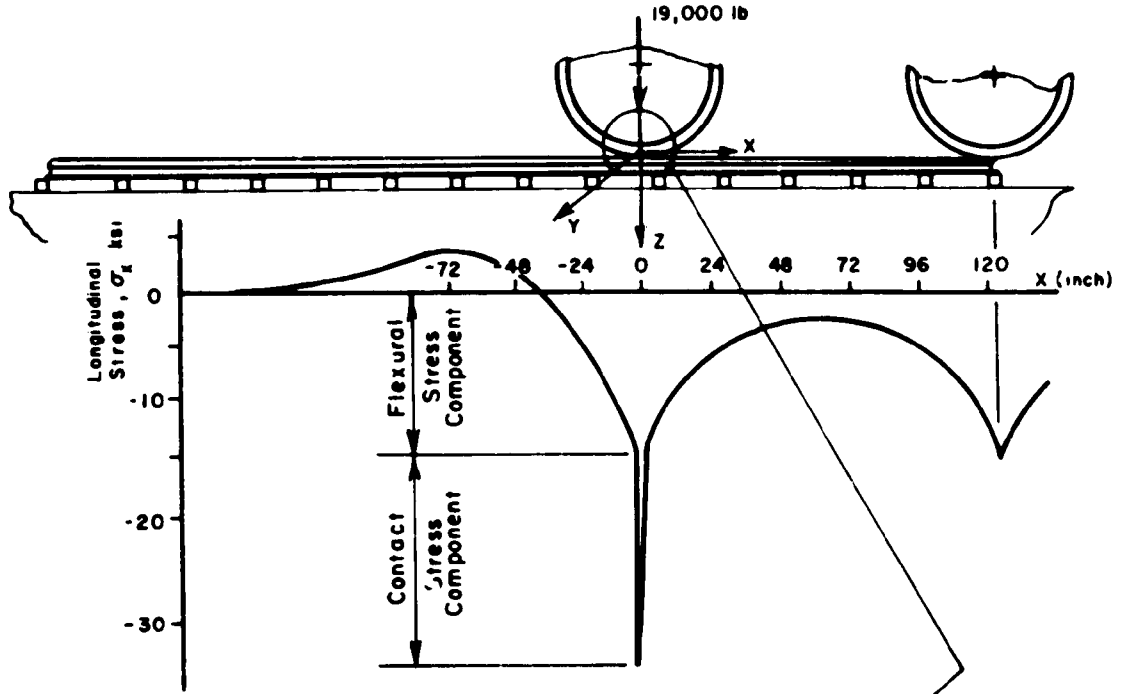
literature prior to 1976. A description of stresses in rail end regions and bolted rail joints is contained in later reports.

1.2 GENERAL DISCUSSION OF STRESS CYCLES IN RAILS/ DESCRIPTION OF BASIC LOAD HISTORIES IN RAIL DUE TO ROLLING LOADS

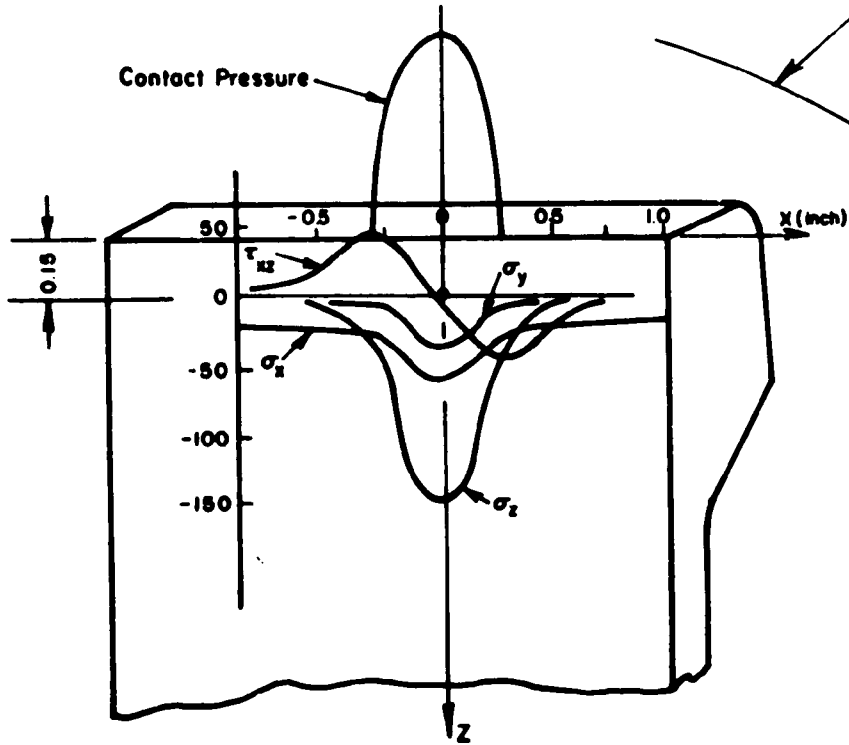
The stresses induced in rail due to passing vehicles are the combined results of three basic loading mechanisms. When the vehicle approaches to within 6 to 12 feet of a particular point in the rail head that location experiences a tensile bending stress due to the flexural action of the rail on the elastic foundation of the ties, ballast and subgrade. As the vehicle approach is closer to the point, the flexural tensile stress becomes a compressive stress of greater absolute value than that of the previous tensile stress. This stress history is illustrated in Figure 1. Significant variations in these flexural stresses occur due to the wide variations in load carrying capacity of individual ties. Nonuniform rail support in conjunction with large variations in the lateral position of wheel on the rail leads to local bending and twist of the rail which can cause significant variations in the flexural stresses in the head-web fillet regions.

When the point of application of wheel load is within 0.3 to 0.5 inches of a point in the rail head, large contact stresses develop due to the local deformation of the rail head near the region of application of wheel load, as shown in detail in the inset of Figure 1. These stresses are in general much larger in absolute magnitude than are the flexural stress components. The contact stresses are, in general, compressive with the exception of a transverse shearing stress component which completely reverses as the rolling load passes. The contact stresses developed in the proximity of the wheel/rail contact zone which frequently exceed the yield stress of the material, have long been suspected as an important cause of rail head failure. Yielding of the rail head occurs at a distance of 0.15 to 0.30 inches below the contact zone due to the highest principal shear stresses. The approximate magnitude of stresses incurred in new rails due to both flexural action and contact deformation are tabulated in Table 2.

When wheel loads are in excess of approximately 19000 pounds, new rails plastically deform upon passage of the first vehicle. Under normal



a) Flexural stress distribution along the rail.



b) Stresses near the contact region.

FIGURE 1. STRESS HISTORY IN RAIL HEAD DUE TO ROLLING LOAD

TABLE 2. TYPICAL MAXIMUM AND MINIMUM STRESSES IN A 132-LB
RAIL HEAD UNDER A VERTICAL WHEEL LOAD OF 19,000 LB

Stress Component	Flexural Stress (Ksi)	Contact Stress (Ksi)	Combined Stress (Ksi)	Residual Stress (Ksi)
Longitudinal σ_x	4 -10	0 -50	4 -60	-12
Lateral σ_y	20 0	0 -40	0 -40	-11
Vertical σ_z	0	0 -155	0 -155	-3
Transverse Shear τ_{xz}	0 ⁽¹⁾	34 -34	34 -34	--
Octahedral Shear τ_{oct}	5 0	53 0	58 0	--

(1) Warping stresses in the head and flange can reach 13,000 psi and 20,000 psi respectively due to eccentric vertical loads.

freight traffic residual stresses are known to build up in the rail head in a region adjacent to the tread surface. This region extends to nearly a quarter of the depth of the head. The residual stress buildup results in a zone directly beneath the tread surface which is subjected to compressive stresses and an adjacent region of tensile stress deeper in the rail head. Table 2 gives approximate values for various residual stress components at a depth of approximately 0.15 inch from the tread surface as determined by experiment.

As the first wheel of the wheel set passes, the contact stresses rapidly return to zero while the flexural stresses diminish more slowly. Interaction of flexural stresses from the adjacent wheel may not permit the flexural stresses to reverse until the second wheel has passed, Figure 1.

A review of stresses arising from both flexural and wheel/rail contact indicates that although each set of stresses may be severe, the effect of the combined action of these stress fields may be more damaging than a simple additive effect. This is especially true if the frequent plastic yielding and resultant residual stress conditions which occur are considered. Furthermore, the complex factors associated with build up of residual rail stresses appear to be closely linked to conditions controlling rail wear. At a minimum, rail wear leads to significantly increased flexural stresses. An understanding of the relation of the combined action of rail stresses is crucial to the understanding of rail reliability.

1.3 SUMMARY OF RAIL STRESSES, ANALYSES AND MEASUREMENT TECHNIQUES

1.3.1 Flexural Stresses

Flexural stress produced by vertical wheel/rail loads are the result of vertical bending of the rail, and compression of the web. The stresses, due to these actions, are all of sufficient magnitude to warrant consideration as causes of fatigue damage.

The stress, due to vertical bending, ranges from tension to compression and can be of the order of -15000 psi to 5000 psi in the head for 400,000-pound wheel loads; wear of 3/8 inch of the head can cause these stresses to be increased by over 100 percent. The vertical bending of the head on the elastic foundation of the web produces an additional compressive stress of -2000 to -5000 psi directly beneath the load. In that the wave length of this stress along the rail is short, it does not permit the reverse bending stress between wheels to be greater than 20 percent of the stress beneath the wheel load.

Significant stresses are produced by the action of lateral wheel loads and the eccentric application of vertical wheel loads (i.e., vertical loads applied off the plane of symmetry of the rail). The principal influence of these loads is felt in the rail head as a distortion of the bending stress distribution. This redistribution of stresses arises from both lateral bending of the rail under lateral loading and the warping of the rail cross-section caused by the resistance to torsion of the rail under the action of both eccentric, vertical, and lateral loads. For 132-lb RE rail the longitudinal bending stresses resulting from lateral bending under a 10,000-lb lateral load, can reach 11,000 psi in the head and 21,000 psi in the base. Warping stresses under these conditions can reach 7,000 psi in the rail head and 11,000 psi in the base. The warping stresses arising from the eccentric vertical loads reach comparable magnitudes.

The torsion produced by eccentrically applied vertical loads also causes additional stress in the fillet region of 20,000 psi for a 40,000-lb applied wheel load. When accompanied by high lateral flanging forces, its maximum can exceed 60,000 psi in compression. The vertical stress in the web produced by lateral loads when superimposed on those produced by eccentric vertical loads can be quite significant. For example, the 132-lb RE rail underwent considerable design change in the fillet region to correct a fatigue-crack initiation problem in the 131-lb RE rail.

Lateral loads can produce torsion of the rail section and vertical bending stress in the web and head. The vertical stress in the web produced by lateral loads when superimposed on those produced by eccentric vertical loads can be quite significant.

The classical analytical treatments of the flexural stresses in rails using beam on elastic foundation theory along with some additional stress components due to head bending, etc., permit flexural stresses to be determined analytically in the rail to within 10 percent. Considerable experimental work has been performed to validate these results. This accuracy is good in view of other possible sources of errors involved. Unfortunately, the critical flexural stress components in the fillet region, do not permit simple closed form analytical solutions and, therefore, only empirical approaches have been developed for design purposes. The weakness of these procedures is in extending the application to problems beyond the experimental data from which the empirical relation was developed.

In general the classical track design procedures do not provide the kind of detailed rail stress information that is needed to evaluate the failure mechanisms. The beam-on-elastic foundation models can only be used to evaluate the effect of differences in track condition by changing the support modulus. Finite element procedures have been recently used to evaluate the effects on rail stress of variable tie spacing, tie type, ballast and subgrade characteristics and wheel loading. Beam theory can be used in conjunction with these procedures to obtain many of the gross bending components; however, beam theory does not account for geometrical effects on three-dimensional stresses nor for the inaccuracies of the strength of materials assumption that plane sections remain plane during bending. Therefore, a more detailed model of the fillet regions is required.

1.3.2 Thermal Stresses

It has been generally accepted that stresses due to thermal expansion or contraction of rails are small in comparison with those of wheel loads. Variation of 68F would produce a longitudinal thermal stress of 6,900 psi. While this stress is small, it should be considered when analyzing stresses in the neighborhood of plastic deformation, evaluating fatigue damage, or when predicting the onset of buckling behavior and rail roll over.

The analysis of thermal loading is quite straightforward, and existing treatments appear to be adequate. Since thermal stress effects are easily accounted for in finite element analysis procedures, the problem may be treated along with the flexural problems.

1.3.3 Contact Stresses

Contact stresses and stresses local to the region of wheel-rail contact are greatly affected by both the lateral and longitudinal tractions. Lateral force resulting from tracking of the wheel back and forth across the rail or sliding of the wheel laterally can be caused by track irregularities or curves. Longitudinal tangential forces result from acceleration and deceleration of the locomotive and "stick-slip" of wheels due to the axle wind-up on curves. In both the tangential loading conditions, the full slip condition creates the highest shear stresses in the rail.

Under conditions involving new wheels and rails in normal contact, yielding of the rail would occur at a location 0.1 to 0.2 inch below the rail surface when the wheel load exceeds approximately 19,000 lbs. Under the influence of a purely normal load, the rail surface will tend to flow in the

direction of rolling if yielding occurs. If in this contact situation the normal load remains below 31,500 lbs, plastic deformations occurring with each wheel passage will decrease and eventually stop and stresses will be thereafter elastic, i.e. "shakedown" of the post yield stresses should theoretically occur.

The compressive surface stresses reach levels in excess of -180,000 psi for a wheel load of 19,000 lbs. This same wheel load would create values of octahedral shearing stress of 54,000 psi and a transverse shearing stress of 34,000 psi which fully reverses during the rolling cycle. This transverse shearing stress component has been identified as being most degrading from the viewpoint of fatigue damage [8].

All the analytical approaches applied to date to investigate the stresses in the vicinity of the contact area ignore the effects of wear, bending or temperature stresses in the rail. While these effects are important in the elastic problem, they may have a still greater effect when plastic deformations are considered.

In the present design considerations of rails, the Hertzian contact theory is used exclusively. The high degree of accuracy of the Hertzian theory has been established for problems within the basic assumptions of the theory. Since rail deforms plastically, thus introducing residual stresses, a Hertzian model of contact is of limited applicability. The work of Martin and Hay^[9] appears to present the most realistic rail head model yet developed, It can account for the development of residual stresses.

Another important aspect of contact loading which has not been considered is the effect of flat wheels. The potentially damaging effect of flat wheels is that the high impact loading may increase residual stresses locally to such an extent as to initiate cracks. Also, the sudden impact load may adversely alter the mechanical and fatigue characteristics of the rail steel.

1.3.4 Residual Stresses

When the rail yields, a residual compressive zone is established directly beneath the rail head. Beneath the compressive zone, a tensile stress zone is developed to a depth of approximately 0.5 inch or more. Horizontal cracks and split heads are known to initiate in this area. This field could be responsible for propagation of these flaws. Cracks occurring closer to the surface of the rail would likely arrest or turn due to residual compressive fields. Near the surface, a maximum range of shear stress occurs but cracks initiated by this stress may be more likely to result in pitting

rather than in such gross defects as horizontal or vertical splits.

When longitudinal tangential forces exist in the direction of rolling, more flow occurs. If the force is opposite to the direction of rolling, and is relatively small, the flow will also be in the direction of rolling. Flow will be opposite the direction of rolling if the force is greater than approximately 0.13 times the normal loading. The distribution of surface shear traction does not appear to greatly influence the subsurface distribution of strain. Therefore, the subsurface plastic distribution for partial slip is not likely to differ very greatly from that of complete slip.

When either the longitudinal or lateral force exceeds a value of approximately 0.35 times the normal wheel load, the onset of plastic deformation occurs on the surface of the rail within the contact area toward the rear. When the longitudinal force exceeds approximately 0.367 times the normal wheel load, whether or not plastic flow stops during the life of a rail is controlled by the surface shear stresses. Thus, the maximum load for yielding virtually coincides with the load for initial yielding of the rail.

In reality, a much larger region of the railhead is exposed to contact loading than has been predicted in three-dimensional stress analyses. Every wheel passes over the rail in a random fashion, thus extending the area of residual stress.

Plasticity introduces two effects, of which only one has been thus far investigated, i.e., the formation of residual stress. A two-dimensional model of rolling contact beyond the elastic limit has been developed by Merwin and Johnson [10]. Merwin and Johnson's model has been shown to possess reasonable accuracy for two-dimensional problems; it was this approach that Martin and Hay adapted to the three-dimensional finite element model of the rail. The model developed by Martin and Hay consisted of a short rail head section neglecting bending and thermal stress. They developed the residual field due to repeated loading across a single point on the rail. The results of Martin and Hay have not been validated in the literature.

The second effect introduced by plasticity is the redistribution of contact pressure caused by alteration of the rail surface contour by the plastic flow or wear. Such redistribution is known to greatly reduce the contact pressure, thus resulting in a more rapid shakedown of the rail. Work hardening of the rail material will also permit shakedown to occur at greater loads.

2. FLEXURAL STRESSES

2.1 BASIC FLEXURAL ACTION

Vertical and lateral wheel loads can result in various simultaneously occurring flexural actions of the rail. Vertical loads on the rail always result in vertical bending of the rail section and local bending of the head due to the compression of the web. Eccentrically applied vertical loads also cause torsion of the rail section and additional stresses to be concentrated in the fillet regions due to vertical bending of the web. Lateral loads can also produce torsion of the rail section and lateral bending of the web. The vertical stresses in the web produced by lateral load when superimposed upon those due to vertical eccentric loads can be quite significant.

2.2 STRESSES DUE TO VERTICAL BENDING

2.2.1 Analytical Treatments

Nearly all analytical treatments of vertical bending in rails have been through classical strength of materials approaches. The stresses computed in this way, as verified by numerous experiments, possess reasonable accuracy at points away from the region of wheel-rail contact.

2.2.1.1 Stresses Due to Vertical Bending of Rails - As early as 1867, Winkler^[11] proposed an analysis of vertical bending stresses in rail by considering the rails as being continuously supported by an elastic foundation. The differential equation governing the bending of a beam supported in this way is

$$EI \frac{d^4 W}{dx^4} + kW = q(x) \quad (1)$$

where $W(x)$ is the vertical deflection at x , EI is the flexural rigidity of the rail, $q(x)$ is the distributed vertical load and k is the base parameter associated with the "Winkler foundation model". In 1882, Schwedler^[12] presented the following solution for bending of longitudinal tie track for the case where an infinite beam is subjected to one concentrated force, P , Figure 2,

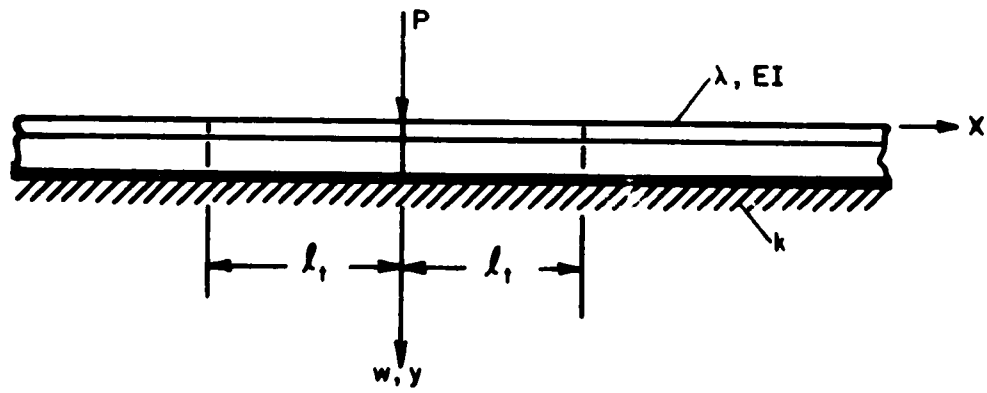


FIGURE 2. INFINITE RAIL WITH CENTRAL POINT LOAD

$$W(x) = \frac{P\beta}{2k} A(x) \quad (2)$$

and the corresponding expression for bending moment

$$M(x) = EI \frac{d^2 W}{dx^2} = \frac{P}{4\beta} B(x) \quad (3)$$

where

$$\beta = \sqrt[4]{\frac{k}{4EI}}$$

$$A(x) = e^{-\beta x} [\cos(\beta x) + \sin(\beta x)] \quad (4)$$

$$B(x) = e^{-\beta x} [\cos(\beta x) - \sin(\beta x)]$$

The track stiffness K_r is commonly written as

$$K_r = \frac{2k}{\beta} \quad (5)$$

In 1885, a book containing many solutions of interest for analysis of railroad track was published by Zimmerman^[13]. These examples were for longitudinal tie track which was in keeping with the assumptions of Winkler's original analysis. Timoshenko^[14] pointed out, however, that the analysis could be suitable for cross tie track if the track modulus, k , was properly chosen. Hetenyi^[15] showed that such an assumption is appropriate for cross tie track if the tie spacing, l_t , obeys the relation,

$$l_t \leq \left(\frac{\pi}{4}\right)^2 \sqrt[4]{\frac{4EI}{k}} \quad (6)$$

Figure 3 shows Equation (6) plotted for various rail sections and track moduli. For most rail (115 RE or larger) with 22 inch tie spacing, the beam-on-elastic foundation model can be used without fear of inadequacy of the model due to the discontinuous support.

Normalized curves for the rail deflection and the rail bending moment are shown in Figure 4. The distance from the loading point to the point of zero bending moment is a convenient reference distance. This can be

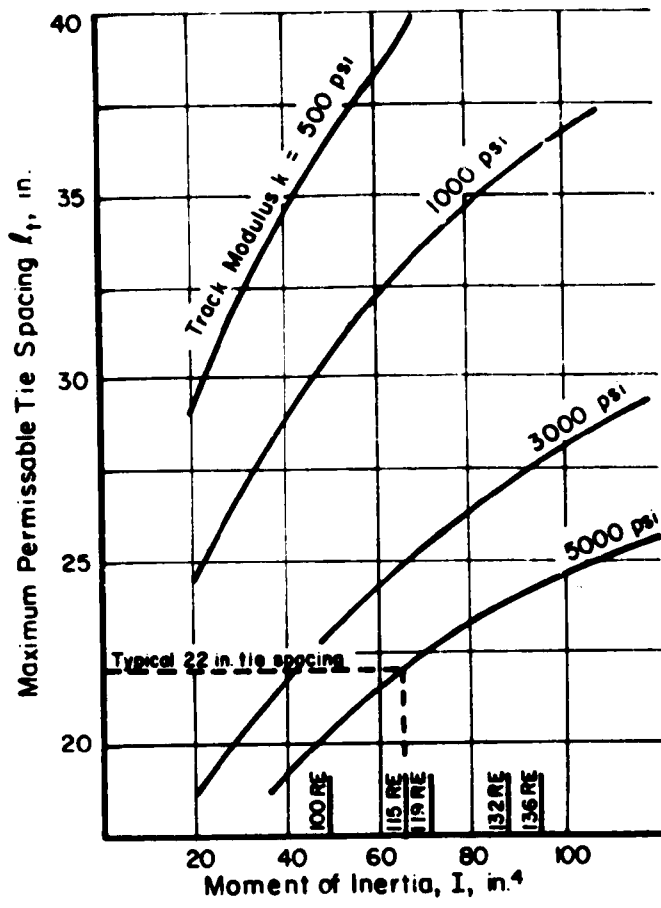


FIGURE 3. MAXIMUM ALLOWABLE TIE SPACING FOR WINKLER MODEL

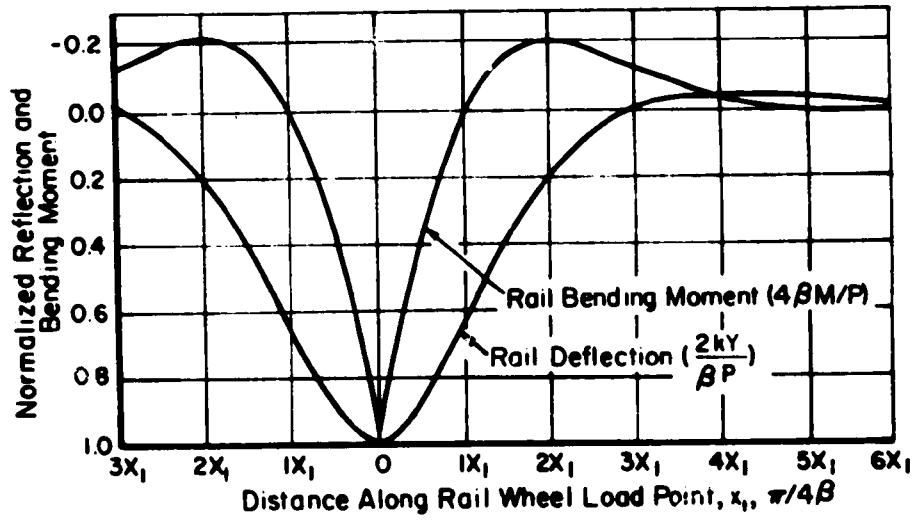


FIGURE 4. NORMALIZED RAIL DEFLECTION AND BENDING MOMENT CURVES

calculated for the first occurrence of the condition $M=0$ Equation (3) as

$$X_1 = \frac{\pi}{4\beta} \quad (7)$$

and the distance from the load to the point of zero rail deflection X_2 is

$$X_2 = 3X_1 \quad (8)$$

For reference purposes, Table 3 lists typical data for the characteristic lengths X_1 and X_2 for the range of rail sizes normally used by the railroad industry.

The solutions for the rail bending moment and deflection due to a point load can be superimposed to obtain the total deflections and bending moments resulting from the wheel loads of single or multiple cars. Typical axle spacings from 6 to 8 feet, would be equivalent to a distance of about $2X_1$ to $3X_1$. The curves in Figure 4 show that adjacent wheel loads will usually increase the rail deflection but reduce the bending moment under the reference wheel.

The analytical results based on Equation (1) have been generally accepted and proven by corresponding test results to provide acceptable values for rail deflections and bending stresses in regions adjacent to the point of application of load. Representative applications of simple beam-on-elastic foundation analysis to rails are presented by Talbot^[16], Timoshenko and Langer^[17], and more recently, Eisenmann^[18]. Innumerable other applications exist in the literature. As pointed out by Keir^[19], these methods are used by many railroads for design purposes. The "practical" application of the analysis to track design is presented by Clarke^[20] in the series on "Track Design Fundamentals" and by Battelle^[21].

An inherent deficiency of using the beam on elastic foundation theory for railroad track consisting of ballast on top of a subgrade is that the Winkler foundation model neglects any continuity or coupling in the foundation, i.e., shear in the ballast is neglected. This model assumes that a pressure applied to one area of the foundation does not cause any deflection outside the loaded area. There have been several attempts at improvement of this simple model.

Hanker^[22] provided a somewhat more rigorous theory by including

TABLE 3. TYPICAL DATA FOR CHARACTERISTIC LENGTHS FOR X_1 AND X_2 *

Track Modulus k, (psi)	100# Rail		115# Rail		132# Rail	
	X_1 (in.)	X_2 (ft.)	X_1 (in.)	X_2 (ft.)	X_1 (in.)	X_2 (ft.)
500	45.9	11.5	49.4	12.3	53.1	13.3
1000	38.6	9.7	41.5	10.4	44.7	11.2
1500	34.9	8.7	37.5	9.4	40.4	10.1
2000	32.4	8.1	34.9	8.7	37.6	9.4
3000	29.3	7.3	31.5	7.9	34.0	8.5
4000	27.2	6.8	29.3	7.3	31.6	7.9

*See Equations (7) and (8).

the effects of a resisting couple produced by the ties which is, in effect, an attempt to characterize the resistance of the ties to the rotation imposed by the rail deflection.

Hanker assumed that a distributed moment, proportional to the rail rotation is applied. Then the differential equation governing bending of the rail becomes

$$EI \frac{d^4 w}{dx^4} - \gamma \frac{d^2 w}{dx^2} + kw = g(x), \quad (9)$$

where γ is the track modulus representing the effect of a continuously distributed resistance to bending. Although analytically more rigorous, the approach also necessitates the experimental determination of γ . It is unlikely that the effects of γ could be uncoupled from the vertical resistance, k . In fact, the effect of a distributed moment is probably taken into account when track deflection measurements are made.

Another attempt at a more realistic subgrade model was made by Weitsman^[23] (1970). This model incorporates shear stresses and some of the effects of lateral displacements within the subgrade. These effects are absent in the Winkler model which consists of uncorrelated linear springs. The model which is attributed to Reissner (1958), retains much of the mathematical simplicity of the elastic foundation. The differential equation governing bending of the rail becomes

$$-EI \lambda_1 \frac{d^6 w}{dx^6} + EI \frac{d^4 w}{dx^4} - \lambda_2 \frac{d^2 w}{dx^2} + k_1 w = g(x) - \lambda_1 \frac{d^2 g(x)}{dx^2}, \quad (10)$$

where

$$\begin{aligned} k_1 &= \frac{E_s}{h} \\ \lambda_1 &= \frac{Gh}{12 E_s}, \\ \lambda_2 &= \frac{Gh}{3}, \end{aligned} \quad (11)$$

and where,

E_s, G = the ballast/subgrade elastic and shear moduli, respectively,

h = the ballast/subgrade thickness.

In light of unquestionable difficulties Weitsman had in determining subgrade characteristics, the elegance of the Reissner theory is, as is the Hanker model, over-shadowed by the simplicity of the Winkler model.

Another shortcoming of the simple Winkler model is its inherent inability to allow lift-off of the rail in front of an approaching vehicle.

Weitsman goes on to demonstrate the effect of absence of tensile reactions across the interference between the rail and the ballast in both the models proposed by Winkler and Reissner. With the Winkler model, the governing equations are quite simple. Namely,

$$EI \frac{d^4 w}{dx^4} + kw = q(x) \quad 0 \leq |x| \leq X_2 \quad (12)$$

$$EI \frac{d^4 W}{dx^4} = q(x) \quad \xi_0 \leq |x| \leq X_2 + \xi_0 \quad (13)$$

Some of the resulting solutions for the depressed and lift-off regions resulting from these equations are shown in Figure 5. Solutions were developed for limiting values, i.e., 100 RE rail (low I) on poor, fine cinder ballast on loam and clay subgrade (low k), and 136 RE rail (high I) on stable limestone ballast (high k). These results demonstrate that the region of lift-off is relatively insensitive for standard rail sizes to ballast and subgrade conditions for most track. However, the size of the depressed region varies greatly.

The Winkler foundation model represents the entire track structure by a single experimentally determined parameter--the track modulus, k . To incorporate the many other track structure parameters in addition to the track modulus in a form suitable for parametric analysis requires the formulation of a mathematical model more complex than the simple solutions just described. Such a model would predict ballast and subgrade stresses as well as rail bending moment and deflection. The complexity of the track structure precludes all but a numerical approach to this problem. Numerous proposed models have appeared recently in the literature. They all, however, are based

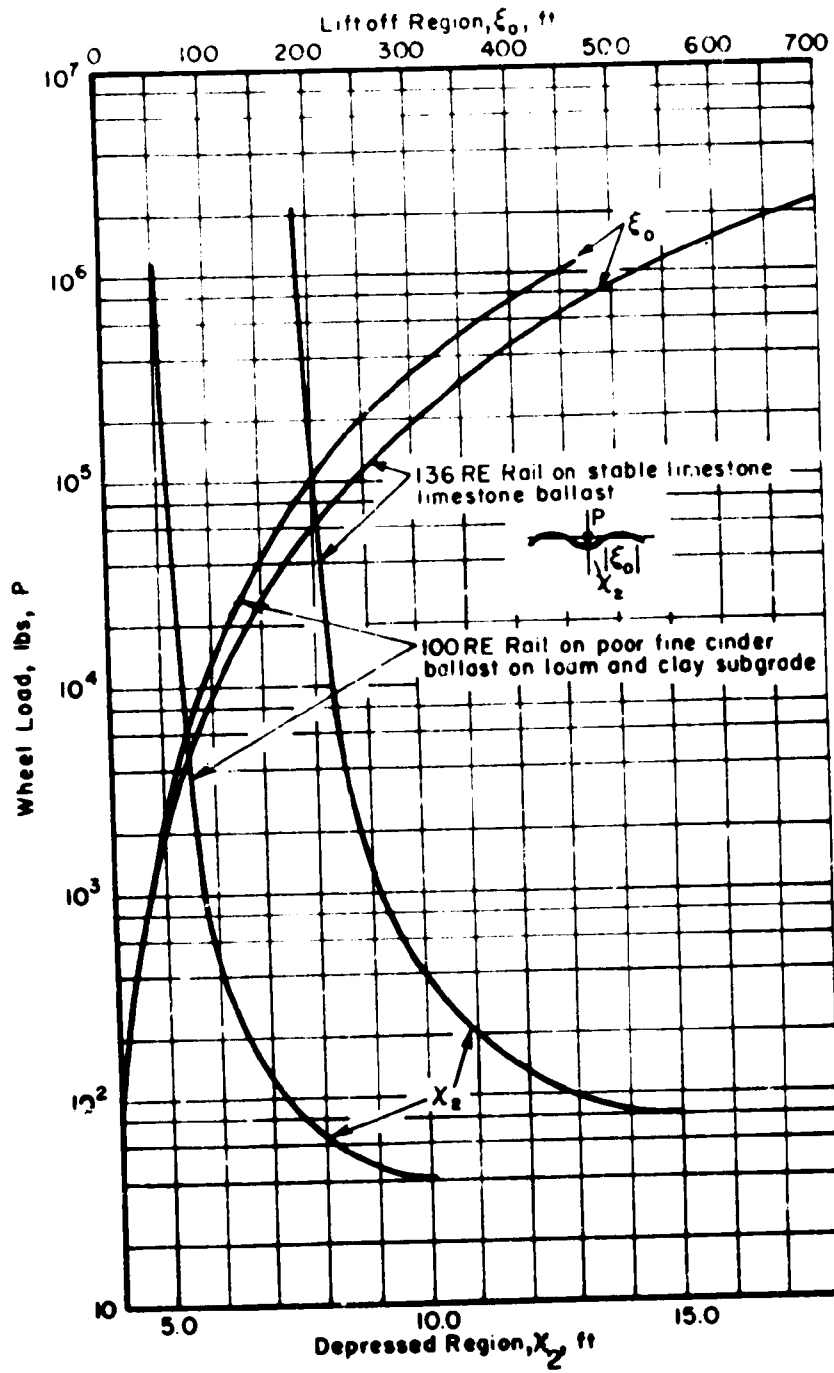


FIGURE 5. DEPRESSED AND LIFT OFF REGIONS AT VARIOUS WHEEL LOADS USING THE WINKLER THEORY

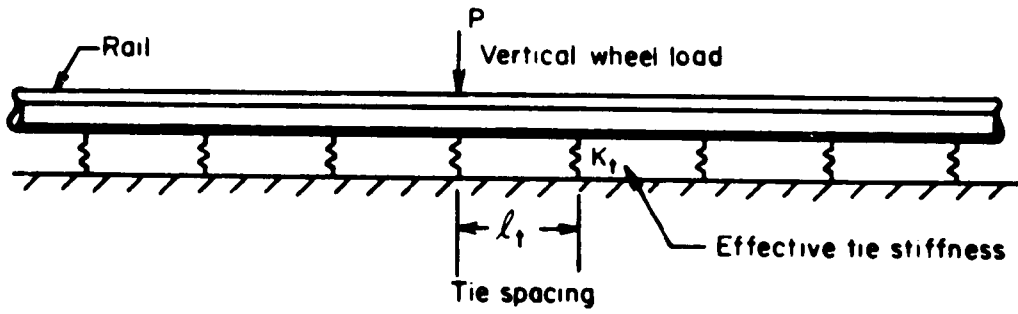
upon beam theory and, therefore, do not include load concentrations, geometric singularities or stress raisers in the rail itself. Several representative models are described below.

An early one-dimensional finite-element model based on elementary beam theory^[21], Figure 6a was used to evaluate the effect of missing or defective ties on track safety. In this model, an effective tie stiffness K_t represents the total elasticity of the support below the rail base and includes the deflection of the ballast and the road-bed. The output from this computer program is a prediction of rail bending stresses, rail deflection, tie plate loads, and ballast pressures for the different track configurations, i.e., section modulus, track modulus, tie spacing, and various combinations of missing ties. Only vertical loading is permitted.

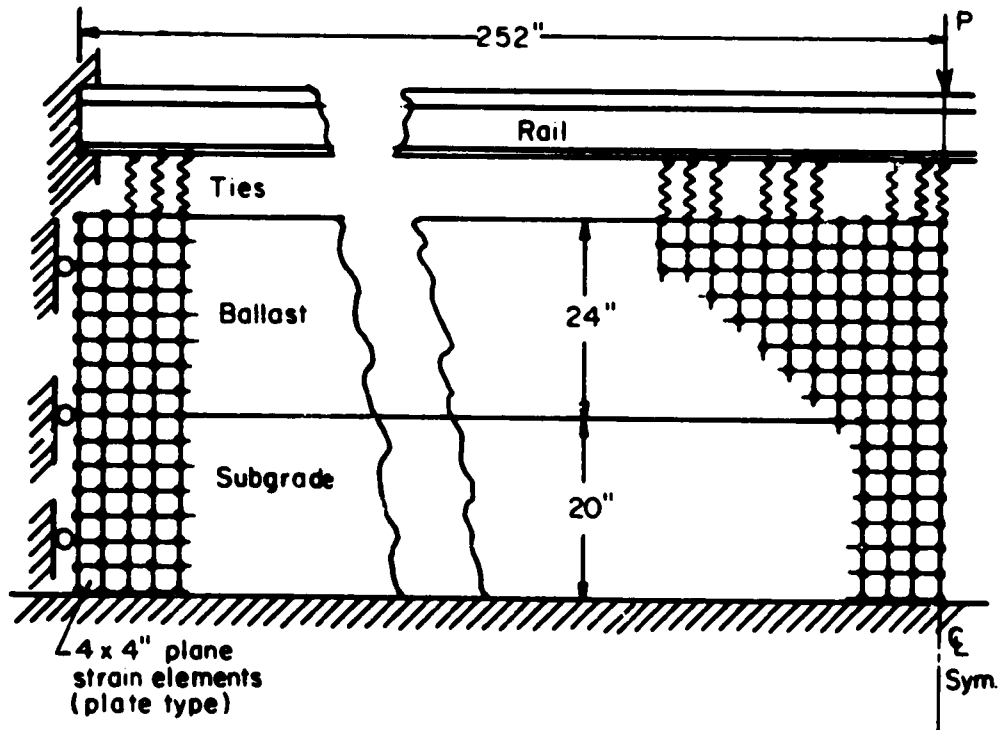
One of the more advanced finite-element models is due to Lundgren, et al. Figure 6b presents the Lundgren^[24] plate type, two-dimensional finite-element grid. This computer program was set up to accept the track variables given in Table 4. The values Lundgren used were based on estimates taken from the literature. The program used the Mohr theory of failure in conjunction with the plate type element to predict load distribution in the ballast and subgrade. An iterative procedure (requiring about six cycles for convergence) was used to calculate load redistribution in the foundation as the yield limit was exceeded in various individual elements.

The Lundgren program was used to calculate rail deflections and bending moments as well as stresses in the foundation. It was noted, however, that the element size used was too large to give an accurate picture of stresses in the foundation. Good agreement was found between the model deflection results and those obtained with the simple Winkler foundation model. A somewhat similar model was introduced by Butler^[26]. Kilmartin^[25] developed a more general plan in which the coupling between rails is introduced by introducing springs between the rail and tie whose stiffness has been determined to be equivalent to the tie acting as a beam on an elastic foundation.

A more complete track structures model has been developed by Martin at AAR. This model, Figure 7, permits variable tie size and spacing, multiple wheel loads, and multiple ballast and foundation. The model centers about representing the ballast as a layered elastic media using the Herrmann, PSA finite element code.



a. Battelle One-Dimensional Track Model



b. Lundgren Two-Dimensional Track Model

FIGURE 6. FINITE ELEMENT TRACK MODELS

TABLE 4. LUNDGREN'S INPUT VARIABLES

Structural Element	Variables
Rail	Stiffness (EI)
Tie	Stiffness (EI) Length Spacing
Ballast	Type (E, ν , yield stress) Depth
Subgrade	Type (E, ν , yield stress)

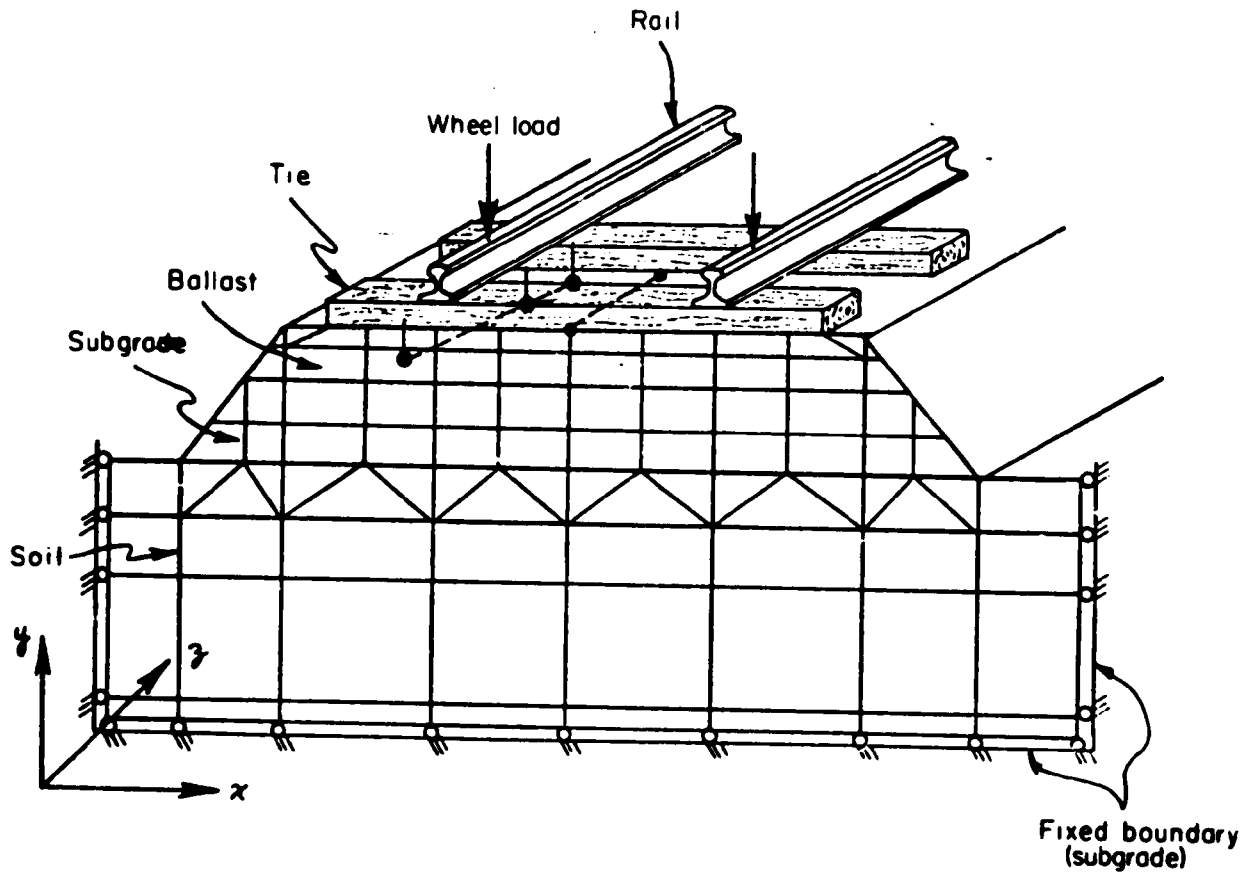


FIGURE 7. GEOMETRICAL CONFIGURATION IN PSA SIMULATION

In that the PSA does not possess sophisticated isoparametric elements, the element grid must be sufficiently fine to permit a physically realistic stress distribution to be computed immediately beneath the tie. Stress distributions deeper within the ballast and subgrade may be more or less sensitive to the grid density directly beneath the tie. Work currently underway at Battelle should produce a more accurate representation. In this work, the rail is represented as a beam on discrete elastic supports.

2.2.1.2 Local Bending Stresses Near the Point of Load - It is generally accepted that rail deflections and bending stresses can be predicted with acceptable accuracy for uniform track conditions if the track modulus has been determined by prior measurement. Even here, large variations in k produce only small deviations in bending stress. Hetenyi^[15] showed that a 100 percent variation in k results in a 16.5 percent variation in maximum bending stress. A significant error in the longitudinal stress computed from ordinary bending theory occurs in the vicinity of the application of load. This may be seen in Figure 8 for a PS 130 lb rail loaded with central and eccentric, 30,000 lb vertical loads.

The flexural stresses in the head near the point of application of load are caused by the behavior of the head as a beam on an elastic foundation provided by the web.

The modulus of support reaction can be estimated by using plate theory^[18]. For vertical loading^[17] the foundation modulus of the head is

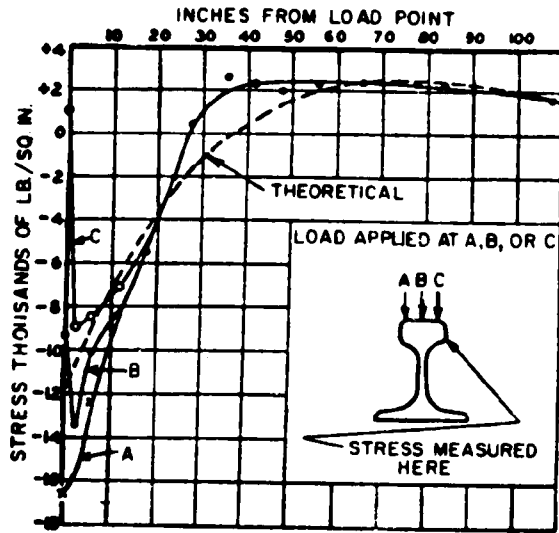
$$k = \frac{tE}{d} \quad (14)$$

where

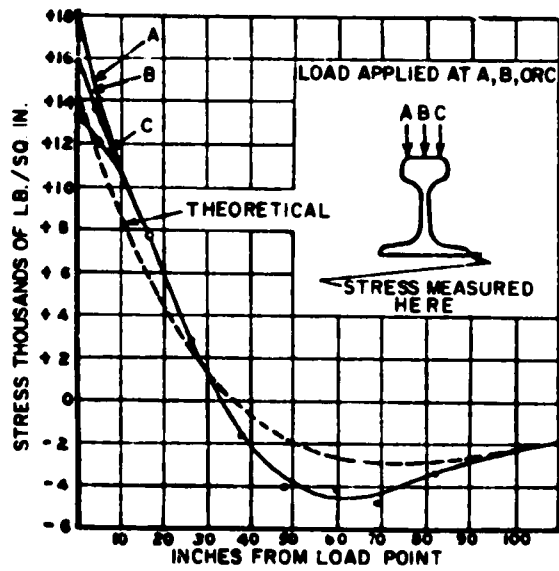
$$\begin{aligned} d &= \text{web height} \\ t &= \text{average web thickness} \end{aligned}$$

When the load is lateral the bending of the web must be considered and the modulus of foundation for the web is

$$k = \frac{Et^3}{d^3} \quad (15)$$



a. Head



b. Base

FIGURE 8. LONGITUDINAL BENDING STRESS FROM 30,000-LB VERTICAL LOAD P.S. 130-LB RAIL IN TRACK[16]

(The base stress was measured 0.25 inch above the bottom of the rail and the head stress below the top)

2.2.2 Comparison Between Calculated and Experimental Results

By using the additional local stress components due to local head bending, Timoshenko and Langer^[17] demonstrate that excellent correlation with experimental results can be obtained, Figure 9.

Eisenmann^[18] presents calculated values for longitudinal stress using techniques like those of Timoshenko and Langer. These calculations were based on 25.6 inch tie spacing with $k = 365$ psi/in. This particularly instructive presentation shows stresses resulting in a rail section subjected to a wheel load of 22,000 lb. Eisenmann also exhibits experimental results for loaded rail sections. Of interest is the occurrence of a tensile bending stress at the lower edge of the head even for central loading, thus showing the effect of local head bending. This stress can assume rather large values for inclined loading, Figures 10, 11, and 12. Eisenmann points out that by using the additional stress components that the theoretical calculated longitudinal stresses are generally 10 percent higher than those determined experimentally.

A large amount of field data exists in the AREA Proceedings on the subject of head bending stress. These data were often obtained for the purpose of checking a particular section of track or for addressing very specific problems rather than for the purpose of describing the nature of stresses in rails. Therefore, these data have been intentionally omitted.

2.3 LATERAL BENDING AND TWIST

2.3.1. Eccentric Vertical Load

Eccentric vertical loading is almost always encountered in practice. The effect upon the longitudinal stress in the rail was just shown. The vertical load, P , Figure 13, produces in addition to this vertical bending a twist of the rail due to the applied couple, Pe .

If, for a section of rail, one end is restrained and a torque $M_t = Pe$ is applied to the other end then this torque is resisted partly through twist M_1 and partly through bending M_2 of the head and base of the rail. If ϕ is the

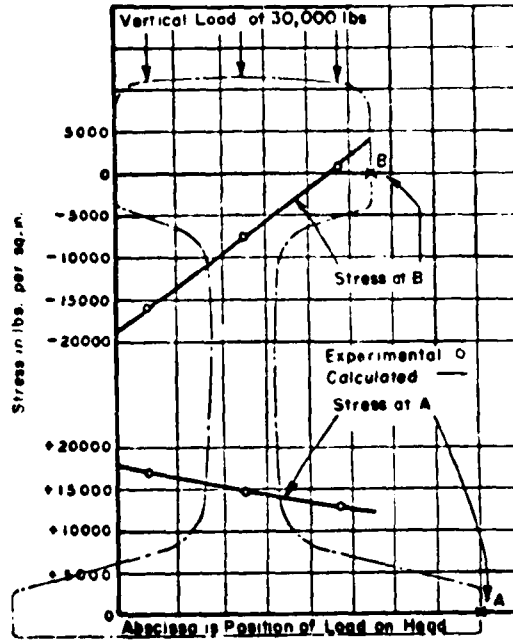


FIGURE 9. COMPARISON OF CALCULATED LONGITUDINAL STRESSES WITH EXPERIMENTAL RESULTS [17]

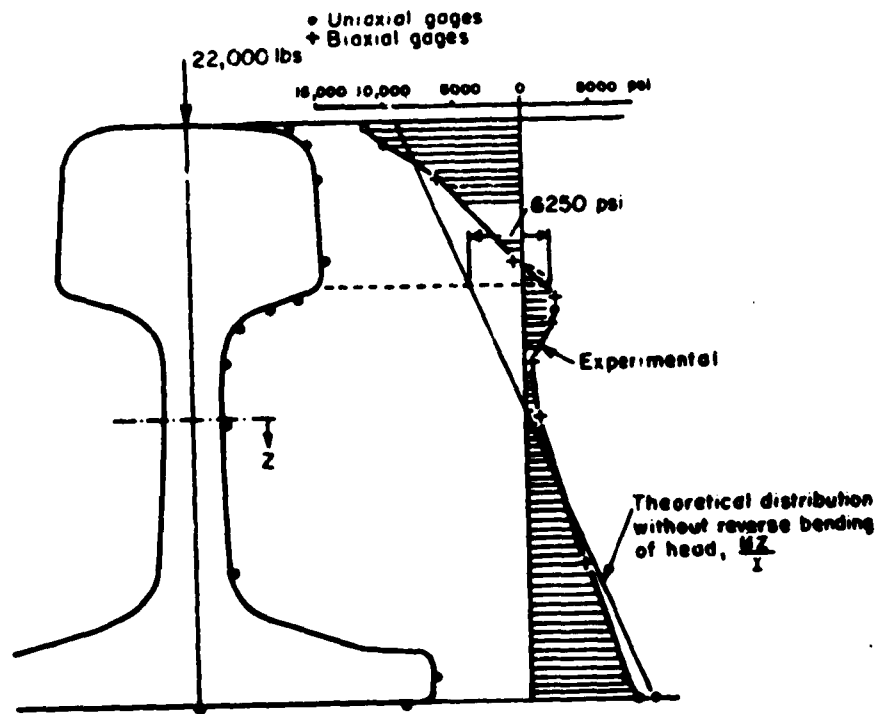


FIGURE 10. EXPERIMENTAL LONGITUDINAL STRESS DISTRIBUTION UNDER CENTRAL LOAD [17]

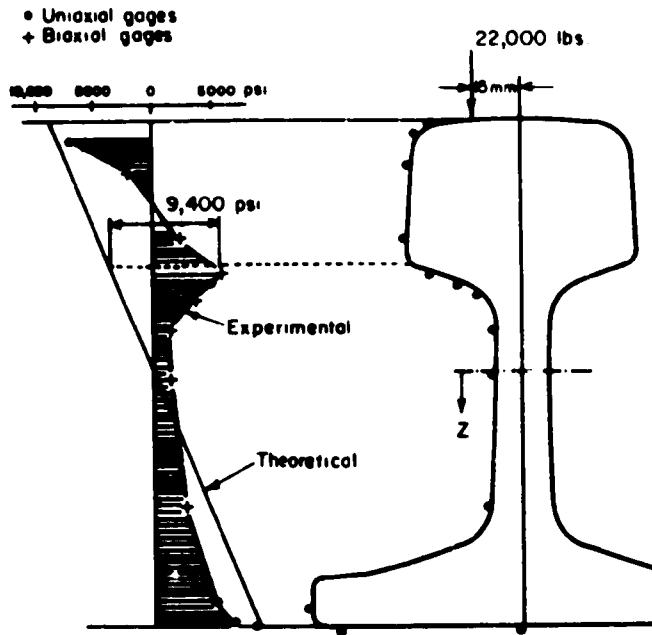


FIGURE 11. EXPERIMENTAL LONGITUDINAL STRESS DISTRIBUTION UNDER ECCENTRIC LOAD [18]

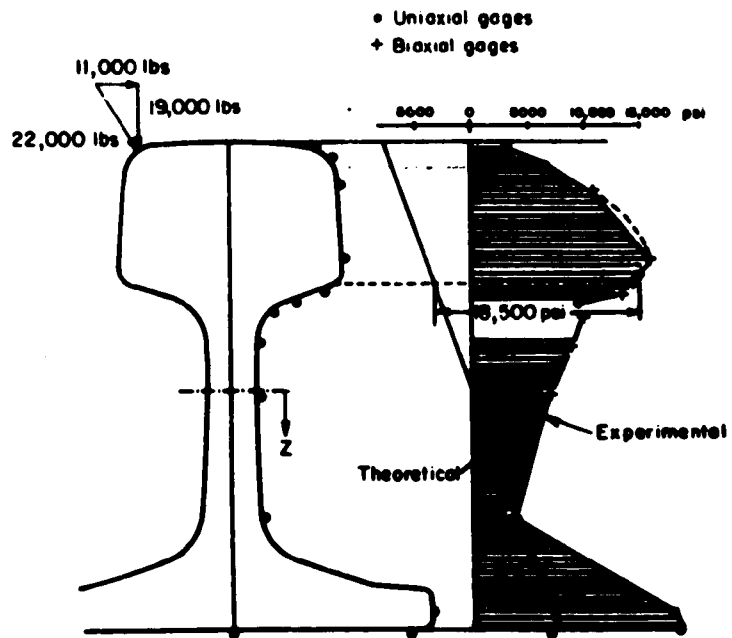


FIGURE 12. EXPERIMENTAL LONGITUDINAL STRESS DISTRIBUTION UNDER INCLINED LOAD [18]

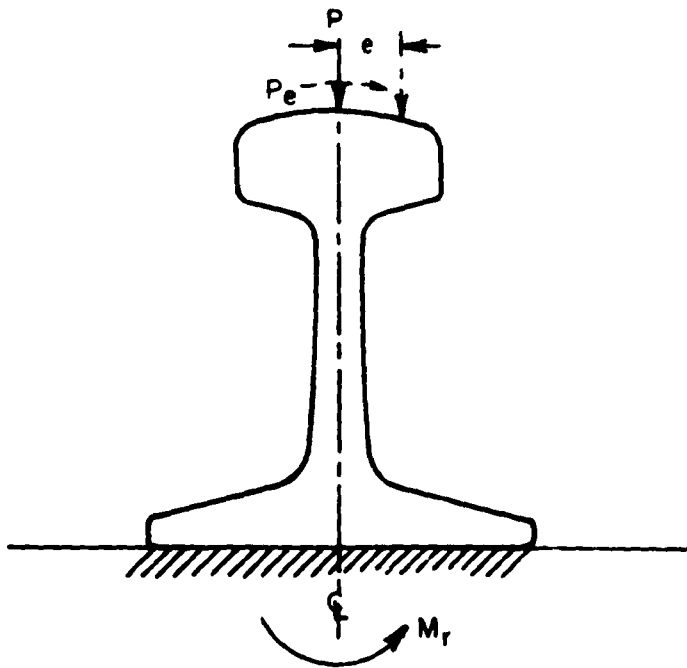


FIGURE 13. RAIL WITH ECCENTRIC VERTICAL LOAD

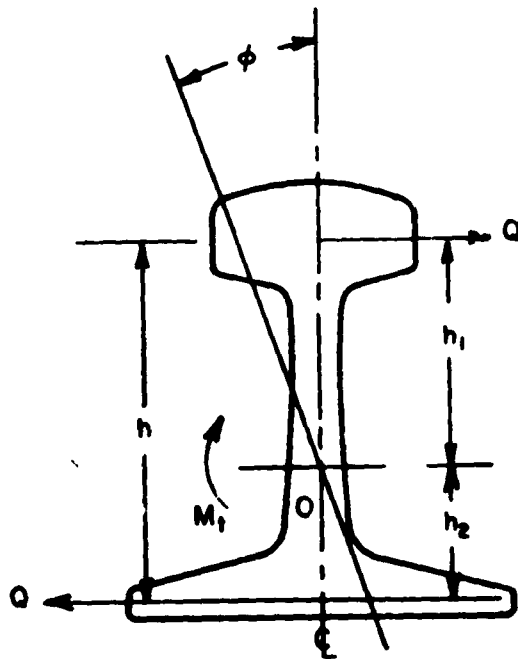


FIGURE 14. ANALYSIS OF RAIL SUBJECTED TO ECCENTRIC VERTICAL LOADING

twist, Figure 14, then

$$M_1 = -C \frac{d\phi}{dx} \quad (16a)$$

where

$$C = \frac{A^4 G}{40 I_p}$$

A = cross sectional area

G = modulus of rigidity, and

I_p = polar moment of inertia.

The moment carried by the head and base is represented in Figure 14 by Qh, in which Q denotes the shearing force due to bending and h is the distance between the centroids of the head and base sections. Then

$$M_2 = Qh = h^2 D \frac{d^3\phi}{dx^3} \quad (16b)$$

where

$$D = \frac{EI_1 I_2}{I_1 + I_2}$$

thus the differential equation governing the twist of the rail is

$$Dh^2 \frac{d^3\phi}{dx^3} - C \frac{d\phi}{dx} = M_1 + M_2 = M_t \quad (17)$$

It has been assumed that the twist of the rail can be uncoupled from the deflection.

The solution of Equation 17 is

$$\frac{d\phi}{dx} = \frac{M_t}{C} (1 - e^{-\rho x}) \quad (18)$$

where

$$\rho = \left[\frac{C}{Dh^2} \right]^{1/2} \quad (19)$$

It is seen from Equation (18) that the solution rapidly approaches the case of simple torsion for increasing x; therefore, bending of the head

and base of the rail have only a localized effect on the torsion of the rail.

Considering the rail supported on an elastic foundation along its length, and that the foundation exhibits a resisting couple per unit length of rail of $K_1 \phi$ then the governing differential Equation (17) becomes

$$Dh^2 \frac{d^4 \phi}{dx^4} - C \frac{d^2 \phi}{dx^2} + k_1 \phi = 0 \quad .$$

The general solution for a rail infinite in extent can be written as

$$\phi(x) = e^{-mx} (C_1 \sin nx + C_2 \cos nx) \quad (20)$$

where

$$m = \frac{C}{2Dh^2}$$

$$n = \left[\frac{k_1}{Dh^2} - \left(\frac{C}{2Dh^2} \right)^2 \right]^{1/2} \quad .$$

The constants of integration are determined by the conditions at $x = 0$. From Equation (20) it is seen that the twist of a rail affixed to an elastic foundation is represented by a wavy line, and that the amplitude of the wave decreases with increasing distance from the loaded region.

2.3.2 Stresses Due to Lateral Loads

When lateral wheel loading, H , is applied to a rail it produces both twist and lateral deflection. Once more the effect of lateral load upon the longitudinal bending stress is shown in Figure 12. The Timoshenko and Langer [17] treatment represents the classical approach to the lateral load problem. It is assumed that the rail is continuously supported by an elastic foundation resisting both the lateral deflection with foundation modulus k_2 and twist with foundation modulus k_1 as in the previous section. Letting y be the lateral deflection the differential equation governing lateral bending is

$$EI_1 \frac{d^4 y}{dx^4} + k_2 y + gk_2 \phi = 0 \quad (21)$$

where g is the distance from the base to the centroid and where EI_1 is the flexural rigidity of the rail in the horizontal plane. The differential equation governing the angle of twist is from Equation (17)

$$Dh^2 \frac{d^4 \phi}{dx^4} - C \frac{d^2 \phi}{dx^2} + (k_1 + gk_2)\phi - k_2 y = 0 . \quad (22)$$

A solution for the lateral deflection and twist must satisfy the two simultaneous coupled differential Equations (21) and (22) and the following boundary conditions at the loaded cross section;

$$\left(\frac{dy}{dx}\right)_{x=0} = 0, \quad EI_1 \left(\frac{d^3 y}{dx^3}\right)_{x=0} = hf/2, \quad \left(\frac{d\phi}{dx}\right)_{x=0} = 0 \quad (23)$$

$$-C \left(\frac{d\phi}{dx}\right)_{x=0} + Dh^2 \left(\frac{d^3 \phi}{dx^3}\right)_{x=0} = hf/2 ,$$

where f is the distance from the top of the rail to the centroid. Along with the conditions of Equation (23) the constants are chosen to make the bending and twist zero as x becomes large.

Timoshenko and Langer^[17] present specific solutions for various cases of loading. In general these solutions are of a localized enough character that stresses produced by nearby wheels do not interact.

For torsion of a rail built into a track, longitudinal stresses near the point of load application are such as would be produced by the forces Q in Figure 15. When twisting of rail occurs, there results a lateral deflection of the head $h_1 \phi$ causing a bending moment in the head and base. Timoshenko and Langer^[17] show these to be simply

$$M_H = -EI_1 h_1 \frac{M_t}{C} \quad (24)$$

and

$$M_B = -EI_2 h_2 \frac{M_t}{C} , \quad (25)$$

respectively.

In summary, it may be said that significant stresses are produced by the action of lateral wheel loads and the eccentric application of vertical wheel loads (i.e., vertical loads applied off the plane of symmetry of the rail). The principal influence of these loads is felt in the rail head as a distortion of the bending stress distribution. This redistribution of stresses arises from both lateral bending of the rail under lateral loading and the warping of the rail cross section caused by the resistance to torsion of the rail under the action of both eccentric, vertical, and lateral loads. For 132-lb RE rail, longitudinal bending stresses due to lateral bending occurring in the extreme fibers of the head and base, under a 10,000-lb lateral load, can reach 11,000 psi and 21,000 psi, respectively. Warping stresses under these conditions can reach 7,000 psi in the rail head and 11,000 psi in the base. The warping stresses arising from the eccentric vertical loads reach comparable magnitudes.

2.4 DYNAMIC FLEXURAL STRESSES IN RAILS

The stresses and deflection in rail from dynamic wheel loads may become much greater than just the static component. Treatments of these problems have been primarily from the standpoint of determining wheel rail loads by studying the dynamic characteristic of the vehicle. These load and tie plate reactions are then applied to the rail quasi-statically in order to determine rail stresses.

2.4.1 Analytical Treatments

An analysis of the effect of low spots in rails (i.e., flat spot on wheels or dips in rails) is presented by Timoshenko and Langer^[17] as referenced in Timoshenko and Lessels^[27].

The vertical displacement of the wheel due to the dynamic deflection of the rail y and the low spot u is $u + y$ and the differential equation of vertical motion of the wheel can be written as

$$\frac{W}{g} \frac{d^2 (u+y)}{dt^2} + \alpha (y+u) = 0 , \quad (26)$$

where v is the speed of the moving wheel and

u = variable depth of low or flat spot

W/g = unsprung mass per wheel

a = $2k/K$ load to produce unit deflection of rail

y = additional, dynamic deflection of rail due to flat spot.

By assuming the shape of the low or flat spot to be

$$u = \frac{\delta}{2} \left(1 - \cos \frac{2\pi x}{l} \right), \quad (27)$$

where

l = length of the low or flat spot

δ = depth of the spot and the middle of its length,

then the solution can be found to be

$$y = \frac{\delta}{2} \frac{1}{1 - \left(\frac{T_1}{T}\right)^2} \left(\cos \frac{2\pi t}{T_1} - \cos \frac{2\pi t}{T} \right), \quad (28)$$

where

T = period of vibration of the rail supporting a wheel set

$T_1 = l/v$, time required for the wheel to cross the low spot.

Figure 15 presents a variety of solutions for the parametric ratio T_1/T . It is seen that the additional deflection is proportional to the flat spot depth. A maximum deflection of 1.47δ is possible when $T_1/T = 2.3$.

In general, the dynamic deflection can be calculated by,

$$y = \frac{g}{W} \frac{T}{2\pi} \int_0^{t_1} F(t) \sin \left[\frac{2\pi(t_1-t)}{T} \right] dt, \quad (29)$$

where $F(t)$ is the contour function of the low spot. Calculations using Equation (29) have shown that the maximum additional dynamic load is about 50 percent more than that which produces a static deflection equal to the depth, δ , of the spot.

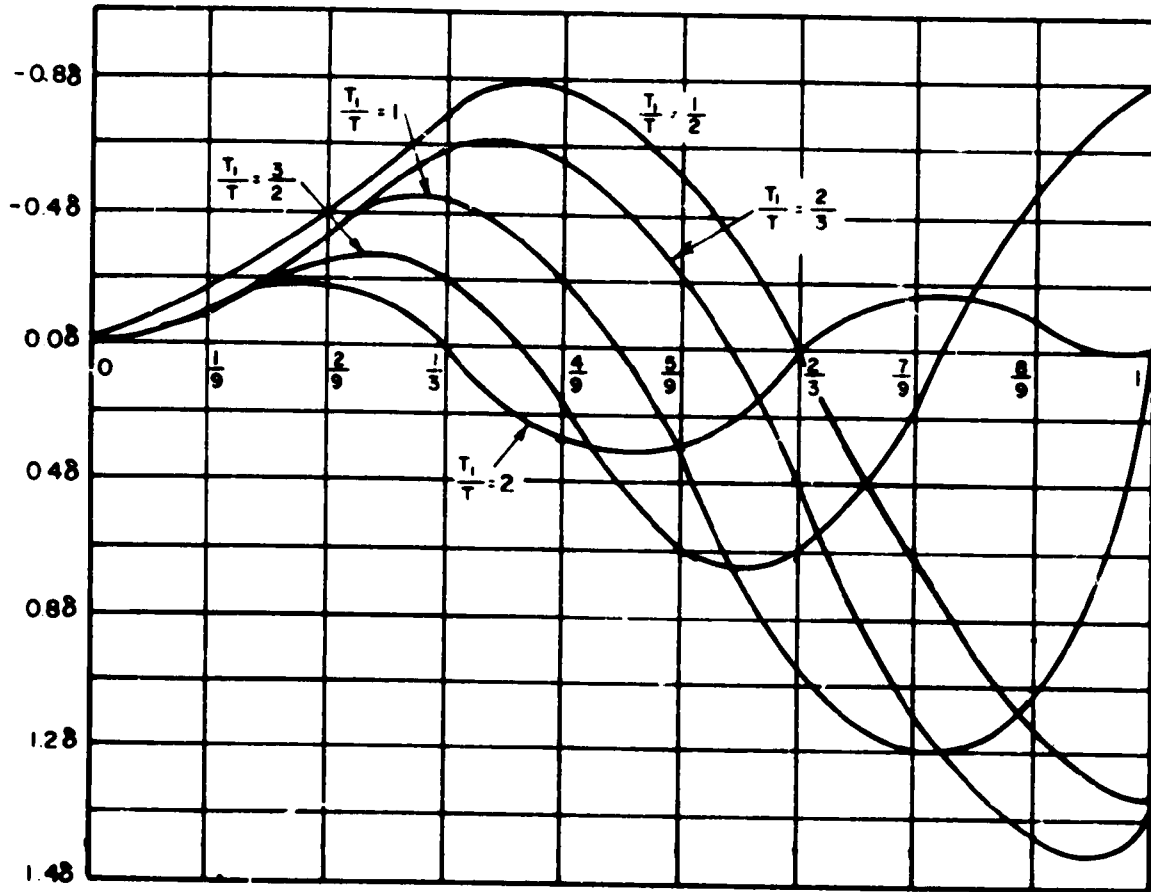


FIGURE 15. ADDITIONAL (DYNAMIC) DEFLECTION PRODUCED BY FLAT SPOT ON WHEEL OR LOW SPOT ON RAIL [17]
 (δ = depth of flatspot; l = length of flat spot; T = period of free vibrations of wheel on rail; T_1 = time for wheel to cross flat spot.)

It should be noted that in this analysis the mass of the rail was neglected. This assumption may lead to error for sufficiently high train speeds, but should be satisfactory at speeds when the time required for a wheel to pass over the flat is small compared with the period of vibration of the rail supporting the unsprung mass.

When wheel loads are applied to the rail impulsively, such as in the case of wheel flats, the mass of the rail adjacent to the contact area between the wheel and rail must be taken into consideration when determining the distribution of stress in that region. In the study of the dynamic response of circular footings, Luco and Westerman^[28] found that the stress distributions beneath a vibrating rigid circular punch on an elastic half space begins to differ from the static solution when

$$\alpha \omega \left[\frac{\rho}{\mu} \right]^{1/2} > 2, \quad (30)$$

where

- ω = exciting frequency
- α = radius of the circular punch
- ρ = density of the rail steel
- μ = shear modulus of the half space.

In order to form an analogy between this problem and the wheel flat against the rail, it must be assumed that $E = 30 \times 10^6$ psi, $\alpha = 0.5$ inch, $\rho = 0.283/386$ slug/in³ and $\mu = 12 \times 10^6$ psi. In so doing, Equation (30) yields that when the forcing frequency is greater than approximately 80 kHz the inertia of the rail adjacent to the contact surface should be accounted for since the effect of the distributed inertia of the half space begins to distort the stress distribution. The significance of this effect is dependent on the energy content above 80 kHz of the impulse load due to impact of the flattened wheel on the rail. To date few data on the energy of wheel flat impulse loads above 10 kHz are available.

The track modulus used throughout the analyses is also assumed to be constant where in fact track modulus is a function of forcing frequencies. The track stiffness refers to the load/deflection ratio for a point load applied to the rail head at a particular forcing frequency. In vibrational analysis of track the term track dynamic compliance is used and is the complex ratio of displacement-to-force. The dynamic compliance represents the frequency dependent transfer function for steady-state sinusoidal excitation. The term compliance or track compliance has been used to indicate forces and displacements measured at the rail head. If the forcing frequency is well below the natural frequency of the system, the track dynamic compliance approaches in magnitude the inverse of the track stiffness. From measurements made of dynamic compliance^[29], Figure 16, it is seen that the statically determined track stiffness is accurate up to forcing frequencies of approximately 50 Hz after which the compliance becomes strongly a function of forcing frequency.

2.4.2 Comparisons Between Calculated and Experimental Results

Magee and Cress^[30] compared these analytical results with experiment. Calculations using the Timoshenko analysis predict dynamic stresses 28 percent in excess of static stress measured in rail base for the same loading condition. This was based on the assumption of a train speed of 5 mph and a flat length of 2.75 inches. As pointed out in Reference [30], the analysis produces a solution in terms of rail deflection; the experimental data are in terms of stress. Small errors in the calculation of the deflected shape can result in large deviations in stress. The results of a study of the effects of flat wheels on track have been also presented in the AREA Proceedings^[31]. The purpose of the investigation was to develop sufficient information on the impact effect of wheel flats to permit the review of regulations regarding the removal of flat wheels from service. Attempts to measure stresses due to flat wheels had begun with the unsuccessful efforts of the Talbot Committee in 1918. The same committee using the more modern equipment which had become available, made similar measurements in 1939 and again in 1942.

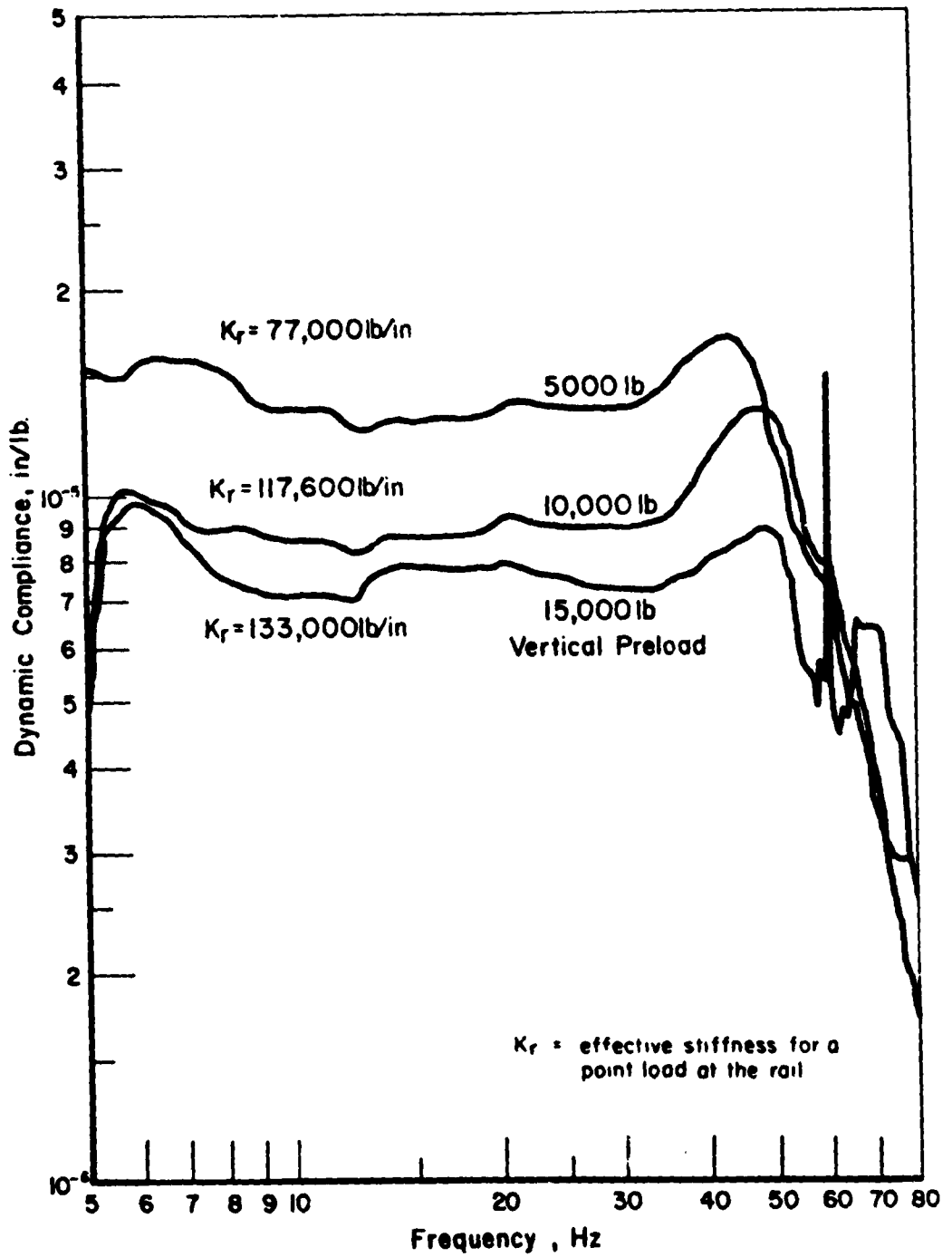


FIGURE 16. DYNAMIC COMPLIANCE MEASURED FOR VARIOUS TRACK STIFFNESSES [28]

The tests detailed in the 1942 report were conducted on a single track, main line of the Chicago and North Western railroad and consisted of 100-lb RA-A and 131-lb RE rail sections laid on gravel ballast. The tie spacing, although irregular, averaged 19 inches. Electrical resistance strain gages were mounted on the rails in the positions indicated in Figure 17 and magnetic oscillographs and associated amplifier channels were used for data recording.

A variety of testing conditions including 2-1/2 to 4-1/2-inch-long ground flat spots were used. Full, half-full, and empty train cars were run over the test rails at speeds from 5 to 90 mph. Tests were also conducted with both wheels of an axle flat and with rounded-corner wheel flats. Figure 18 presents the wheel contours utilized. Figure 19 shows a typical record of traces resulting from the various strain gages due to the passage of round wheels. Figure 20 shows the same traces for the passage of a flat wheel. Considerable amplification in stress is noted.

Figure 21 presents rail bending stress for various vehicle speeds (at the base underside centerline) for several flat spot dimensions. It is seen that flat spot stresses increased rapidly from speeds of about 5 mph and reached a peak at about 20 mph. Stresses remained relatively constant above this speed until 40 mph was reached. Flat spot stress (in the base) is seen to decrease at speeds greater than 40 mph. This effect is particularly noticeable in the cases of light rail or high wheel load.

This figure also demonstrates how impact stress increases significantly with the length of the flat spot. It should be noted that the tests with rounded corner flat spots showed clearly that the depth of the flat was the primary factor as is predicted by the preceding analysis.

Magee and Cress^[30], in the report previously mentioned, present a plot of resultant stress at several points in the rail due to the action of flat wheels. This is of particular interest since the stresses in the rail web are greater than those in the base. Figure 22 presents a plot of stresses measured in the web as compared with those in the base. It is interesting to note that the maximum stresses were found to occur ahead of the wheel rather than directly beneath it. It could actually be that the maximum load is seen when this front edge of the flat contacts the rail. Unfortunately, no results are presented for rail head stresses.

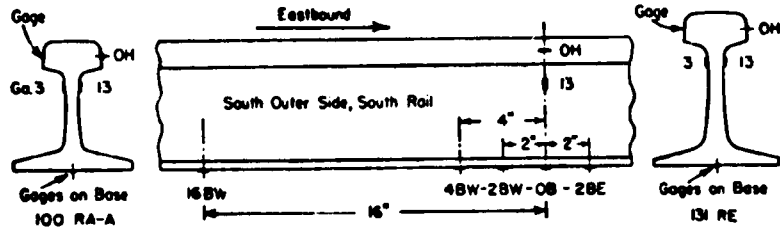


FIGURE 17. LOCATION OF STRAIN GAGES ON RAILS

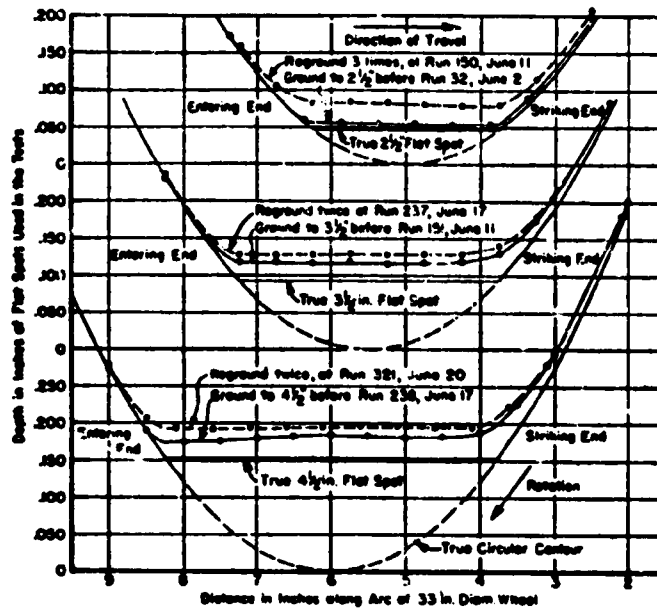


FIGURE 18. PROFILES OF THE THREE LENGTHS OF GROUND FLAT SPOTS ON A 33-IN. WHEEL. Profiles shown are before and after test runs.

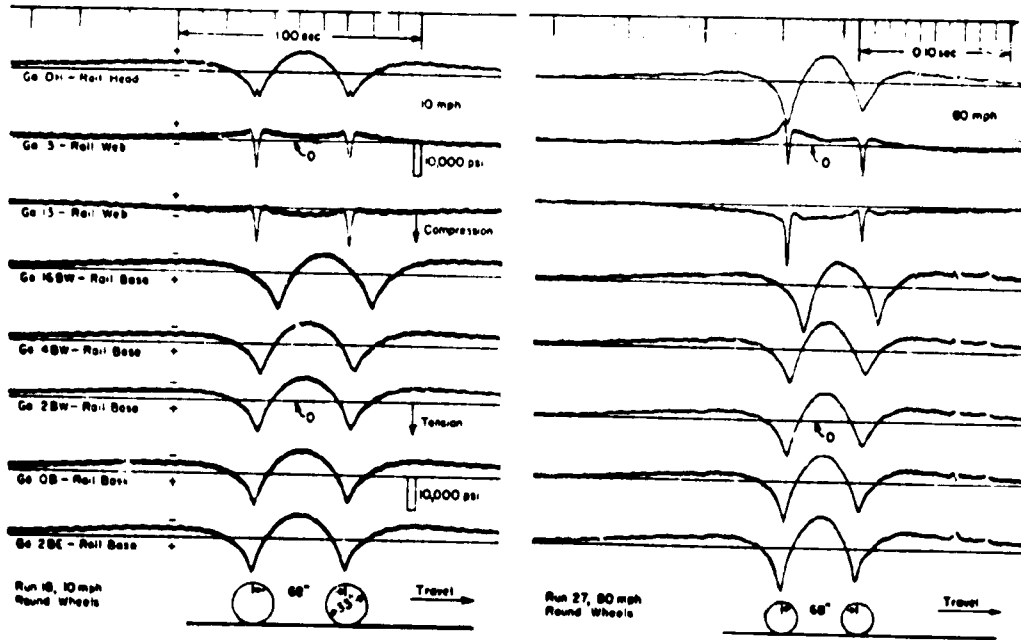


FIGURE 19. TYPICAL RECORDS OF RAIL STRESS AT 10 AND 80 MPH WITH ROUND WHEELS - FULL LOAD, 100-LB. RAIL

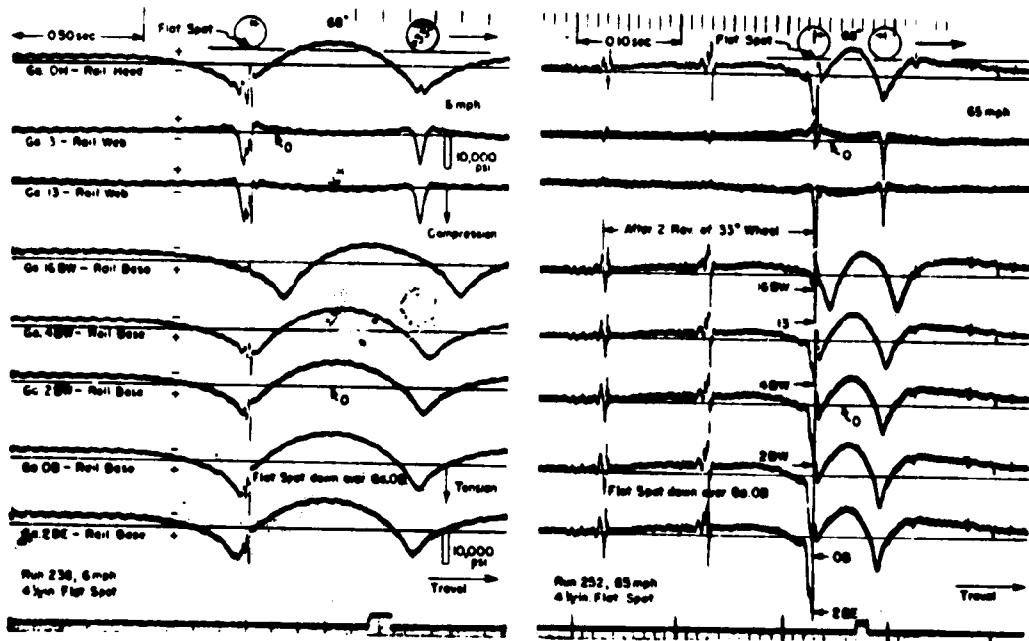


FIGURE 20. TYPICAL RECORDS OF RAIL STRESS AT 6 AND 65 MPH WITH 4-1/2-IN. FLAT SPOT-FULL LOAD, 100-LB. RAIL [32]

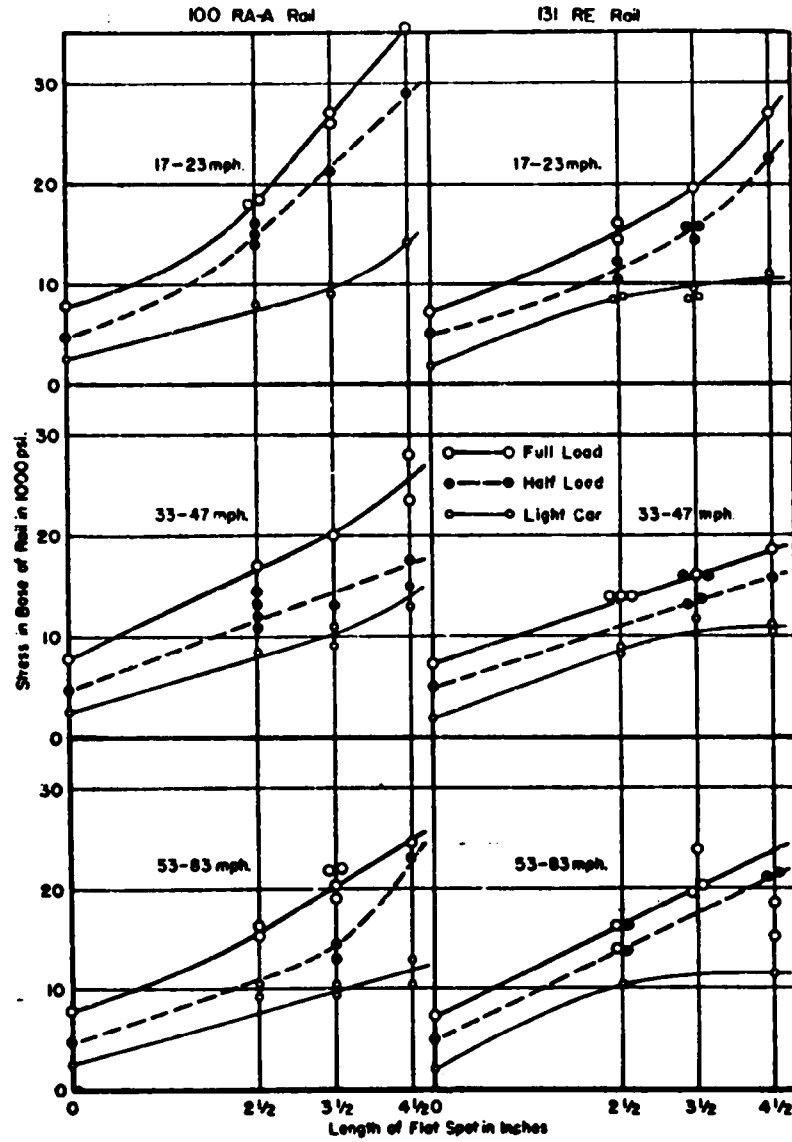


FIGURE 21. LONGITUDINAL STRESS IN RAIL BASE DUE TO FLAT SPOTS AT THREE RANGES OF SPEED AND THREE LOADS - 100-LB and 131-LB RAILS [32]

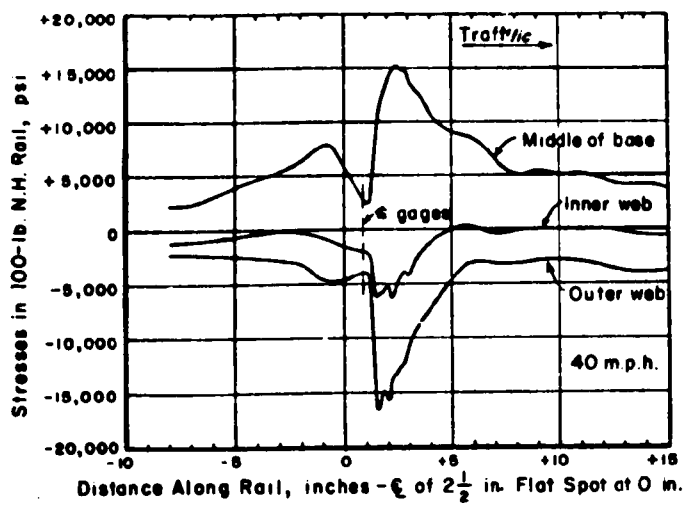


FIGURE 22. SIMULTANEOUS STRESSES IN THE BASE AND IN THE INNER AND OUTER WEB FACES OF A 100-LB N.H. RAIL AS A 33-INCH WHEEL WITH A 2-1/2-INCH FLAT SPOT MOVES PAST THE GAGES

3. STRESS CONCENTRATIONS--WEB AND FILLET STRESSES

3.1 INTRODUCTION

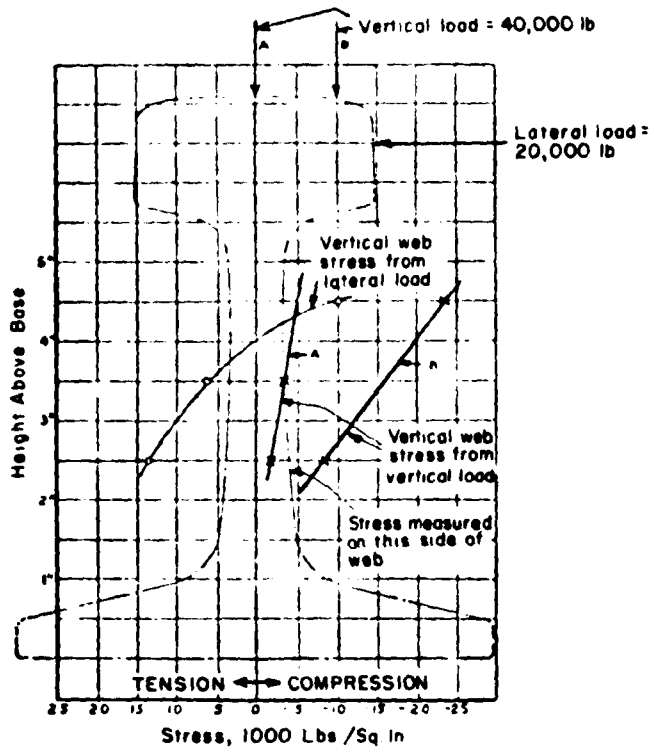
A rail section design makes efficient use of the steel in resisting flexural loads. In this regard rails are like similarly designed structural members, I-beams and WF beams, in that the head and base are separated by a much thinner web section. In vertical bending this geometry is most efficient; however, when lateral loads, vertical load eccentricities, or torsional loads are applied the sudden transition in geometry of the head to web is a location of stress concentration. A concentration of stress also occurs at the head/web intersection due to the rapid change in geometry under pure vertical load.

Numerous studies have been conducted on specific problems of high head web fillet stresses. Subsequent redesign of rail cross sections have eliminated many of the early problems.

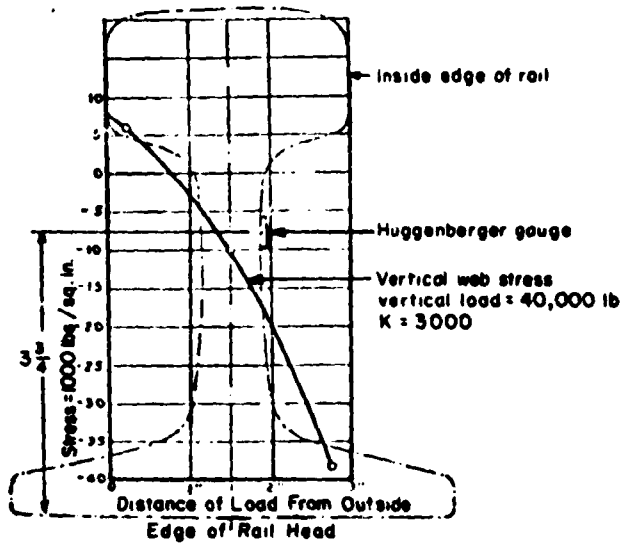
3.2 SUMMARY OF PREVIOUS EXPERIMENTAL STUDIES

The majority of investigations of fillet stresses have been via experimental approaches. Timoshenko and Langer^[17], via extensometric measurements determined web vertical stress for several loading conditions for PS 130-lb and PS 131-lb rails, Figures 23a and 23b, respectively. They also presented results of two-dimensional photoelastic results on PS 130 rail for the same loading conditions, Figure 24. Here, however, the load was adjusted to account for the missing restraint of the three-dimensional rail. A maximum stress of 34,950 psi is observed in the upper fillet on the load side.

Similar results were obtained by Leaf^[33], using a two-dimensional photoelastic model in a later study, Figure 25. This work was conducted on a 112-pound RE rail using a 1-inch offset 37,000-pound load. Adjustments were made for planar nature of the model (as in Timoshenko and Langer). Figure 25 presents the results together with typical strain gage measurements taken from actual, in-service, track. A very high stress of 60,000 psi was



a. Combined Loading of PS131 Rail - Vertical Stress



b. Vertical Loading of PS130 Rail - Vertical Stress

FIGURE 23. WEB VERTICAL STRESSES IN PS130 AND PS131 RAIL [17]

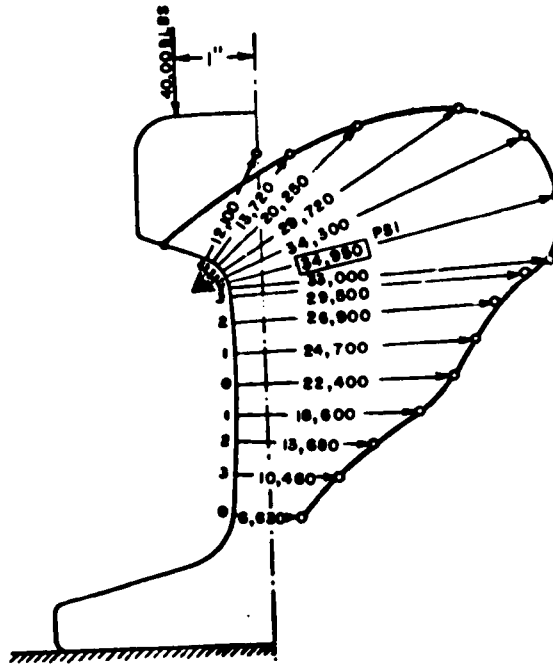


FIGURE 24. CONNECTED PHOTOELASTIC DETERMINATION OF TANGENTIAL STRESS IN P&130 RAIL (TIMOSHENKO AND LANGER [71])

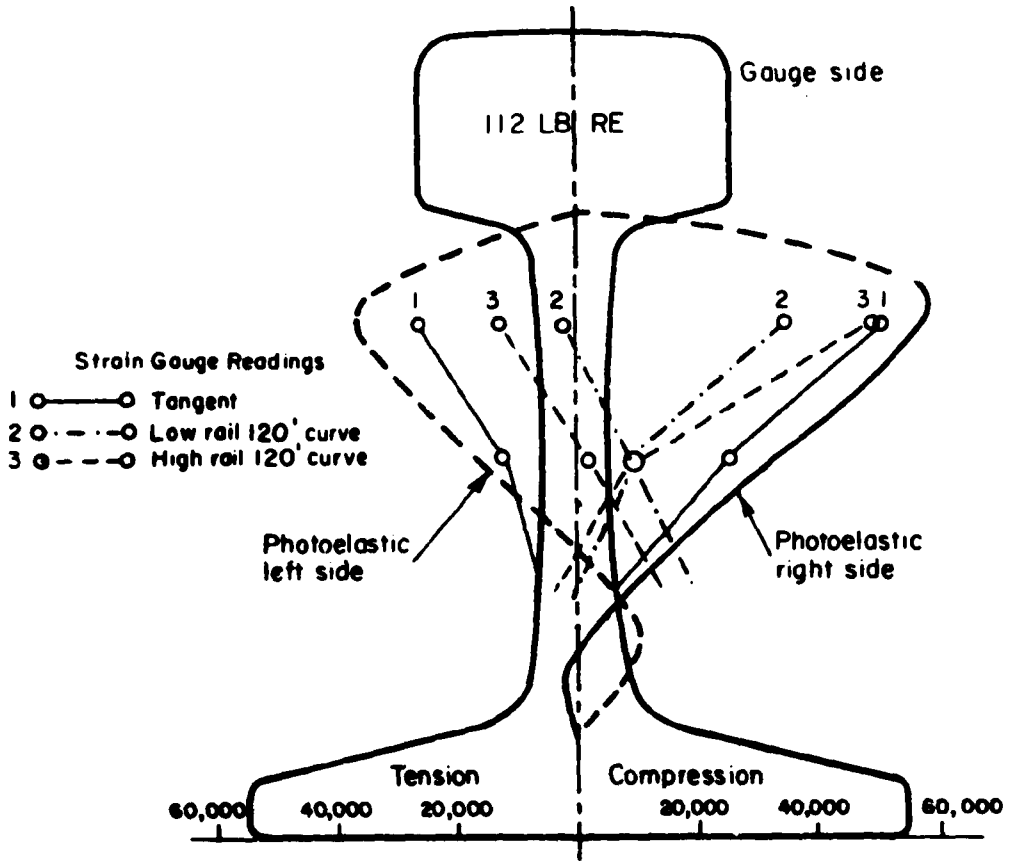


FIGURE 25. WEB AND FILLET STRESS IN 112-LB RE RAIL^[33]

observed on the gage side, upper fillet region. This result seems to be in reasonable agreement with the Timoshenko and Langer measurements on the PS 130-lb rail. Leaf concluded that the rail should be redesigned to thicken the upper web portions to reduce the excessive fillet stress. It is interesting to note that Timoshenko and Langer reached the same conclusions, based on substantially identical results, some 10 years earlier.

More recently, similar work was conducted by Miyairi and Sasaki^[34] on a variety of rail sections from different countries; German, American, and Japanese profiles were used. One-half scale epoxy resin models were fabricated of the various profiles. Comparisons of resulting stress were made for several loading case combinations. The results of this work were given in a rather qualitative fashion, and therefore will not be presented here.

The results of a study of static web and fillet stresses in five rail sections were presented in the APEA Proceedings in 1945^[35]. The rail sections investigated were

- (1) 112-lb RE Rail
- (2) 115-lb Rail Proposed by Leaf^[33]
- (3) 112-lb "Torsion Resisting" Rail
- (4) Redesign of 115-lb Rail Section A
- (5) 131-lb RE Rail.

The rails were tested in a special yard track at Proviso, Illinois. Strain gages were applied to each rail section. Loading was applied with a flat car having 20,000- and 40,000-lb wheel loads. The gage of the rail and the condition of the wheel were varied so as to produce a variety of lateral and vertical load combinations. The eccentricity of the load on the rail head was determined by loading through a 1/8-inch steel wire which could be moved laterally across the rail head. The results of the 112-lb RE and 131-lb RE rail tests are shown in Figures 26 and 27, respectively.

It was noted that measurable distortions of the underside of the rail head and upper web fillet occurred with residual compressive stresses of 10,000, 25,000 psi being observed at those points, respectively. Since the stresses at these locations were insufficient to cause yielding in themselves, it was concluded that the residual stresses were due to plastic flow within the rail head; presumably from the contact zone.

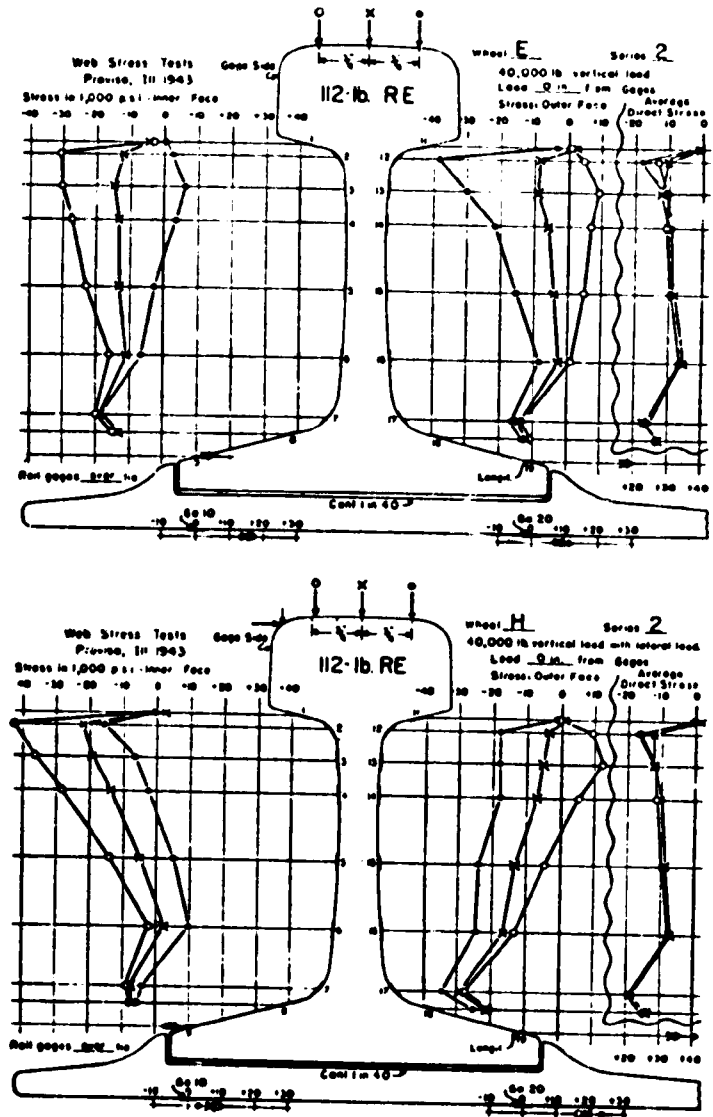


FIGURE 26. MEASURED STRESSES IN 112-LB RE RAIL OVER MIDDLE OF TIE FOR STATIC LOAD OF 40,000-LB CONTROLLED LOADING CONDITIONS AS INDICATED ON RAIL HEAD [35]

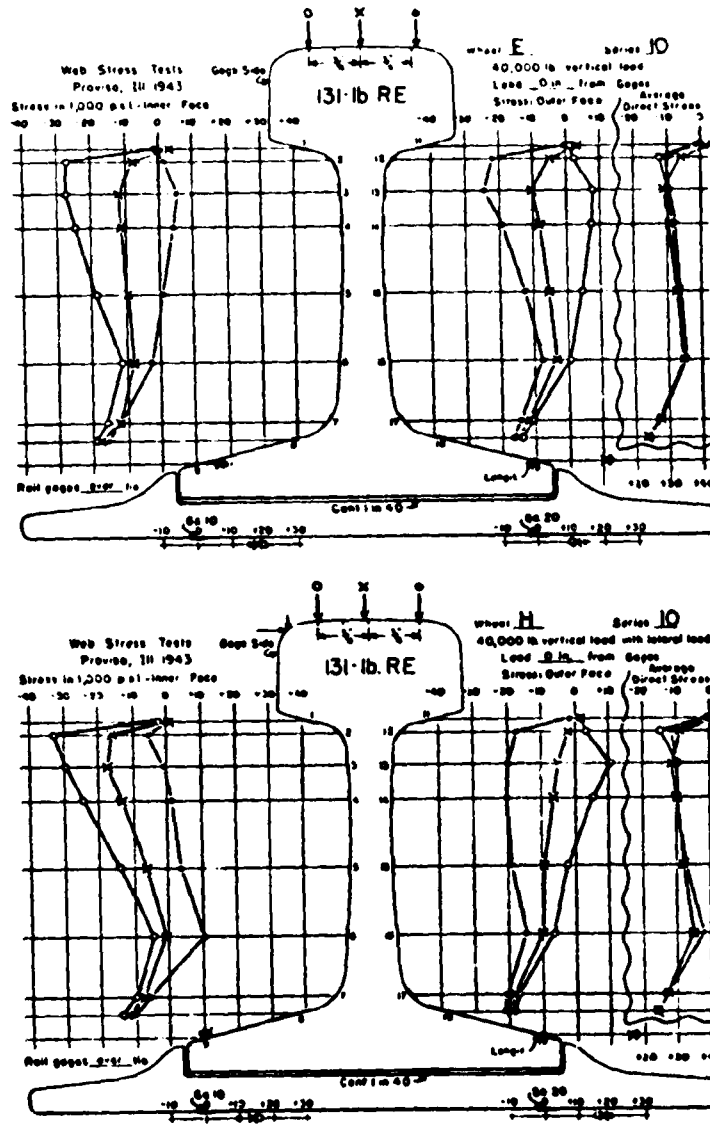


FIGURE 27. MEASURED STRESSES IN 131-LB RE RAIL OVER MIDDLE OF 11E FOR STATIC LOAD OF 40,000-LB CONTROLLED LOADING CONDITIONS AS INDICATED ON RAIL HEAD^[35]

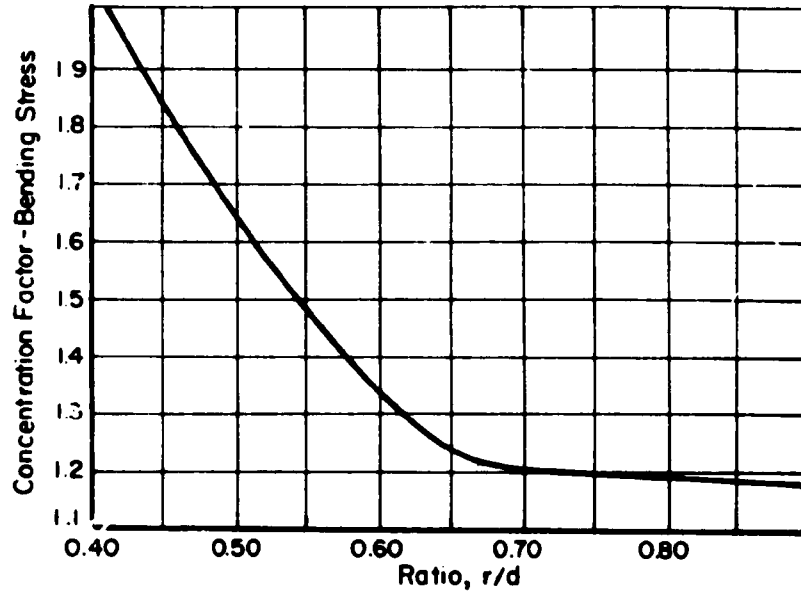
3.3 CALCULATION OF FILLET STRESSES

In 1947, Code^[36] presented an empirical method for calculating maximum web stresses due to eccentric vertical load. Code presents empirical curves for stress concentration factors to be applied to the bending and direct stresses as a function of r/d (ratio of fillet radius to web thickness), Figures 28a and 28b. For the purpose of calculation Code presents the results for a 20,000-lb load and an eccentricity of 3/4 inch. From the torsional rigidity and moment of inertia, the bending moment and direct stress on a 1-inch length of web are determined from Figures 29a and 29b, respectively. This moment and stress are adjusted depending upon the thickness of the web at the point of interest. Then the appropriate stress concentration factor from Figure 28 is applied.

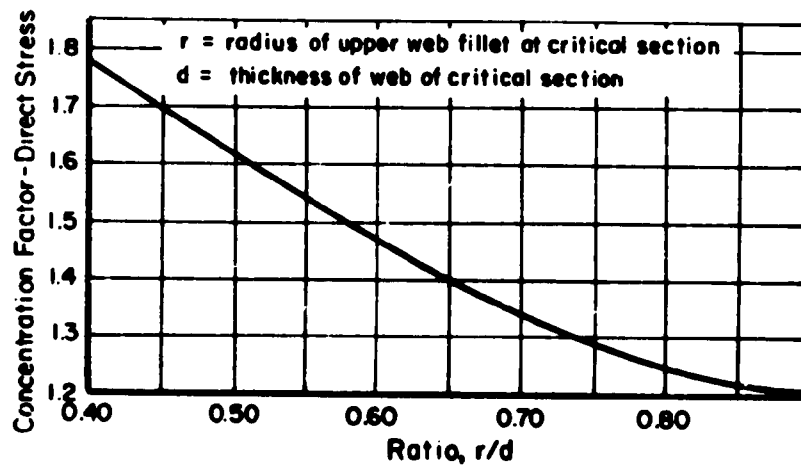
Code suggested that for other loads, the stress can be determined by applying a direct proportion to the stress due to a 20,000-lb load. For eccentricities other than 3/4 inch, a direct proportion to the bending stresses is suggested. Code stated that the results may be expected to be within 5 percent of the true stress.

3.4 EFFECTS OF WEAR ON WEB AND FILLET STRESSES

In 1965, Babb^[37] presented an in-depth study of web stresses for new and worn British rail sections. A similar study had been done in 1961 by AAR^[38] on a number of CF&I and AREA sections. These sections were compared on the basis of flexural stiffness and strength, head contour, head depth, and web and fillet stresses. The latter item, particularly with respect to head wear, is of interest. Rail sections studied included 100, 115, 132, 140-lb RE, 116, 119, 136-lb CF&I, 131-lb NYC. Test rails were planed to simulate head wear; the depths of simulated wear chosen were 3/8 and 3/16 inch, with a 9-inch head radius maintained. It was felt that the "worn" contour thus obtained provided a reasonable simulation of in-service worn conditions.

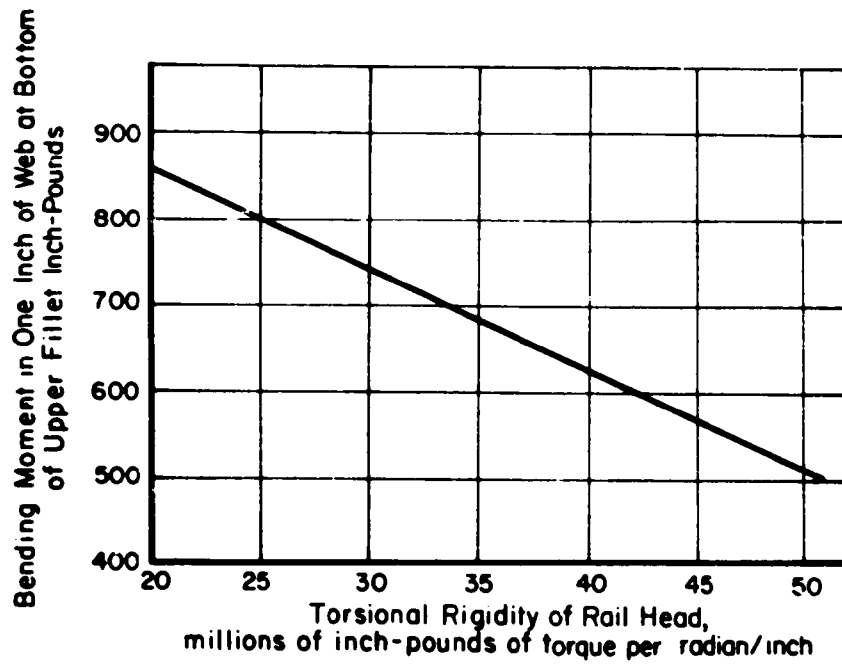


a. Concentration Factors for Bending Stress in Upper Web Fillet of Rail

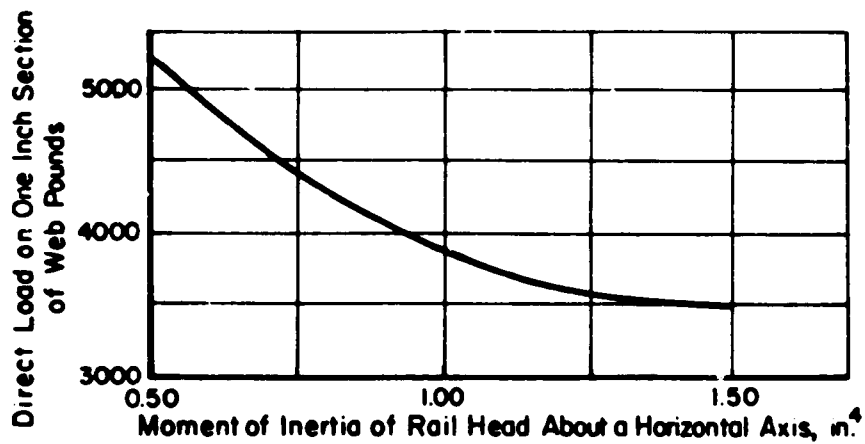


b. Concentration Factors for Direct Stress in Upper Web Fillet of Rail

FIGURE 28. STRESS CONCENTRATION FACTORS FOR BENDING AND DIRECT STRESS [22]



a. Bending Moment Top Web Fillet 20,000-lb. Load 3/4 in. off Center



b. Direct Load on 1-in. Section of Rail Web 20,000-lb. Load

FIGURE 29. BENDING MOMENT AND DIRECT STRESS FOR RAIL SECTION [36]

The test rail sections were 6 feet long. Test rails were supported by tie plates resting on plywood ties spaced at 18-inch centers, and the entire track assembly rested on a cellotex pad on plywood. The support system created an effective track modulus of about 1600 lb/in./in. A 40,000-lb load was used in all cases.

The maximum ranges of stress in the upper fillet area were measured for all of the sections in various stages of wear and are presented in Table 5. Figures 31 through 33 present web and fillet stresses as a function of depth of the rail for the AREA Sections. The nonworn sections for 132 RE compare closely to that for 131 RE in Figure 27 as can be seen, wear has the effect of substantially increasing web and fillet stresses. In Figure 34 is shown the web and fillet stresses for all sections tested versus calculated stresses.

A large amount of data exists, taken primarily from field evaluations, on this topic. AREA proceedings^[16] contains the most of these data.

TABLE 5. MAXIMUM RANGE OF MEASURED STRESS IN THE UPPER FILLET AREA^[38]

Condition of Rail (a)	Range of Stress (10^3)	Total Range	Ratio to End. Limit (b)
100 RE			
Full Head	-42 to +8	50	0.67
3/16 in. Sim. Wear	-49 to +10	59	0.79
3/8 in. Sim. Wear	-62 to +17	79	1.05
106 CF&I			
Full Head	-32 to +6	38	0.51
3/16 in. Sim. Wear	-36 to +9	45	0.60
3/8 in. Sim. Wear	-43 to +12	55	0.73
115 RE			
Full Head	-31 to +4	35	0.47
3/16 in. Sim. Wear	-36 to +6	42	0.56
3/8 in. Sim. Wear	-43 to +9	52	0.69
119 CF&I			
Full Head	-27 to +5	32	0.43
3/16 in. Sim. Wear	-31 to +6	37	0.49
3/8 in. Sim. Wear	-37 to +7	44	0.59
132 RE			
Full Head	-29 to +4	33	0.44
3/16 in. Sim. Wear	-33 to +5	38	0.51
3/8 in. Sim. Wear	-38 to +7	45	0.60
136 CF&I			
Full Head	-25 to +3	28	0.37
3/16 in. Sim. Wear	-28 to +4	32	0.43
3/8 in. Sim. Wear	-31 to +5	36	0.48
136 NYC			
Full Head	-23 to +2	25	0.33
140 RE			
Full Head	-23 to +2	25	0.33
3/16 in. Sim. Wear	-26 to +3	29	0.39
3/8 in. Sim. Wear	-31 to +5	36	0.48

(a) 40,000-lb load statically applied with 3/4-in eccentricity each side of the center of the rail head.

(b) Endurance limit taken as -60 to +15. See AREA Proceedings, Vol 51, page 637.

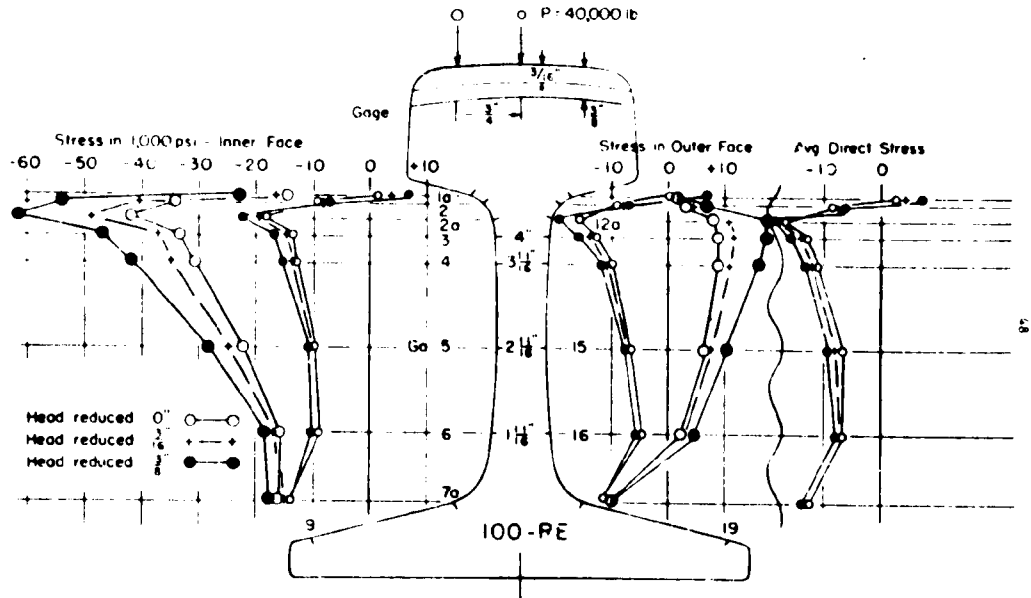


FIGURE 30. MEASURED WEB AND FILLET STRESSES IN THE WEB OF 100 RE RAIL WITH CONCENTRIC AND ECCENTRIC LOADING [38]

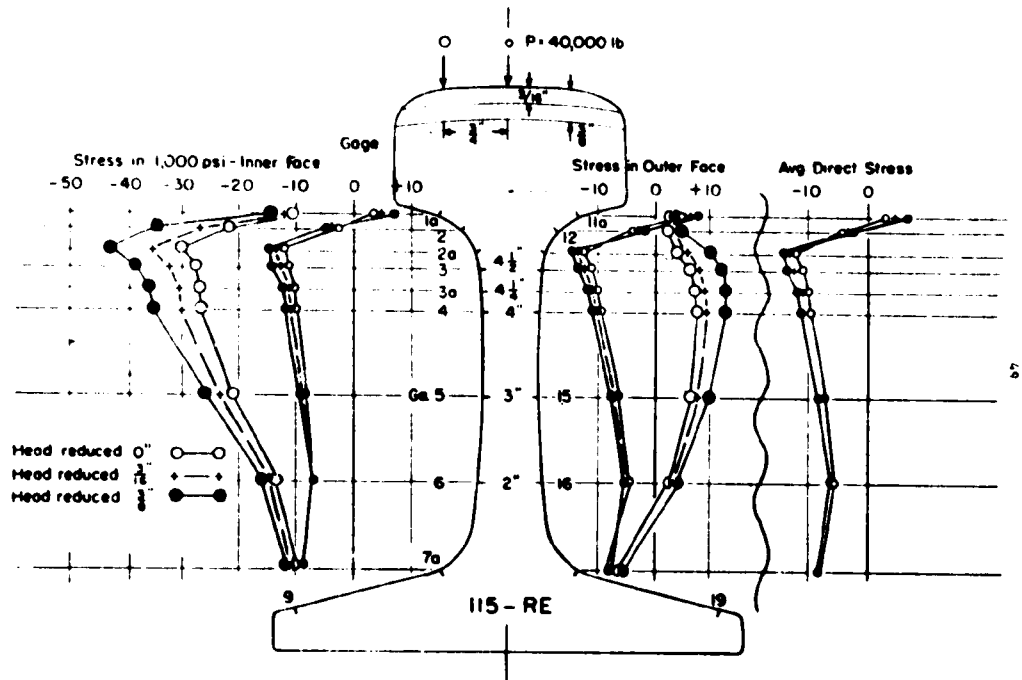


FIGURE 31. MEASURED WEB AND FILLET STRESSES IN THE WEB OF 115 RE RAIL WITH CONCENTRIC AND ECCENTRIC LOADING [38]

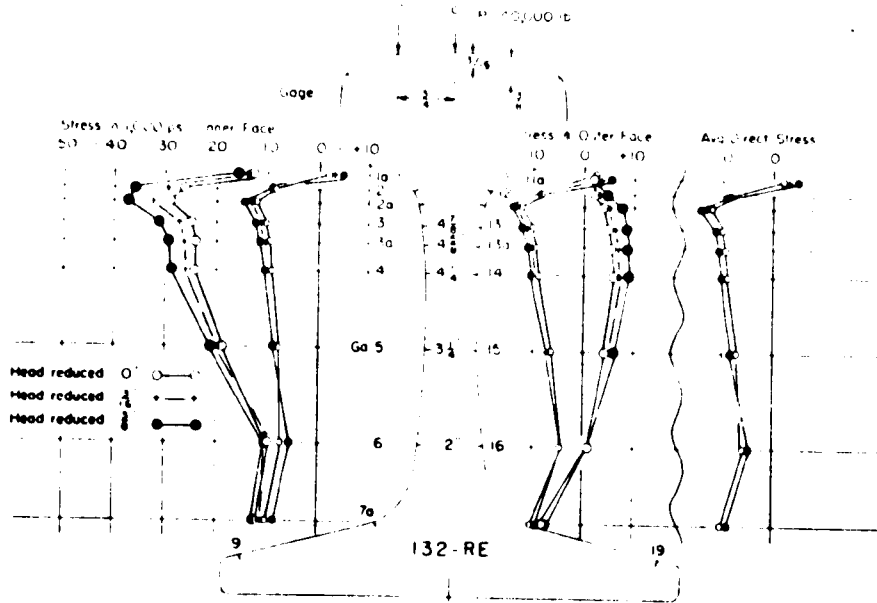


FIGURE 32. MEASURED WEB AND FILLET STRESSES IN THE WEB OF 132 RE RAIL WITH CONCENTRATED ECCENTRIC LOADING[38]

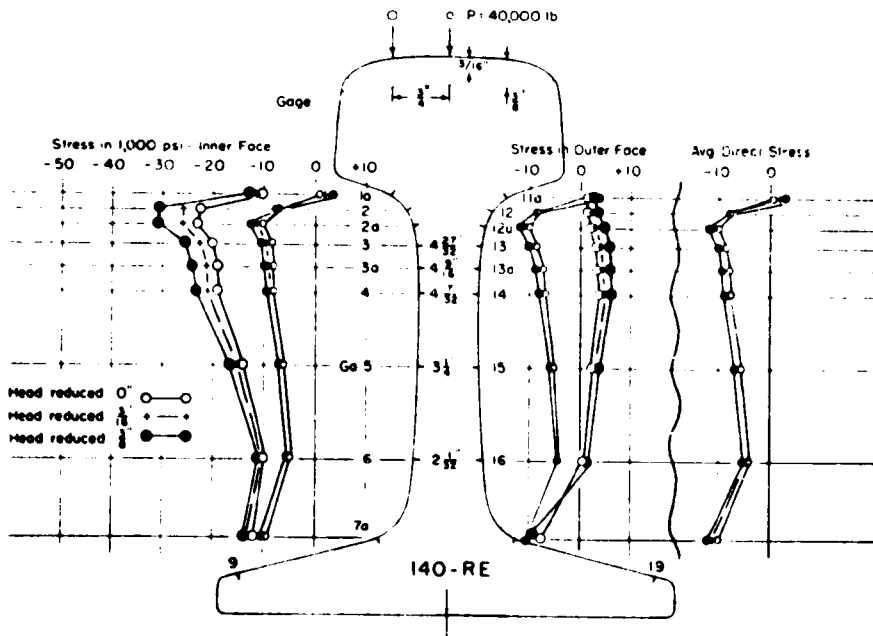


FIGURE 33. MEASURED WEB AND FILLET STRESSES IN THE WEB OF 140 RE RAIL WITH CONCENTRIC AND ECCENTRIC LOADING[38]

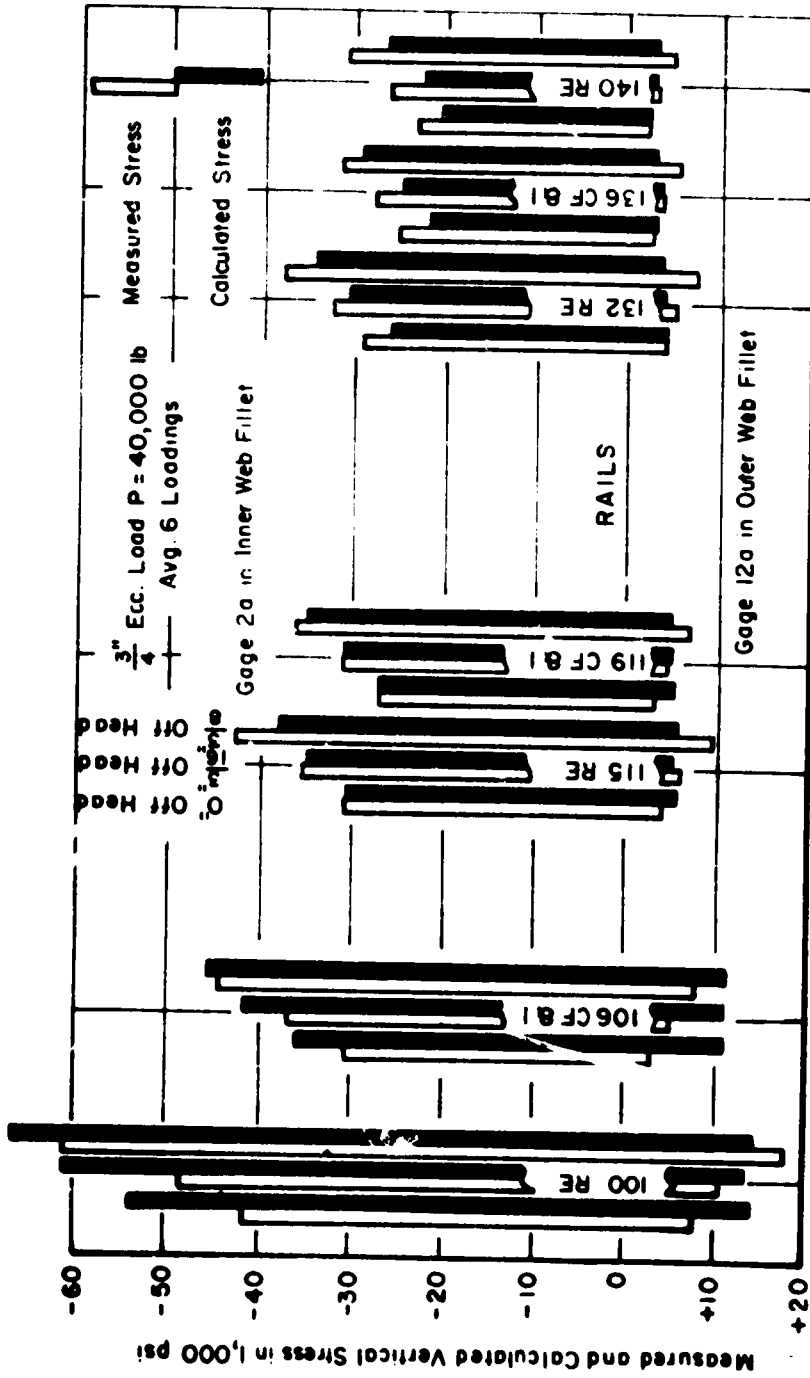


FIGURE 34. COMPARISON OF MEASURED AND CALCULATED VERTICAL STRESSES AT GAGE LOCATIONS 2a - 12a IN THE UPPER WEB FILLETS WITH 3/4-INCH ECCENTRIC LOAD OF 40,000-LB [38]

4. THERMAL STRESSES

4.1 DISCUSSION

It has been generally accepted that stresses due to thermal expansion and contraction of the rail are small in comparison with those caused by the wheel loads. However, these have been of major concern when the stability of the rail is considered since these stresses do influence the equilibrium of the rail structure in a parametric sense. Furthermore, there is the possibility that rail rollover tendencies are increased with increased longitudinal thermal stress. Thermal expansion in relation to buckling of continuous welded rail (CWR) has, therefore, been a subject of considerable recent interest. According to Kerr^[19], buckling of jointed rail is quite possible and was reported as early as 1927 by Wohr^[39]. Kerr^[40,41] has examined the horizontal and vertical buckling of long rails in considerable detail.

Relatively little attention has been directed in the literature to the question of thermal stresses in rails. The following discussion outlines some of the analytical approaches that have been prepared.

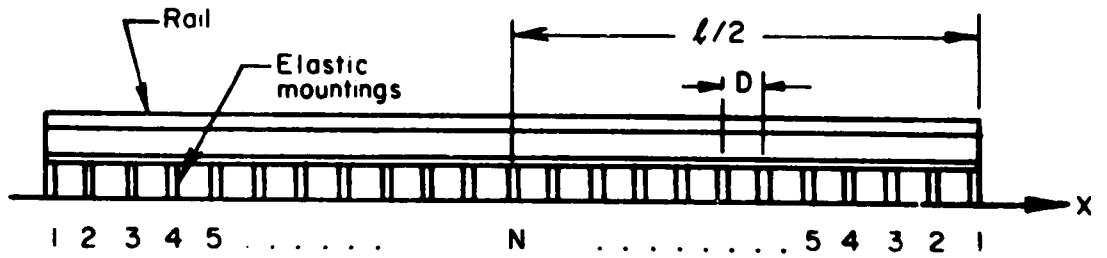
Varga^[14] has presented an analysis of the thermal elongation of rails on elastic fasteners. Two methods of analyses were derived; a discrete restraint approach and a continuous restraint approach.

The discrete approach assumes the rail model to have $(2N-1)$ supports as shown in Figure 35. Varga distinguishes the case of creep, i.e., when the rail at a particular location slips from the fasteners, from that of simple elongation. The longitudinal stiffness of each mounting is,

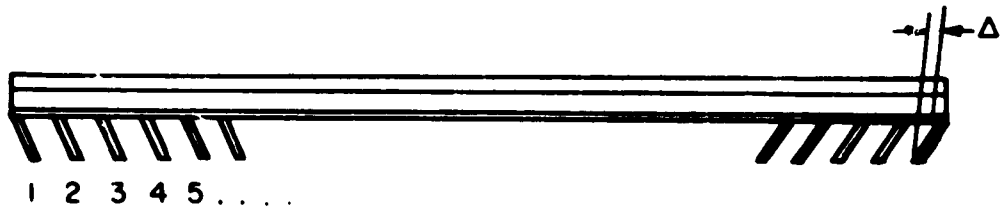
$$Q = F/\Delta \quad , \quad (31)$$

where Δ and F are the deflection and force upon the mounting, respectively. The pitch of the mountings is given by

$$D = \frac{L}{2N-1} \quad . \quad (32)$$



a. Undeflected Rail and Fasteners



b. Deflected Rail and Fasteners

FIGURE 35. RAIL MODEL FOR THERMAL ELONGATION

It can be shown that the force on the p^{th} mounting from the end is

$$F_p = F_1 \sum_0^{p-1} \binom{p+i-1}{2i} K^i - QDc \sum_0^{p-2} \binom{p+j-1}{2j+1} K^j \quad (33)$$

where the bracketed factorial quotients are in the visual notation of the binomial coefficients. The greatest compressive force occurs on either side of the center (N^{th}) rail mounting and has the value,

$$F_{\max} = QDc \left\{ \frac{\left[\sum_0^{N-2} \binom{N+i-1}{2i+1} K^i \right]^2}{\sum_0^{N-1} \binom{N+j-1}{2j} K^j} - \sum_0^{N-3} \binom{N+k-1}{2k+2} K^k \right\} \quad (34)$$

where $K = QD/EA$, $c = \alpha \Delta t$, α is the coefficient of thermal expansion and Δt is the temperature change.

A simpler analysis is possible if the assumption of a continuously distributed rail resistance is made. If Q/D is the longitudinal resistance per unit length, then the governing differential equation for longitudinal strain ϵ is

$$\frac{d^2 \epsilon}{dx^2} = u^2 \epsilon$$

where

$$u^2 = \frac{Q}{EAD}$$

(35)

which has the solution,

$$\epsilon = \frac{1}{u} \frac{\sinh(ux)}{\cosh\left(\frac{ul}{2}\right)}$$

The force on the p^{th} load mounting is given by

$$F_p = cEa \left\{ \cosh[(p-1)uD] - \cosh(puD) + \right. \\ \left. + \tanh(ul/2) \{ \sinh(puD) - \sinh[(p-1)uD] \} \right\} \quad (36)$$

The maximum compressive stress occurs at the center of the rail and is

$$\sigma_c = E \left(1 - \frac{\cosh(ux)}{\cosh(u\ell/2)} \right) \quad (37)$$

or for a very long rail,

$$\lim_{\ell \rightarrow \infty} \sigma = Eac = E\alpha\Delta t \quad (38)$$

Thus, the thermal elongation is completely constrained at the center of a very long rail.

A similar procedure may be followed for the continuously constrained creeping rail. In fact, the force at the mid-rail is found to be

$$F_o = \frac{\ell F_s}{b} + \left[EA - \frac{\ell F_s}{b} \right] \left[1 - \frac{1}{\cosh[u(\ell/2 - 2)]} \right] \quad (39)$$

once again

$$\lim_{\ell \rightarrow \infty} F_o = E\alpha\Delta t \quad (40)$$

which is the same as was obtained for the non-creep case.

Varga^[33] also presents an application of the method to a track structure in the Delft.

4.2 EFFECT ON TOTAL STRESS STATE

The presence of elastic rail mountings has the effect of constraining the thermal expansion of the rail. The maximum thermal stress that can develop is that given by Equation 38. To illustrate the magnitude of stresses involved, it is useful to perform a few calculations for the maximum stress that could be developed. Let $E = 30 \times 10^6$ psi, and assume $\alpha = 6.39 \times 10^{-6}/^\circ\text{F}$. Figure 36 presents axial thermal stress as a function of temperature variation. It is observed that a 68 F temperature variation (a reasonable range for a moderate northern climate) would produce a thermal stress of 6900 psi. Although this is a relatively small stress, it may become significant in conjunction with other stresses.

Reports 7 and 9 of the ORE C53 series incorporate Equation (38) in a general rail stress computer program. In this study, Δt was taken to be 104 F, and the resulting stress is 13,800 psi.

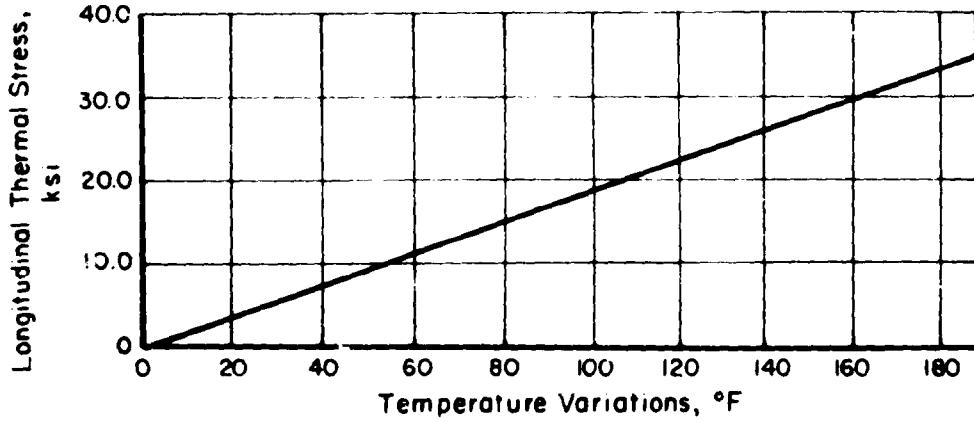


FIGURE 36. THERMAL STRESS AS A FUNCTION OF TEMPERATURE VARIATION FOR TOTAL RESTRAINT ($\sigma = E\alpha\Delta t$)

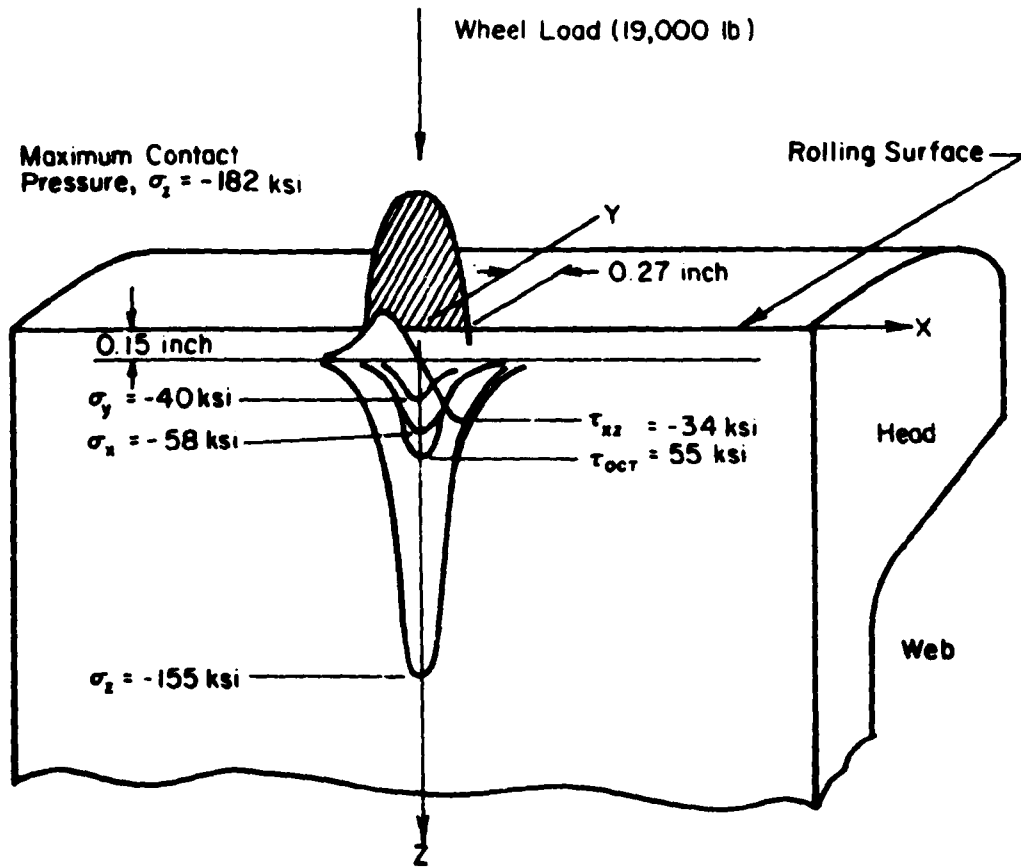


FIGURE 37. STRESSES DEVELOPED IN 132-LB RE RAIL HEAD AT DEPTH OF 0.15 INCH DUE TO 33-INCH DIAMETER WHEEL AND WHEEL LOAD OF 19,000 LB

5. CONTACT STRESSES IN RAIL

The contact pressure between the rail and the wheel is of importance in the study of plastic flow and fatigue life of both the rail head and the wheel. The elastic and plastic deformation of the head produced by contact pressure may also hasten the development of certain types of rail flaws. During the passage of the wheel, the contact stresses reach a maximum and return to nearly zero within a short distance of the loaded area. Typically, this loaded area is elliptical, having its long axis of 0.5 to 0.75 inches, along the length of the rail as shown in Figure 37. The maximum stress in absolute magnitude occurs on the rolling surface directly beneath the load. The worst stresses from the standpoint of yielding, however, (the octahedral shearing stress τ_{oct}) and from the standpoint of fatigue (an alternating transverse shear τ_{xz}) both reach their respective maximum values beneath the rolling surface. For the example in Figure 37, the location of maximum τ_{oct} is approximately 0.15 inch directly below the center line of the wheel; the location of maximum τ_{xz} is at a depth of approximately 0.12 inches from the rolling surface and occurs beneath the front and rear edge of the loaded contact area. Contact stresses may be the most important but are perhaps the least understood of the stress components.

5.1 NORMAL ELASTIC CONTACT STRESSES

While the initial contact between a wheel and rail is determined by the geometric features of the bodies, the final contact area is determined by the amount they are elastically and plastically deformed by the applied forces. The stresses developed during the elastic contact of wheels and rail have long been of great concern to the railroad industry. The general theory of contact of elastic bodies was formulated by Heinrich Hertz^[43] in 1881. Hertz assumed the bodies to be flat enough in the neighborhood of the area of contact to be treated by analytical methods of potential theory available for semi-infinite half spaces. His solutions, arrived at by means of the semi-inverse method, have long served as the basis for evaluating contact stresses.

The first extensive evaluation of the stress field arising in general Hertzian contact is due to Belyayev^[44]. Many other papers which came later expanded upon these results. Those include the works of Dinnik^[45], Way^[46],

Karac^[47], Radzimovsky^[48], Palmgren^[49], Thomas and Hoersch^[50], Weibull^[51], Lundberg and Odqvist^[52], and Fessler and Ollerton^[53]. A concise summary of Hertzian contact theory may be found in Seely and Smith^[54].

Instead of using the exact expression for the three-dimensional geometry of a wheel and rail, the Hertzian theory approximates the wheel and rail as semi-infinite bodies whose separation f between corresponding points on the wheel and rail is

$$f = Ax^2 + By^2 \quad (41)$$

where x and y correspond to the longitudinal and lateral directions, respectively, Figure 38. A and B are surface-defining parameters which depend upon the crown radius and wheel radius and are given by

$$\begin{aligned} A &= \frac{1}{2R_2} \\ B &= \frac{1}{2R_1} \end{aligned} \quad (42)$$

where R_1 and R_2 are the crown and wheel radii, respectively. If w_1 and w_2 represent the deformations of each of the two bodies, at any point within the contact area the sum of these deformations is given by

$$w_1 + w_2 = \alpha - Ax^2 - By^2 \quad (43)$$

where α is the approach of the two bodies or distance they move toward each other. It is noted that by neglecting effects of bending of the rail and wheel, Equation (43) has the same form as that of the Newtonian potential equation for the attraction of a homogeneous mass M in the shape of an ellipsoid upon a unit of mass concentrated at a point P some distance from the ellipsoid. This Newtonian potential function satisfies the same differential equations which are required to be satisfied in the potential function method of the theory of elasticity. The solution is given in terms of elliptic integrals which have been solved and tabulated.

The contact region is elliptical having major and minor principal axis a and b , respectively, where

$$\frac{x^2}{a^2} + \frac{y^2}{b^2} = 1 \quad (44)$$

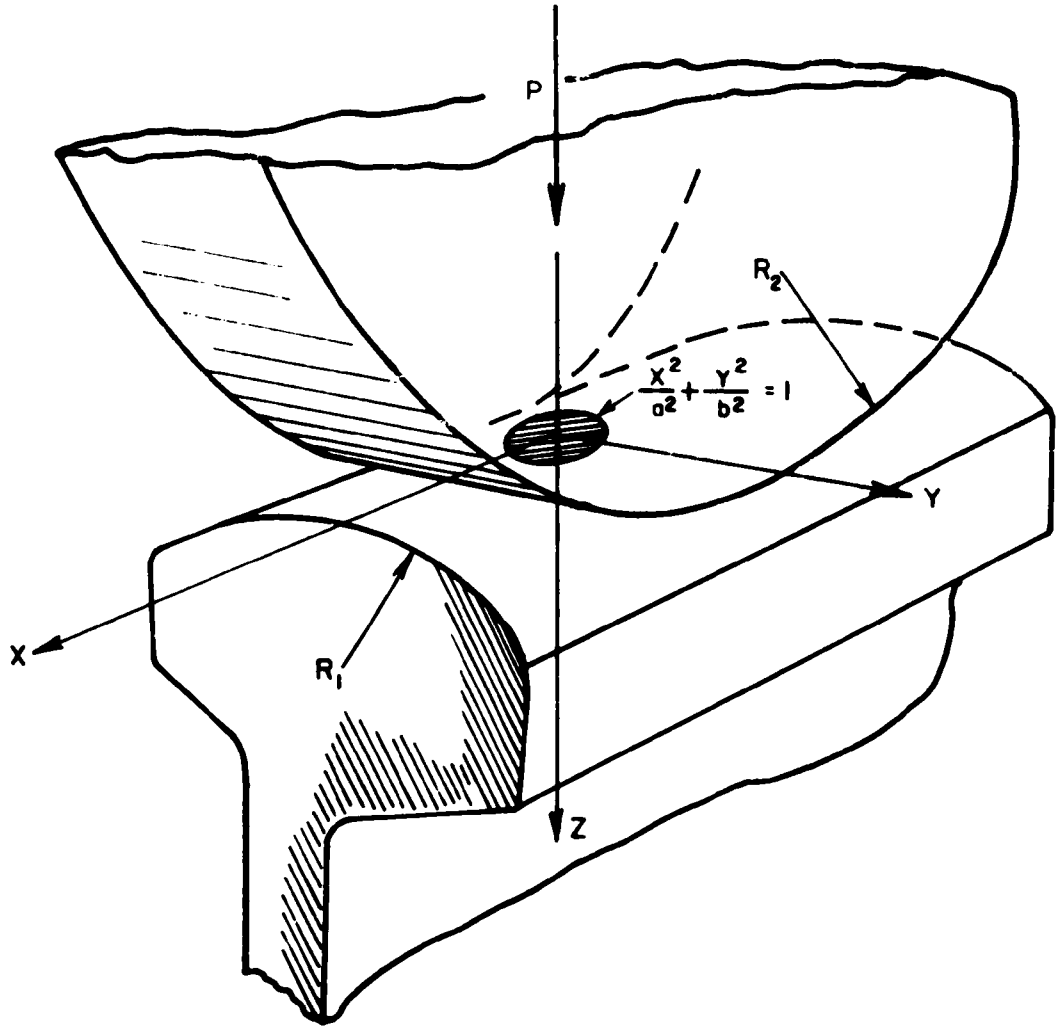


FIGURE 38. WHEEL/RAIL CONTACT AS ELLIPTICAL IN CONTACT

The pressure distribution across this area is ellipsoidal and of the form

$$\sigma_z = c_{\max} \left(1 - \frac{x^2}{a^2} - \frac{y^2}{b^2} \right)^{1/2} \quad (45)$$

where

$$\sigma_{\max} = -C_{\sigma}(b/\Delta) \quad (46)$$

is the maximum compressive stress in the contact region and

$$b = C_b^3 \sqrt{P\Delta} \quad (47)$$

$$a = b/k \quad (48)$$

$$\Delta = \frac{1}{A+E} \left(\frac{1-\nu_1^2}{E_1} + \frac{1-\nu_2^2}{E_2} \right) \quad (49)$$

E_1, ν_1 = the elastic modulus and Poisson's ratio, respectively, of the rail ($i = 1$) and the wheel ($i = 2$).

The constant C_{σ} , k and C_b (as well as C_{z_s} , C_{τ} , and C_G used below) can be found from Figure 39 for the appropriate A and B.

Figure 40 shows curves for various stress components directly beneath the centerline of contact of a 132-lb RE rail and a 28-inch diameter wheel under a 19,000-lb wheel load ($B/A = 1.16$). The curves show that the magnitudes of σ_x and σ_y decrease more rapidly than that of σ_z at points just beneath the surface of contact. Because of this fact, the maximum shearing stress, τ_{\max} , reaches its maximum value $(\sigma_z - \sigma_y)/2$ at a depth z_s . In general, the maximum shearing stress and depth of occurrence are given by

$$\tau_{\max} = C_{\tau}(b/\Delta) \quad (50)$$

and

$$z_x = C_{z_s} b \quad (51)$$

The von Mises yield criterion has been shown to adequately predict onset of yielding of steel. The parameter used in this criterion is the second invariant of the stress tensor or the octahedral shearing stress. The octahedral shearing stress τ_G defined beneath the centerline of contact is given by

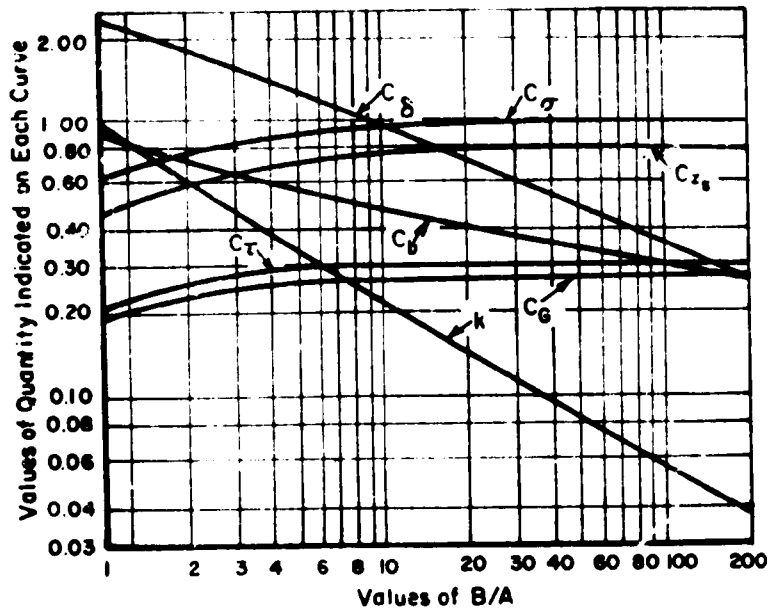
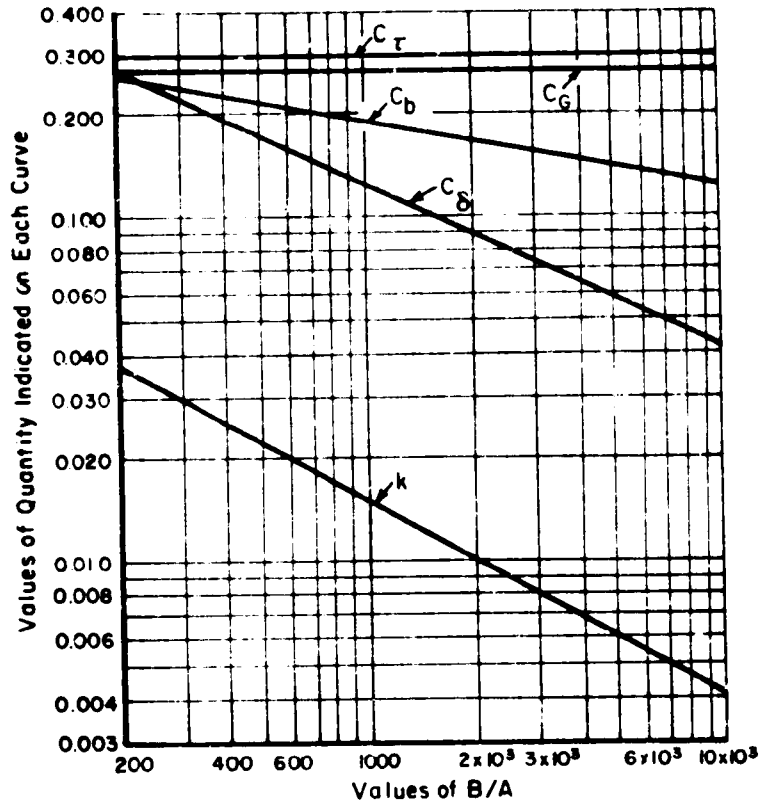


FIGURE 39. STRESSES AND DEFLECTIONS BETWEEN A WHEEL AND RAIL IN CONTACT [54]

$$\tau_G = \frac{1}{3} \left[(\sigma_x - \sigma_y)^2 + (\sigma_y - \sigma_z)^2 + (\sigma_z - \sigma_x)^2 \right]^{1/2} \quad (52)$$

and has a maximum value of

$$\tau_G = C_G (b/\Delta) \quad (53)$$

In Figure 40, it is seen that the maximum value of $\tau_G \approx 55,000$ psi, is at the onset of yielding for work hardened rail steel.

The accuracy of the Hertzian approach has been verified by several experimental investigations. An embedded strain gage technique was utilized by Bazergui and Meyer^[55] for measuring subsurface strain distributions in rolling contact. Ten strain gages assembled into four rosettes were embedded near the surface of a 10.6-inch diameter epoxy resin sphere. Two of the rosettes were arranged to measure strain in the x, y, and z directions. Elastic coefficients were determined by means of a two-dimensional rosette embedded in a cylindrical compression specimen.

Loading of the model sphere was accomplished by rolling it against an identical epoxy sphere. The loading fixture was arranged so that varying tangential tractions and normal pressures could be applied to the model.

Static calibration tests were conducted to compare experimental and theoretical results. The radius of the contact area was measured with a microscope. Figure 41 presents a comparison of these values of strain as a function of nondimensional distance from the point of contact. Excellent agreement is displayed in this figure with the Hertzian results. Good agreement with theoretically calculated stresses have also been reported by Fessler and Ollerton^[53]. In later work, Ollerton^[56] also demonstrated that the Hertz theory gives an accurate estimate of size and shape and orientation of the contact area, even when the contact areas are quite large. Andrews^[57] has measured contact areas under laboratory conditions and between wheels and rails in practice and found that the measured areas are always larger than predicted. This, however, may be due to the use of thin sheets of carbon paper and ordinary paper placed between the rail and wheel as well as the roughness of the surfaces in his experiments.

Timoshenko and Langer^[17], Eisenmann^[18], Talbot^[31], Code^[58], Paul^[59], and the ORE C53/RF 7 and 9 studies all have applied the theory of Hertzian contact to rail studies. Storey^[60] and Srinivasan^[61] utilizing these analysis methods evaluated the effects of various parameters on the wheel-rail contact

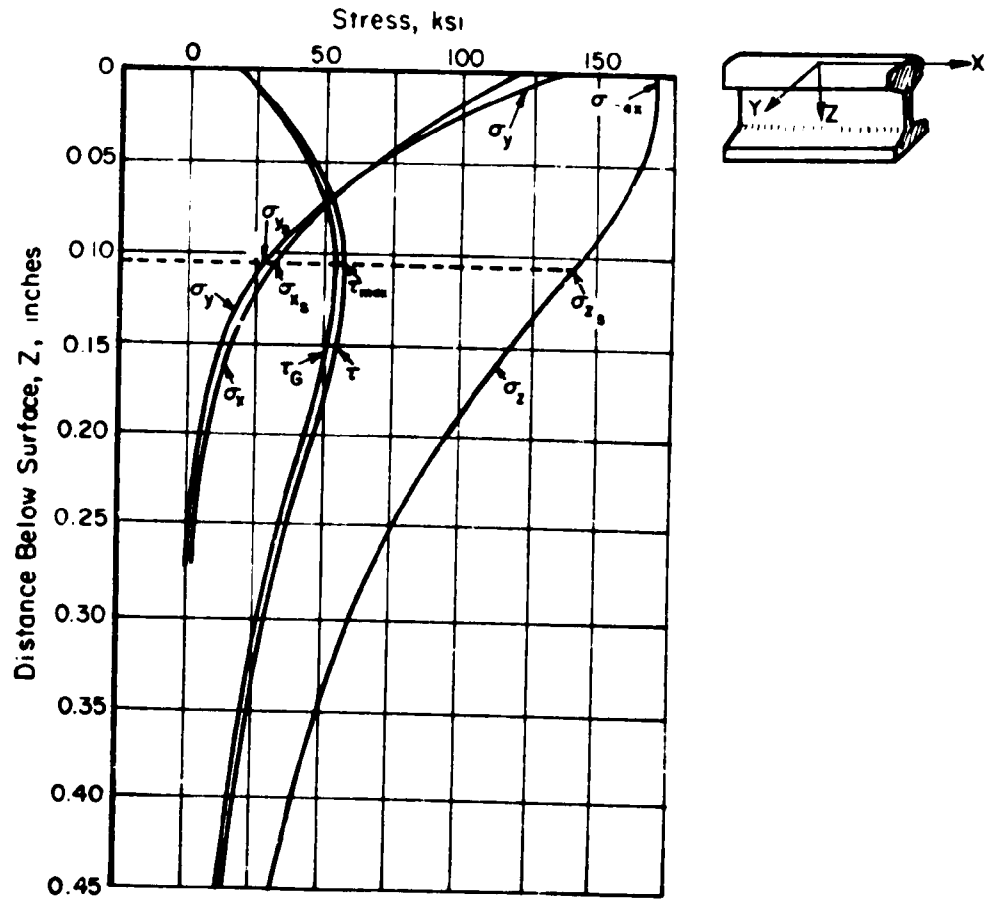


FIGURE 40. ELASTIC STRESS DISTRIBUTION IN RAIL HEAD UNDER THE WHEEL ($x=y=0$)

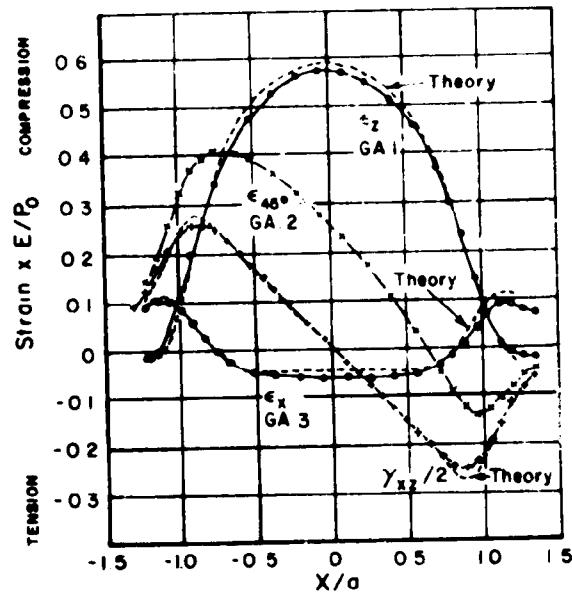


FIGURE 41. TYPICAL MEASURED AND THEORETICAL STATIC-STRAIN DISTRIBUTION BELOW THE SURFACE OF CONTACT ALONG THE LINE $y = 0$ AND $z/a = 0.236$

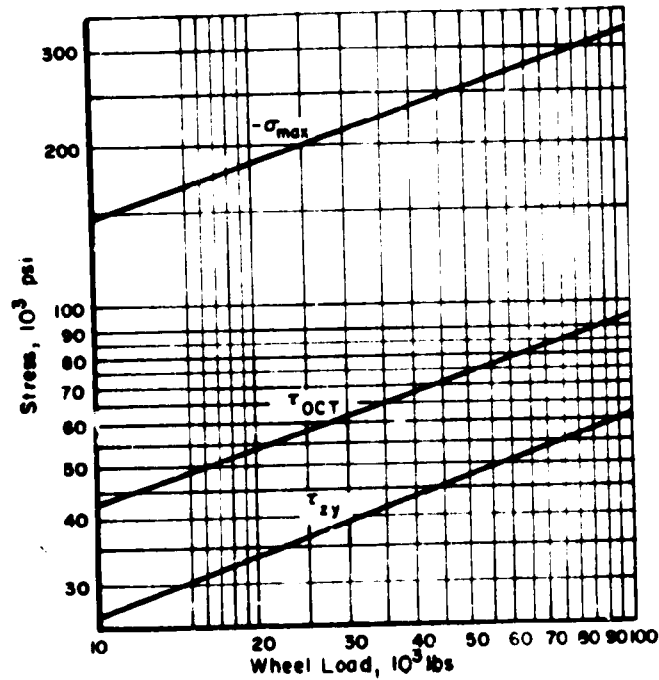


FIGURE 42. MAXIMUM COMPRESSIVE, OCTAHEDRAL SHEAR, AND ALTERNATING TRANSVERSE SHEAR STRESS FOR NEW 33-INCH DIAMETER WHEEL AND RAIL HAVING 10-INCH CROWN RADIUS

area and maximum shear stress below the surface of the rail. In this work, although seemingly obvious, it was found that rail curvature (due to bending) had little effect upon the area of contact. In Figure 42 is shown τ_{\max} within a rail having 14-inch crown radius for various wheel loads and wheel diameters as computed by Battelle.

In 1953, Radzimovsky^[8] analytically demonstrated for elastic cylinders in contact that subsurface transverse shearing stresses τ_{xz} are fully reversed during the rolling cycle as was seen in Figure 37. He pointed out that calculations based only on maximum normal stresses or on the maximum shearing stress cannot be considered as satisfactory in predicting fatigue failure because of the complicated stress conditions which are present in the case of the rolling bodies. The expression for onset of fatigue failure based on the Huber-Mises hypothesis put forth by Radzimovsky for two-dimensional stress fields is

$$\left[\left(\frac{\sigma_{xv}}{\sigma_{-1}} + \frac{\sigma_{xm}}{\sigma_s} \right) + \left(\frac{\sigma_{zv}}{\sigma_{-1}} + \frac{\sigma_{zm}}{\sigma_s} \right) \right]^2 - \left(\frac{\sigma_s}{\tau_s} \right)^2 \left[\left(\frac{\sigma_{xv}}{\sigma_{-1}} + \frac{\sigma_{xm}}{\sigma_s} \right) \left(\frac{\sigma_{zv}}{\sigma_{-1}} + \frac{\sigma_{zm}}{\sigma_s} \right) \right] + \left[\frac{\tau_r}{\tau_{-1}} + \frac{\tau_m}{\tau_s} \right]^2 = 1 \quad (54)$$

where

σ_{xv} , σ_{zv} and τ_v are the amplitudes of the alternating parts of the stress components σ_x , σ_z , and σ_{xz} , respectively

and σ_{xm} , σ_{zm} and τ_m are the steady parts.

Further, σ_s and τ_s are the yield stresses in tension and simple shear respectively and σ_{-1} and τ_{-1} the endurance limits due to a symmetrical stress cycle. Using this condition, he showed that subsurface shears were of sufficient magnitude to initiate fatigue failures. He went on to show that there was good correlation between data obtained by his calculations and the experimental results of both Buckingham^[62] and Way^[46]. The work of Radzimovsky pointed out the need to investigate the entire three-dimensional stress field. Up until that time, investigators had only concerned themselves with stresses along the centerline of contact in predicting fatigue initiation, as in Figure 50.

Martin and Hay^[9] in 1969 were the first to develop a model of a rail head that would permit general three-dimensional modeling. This model, based on finite elements, to date represents the most advanced analysis that has been

performed on railheads. The Martin and Hay model consisted of an elastic-plastic, three-dimensional model of a 132-lb RE rail, Figure 43, which was assumed to rest upon a rigid plane. Therefore, only contact stresses were considered and beam flexure was ignored.

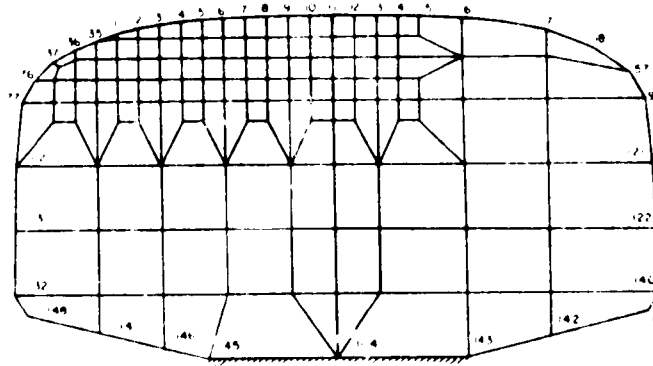
The contact pressure distribution was assumed always to be Hertzian and obtainable from Equation (45). Surface tractions were then assumed to be simply the contact pressure multiplied by the coefficient of friction.

The method of analysis used in this finite element procedure is not the customary one of applying nodal forces to the mesh and determining the equilibrium stress-states. In order to avoid having to develop a fine mesh, Martin and Hay determined the stresses that would be predicted on the boundary of finite element model using stress computed from a classical half space solution. The negatives of these stress and boundary conditions were applied to the finite element model and the stresses computed. The stress states from the finite element model were superimposed with those of the half space solution to yield the final stress state.

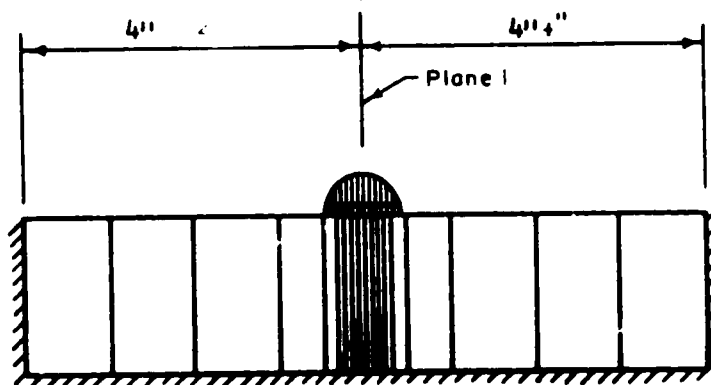
The authors utilized this procedure to investigate 27 cases of various loading combinations (vertical, lateral, longitudinal). The elastic-plastic results were presented without experimental validation. However, the elastic stresses developed do appear to agree reasonably well to the Hertzian results for the central load case. This can be seen in Figure 44, in which the results of Martin and Hay for the central load of 19,000 lbs are compared with the Hertzian results from Figure 40 for the same wheel, rail, and wheel load. Figure 45 gives the complete stress field within the rail at a vertical plane through the center of the contact area (Plane 1, Figure 43).

A number of experimental photoelastic investigations have been performed on model rail sections to determine the stresses induced by the wheel contact stress.

Three-dimensional, stress-freezing, photoelastic techniques were first applied to the investigation of rail head stresses by Frocht^[63] and later by Frocht and Wang^[64]. The model used consisted of a Fosterite, two-thirds scale replica of a 132-lb RE rail with a truncated rail web. The rail was loaded with a wheel contour corresponding to a 33-inch worn wheel. Two rails were loaded simultaneously in the stress freezing oven, Figure 46, at a 40.1 cant.



(a) Transverse Section



(b) Longitudinal Section

Figure 43. THREE-DIMENSIONAL MODEL OF RAIL HEAD AFTER MARTIN AND HAY [9]

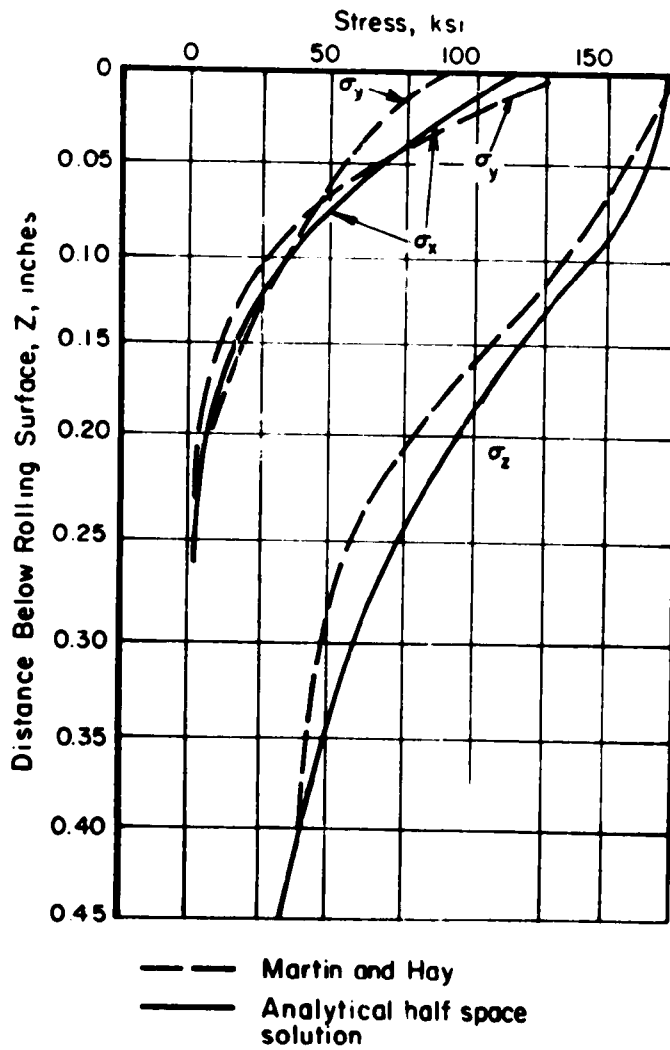
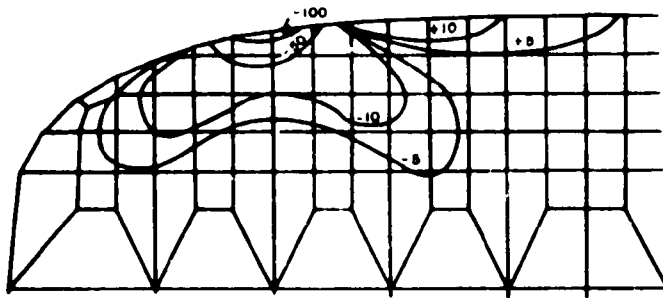
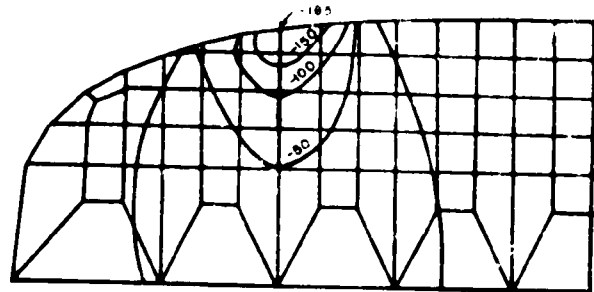
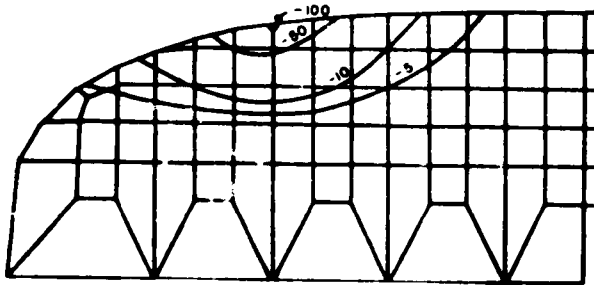
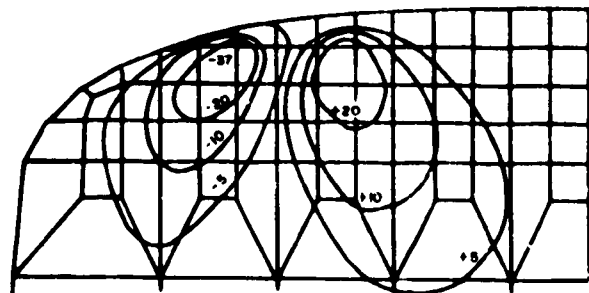
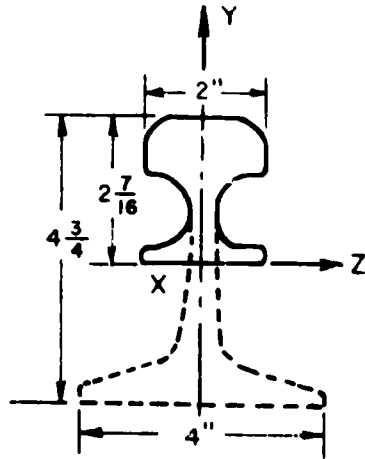
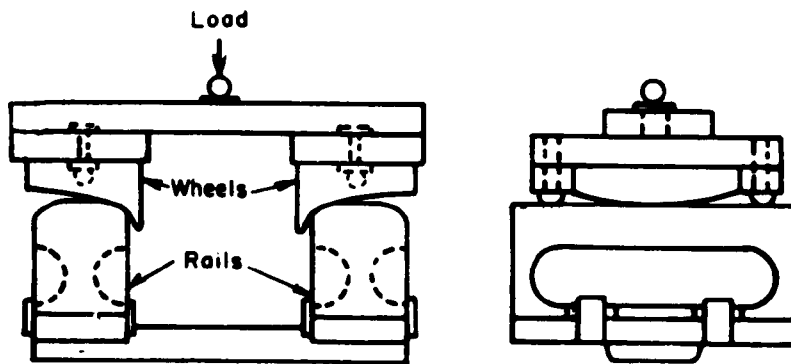


FIGURE 44. ELASTIC STRESS DISTRIBUTION FROM MARTIN AND HAY^[9] AND ANALYTICAL SOLUTIONS

Lateral Stress σ_y (ksi)Vertical Stress σ_z (ksi)Longitudinal Stress σ_x (ksi)Shearing Stress τ_{yz} (ksi)FIGURE 45. STRESS CONTOURS FOR 132-LB REPAIR AND 19000-LB WHEEL LOAD^[9]



a. Rail Section (132 lb RE rail)



b. Loading Arrangement (40:1 cant)

FIGURE 46. FROCHT PHOTOELASTIC MODEL AND TEST SETUP OF 132-LB RE RAIL AND 33-INCH DIAMETER WORN WHEEL

In the work of Frocht, both vertical (scaled 19,575 lb) and combined lateral-vertical (scaled 7,040 lb - 19,513 lb, respectively) loading cases were considered; however, Frocht and Wang considered only the vertical load cases (30,000 lb).

Figure 47 was derived from data given in Frocht and Wang and is presented in the format of rail stresses as a function of depth below the surface. Comparison of these curves, which are obtained for a 30,000 lb equivalent load, with those of Figure 40 for a 19,000-lb load show large differences. All the photoelastically measured stresses were much lower than would be expected for a 30,000-lb wheel load. As can be seen, these results are 20 percent lower than the analytical results for a 19,000-lb wheel load. It is not known how much of the difference can be attributed to the worn contour wheel. The difference may also be explained by the nature of the similitude relations applied by Frocht and Wang. These are approximate because of the nonlinear relation between applied load and contact stress distribution. Thus the similitude relations can be valid only near the point of load application.

Photoelastic determination of the contact stresses in rail were also performed by the ORE in report C53/RP5. A composite 1/3 scale model of a U36 Rail was used and is shown in Figure 48. This model was loaded with a simulated wheel section of radii $R_1 = 2.62$ inch. (7.9 inch rail full scale crown radius) and $R_2 = 6.6$ inch (19.7-inch wheel full scale radius). Figure 49 shows the maximum shear stresses as a function of depth for the model described. These values were obtained with a model load (35.8 lb) equivalent to a wheel load of 22,400 lb. Stresses were scaled by the relation $\frac{\sigma_m}{\sigma_p} = \frac{1}{70}$. Comparison with the calculated results obtained in Figure 40 for approximately the same loading and geometry shows good agreement, contrary to the results of Frocht.

All of the forementioned analytical descriptions of the contact between wheels and rails were based on the Hertzian contact theory since that was all that was available at the time. Perhaps the most significant, and certainly the most recent, contribution to topics of contact problems has been made by Conry and Seireg^[65] and again by Johns and Leissa^[66]. Realizing the intractable nature of problems involving bodies with more complex geometries than the ellipsoids of Hertz, Conry formulated a programming procedure utilizing a simplex-type algorithm to solve the contact of arbitrarily shaped homogeneous bodies.

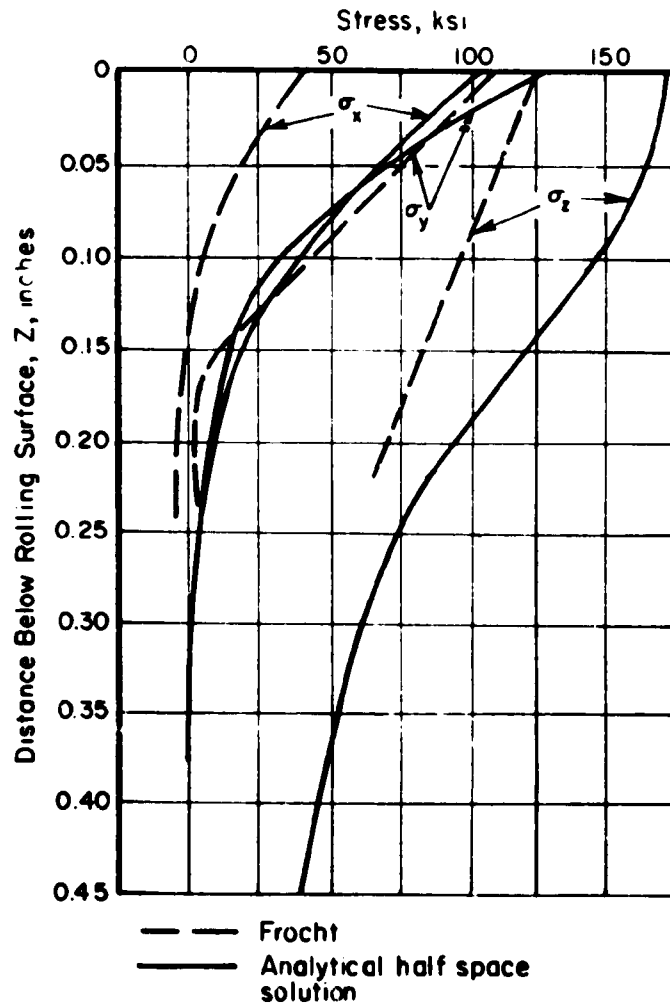


FIGURE 47. ELASTIC STRESS DISTRIBUTION FROM FROCHT AND ANALYTICAL HALF SPACE SOLUTIONS (30,000 LB WHEEL LOAD, 132-LB RAIL, 33-IN. WORN WHEEL) [63]

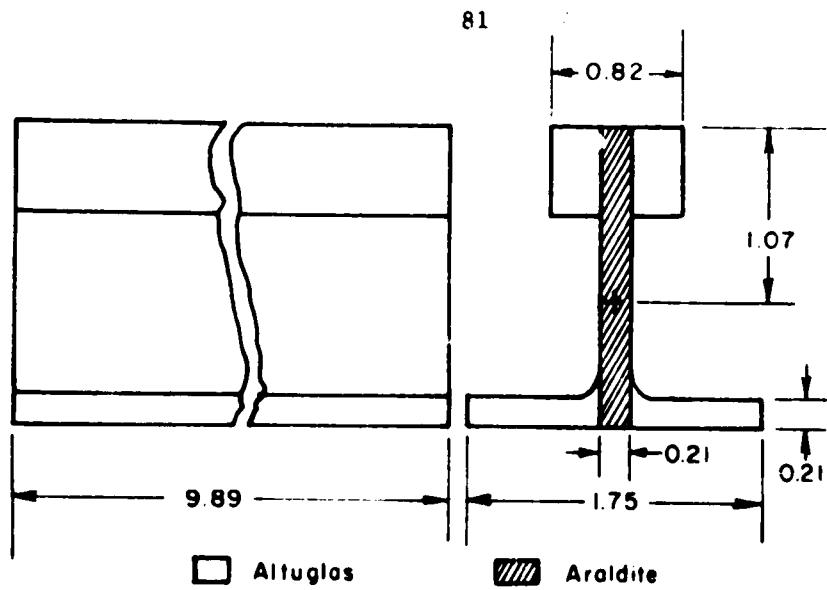


FIGURE 48. ORE PHOTOELASTIC MODEL OF U36 RAIL.

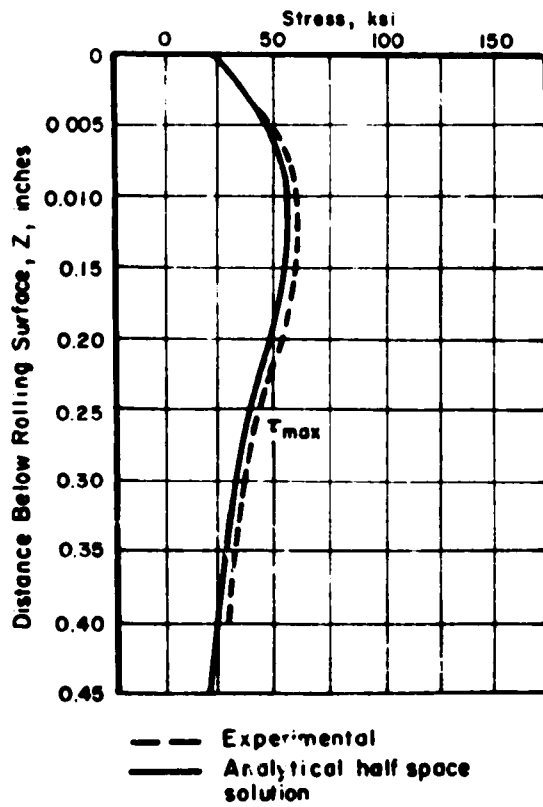


FIGURE 49. ELASTIC STRESS DISTRIBUTION FROM ORE PHOTOELASTIC MODELS

Using the simplex algorithm technique, Johns^[67] points out that subsurface failures are predicted to occur very near the surface if contact occurs near the corner radius of the wheel (Figure 50). The same action would be developed by contacting the gage corner of a rail. Due to this action, the contact stress distribution deviates greatly from Hertzian and develops a high-peak compressive stress toward the edge of the contact region. Those high normal contact stresses cause a region of high shearing stress to be developed just beneath the contact surface near the corner radius. This phenomenon has not been investigated in wheel-rail interaction; however, several investigators have observed this effect in edge loading of cylindrical rollers. These include Singh and Paul^[68] and Kannel^[69]. These conditions are similar to the conditions encountered at the edge of the rail head as the wheel set translates laterally as occurs during track hunting behavior.

5.2 SURFACE TRACTIONS OR ELASTIC SHEARING FORCES

When a wheel rolls across a rail, although the wheel rolls without overall sliding, microslip may be taking place between the surfaces at some points within the contact region, while at other points the surfaces move together without slip. Thus, the contact area is divided into a region of slip and a "locked" region of no slip. The distribution of tangential stresses within the contact region was first formulated by Carter^[70], Figure 51, for a roller on a plane.

Carter found that the maximum surface shearing stress occurs on the edge of the locked-in region and is given by,

$$\tau_M = \frac{2\phi\sigma_M}{\pi n l} \left(1 - \frac{x^2}{a^2} \right)^{1/2} \quad (55)$$

where

$2a$ = the width of the contact region

l = the roller width

ϕ = the coefficient of friction

σ_M = the maximum compressive stress

The location of maximum shearing stress occurs at $x = c$ as shown in Figure 52.

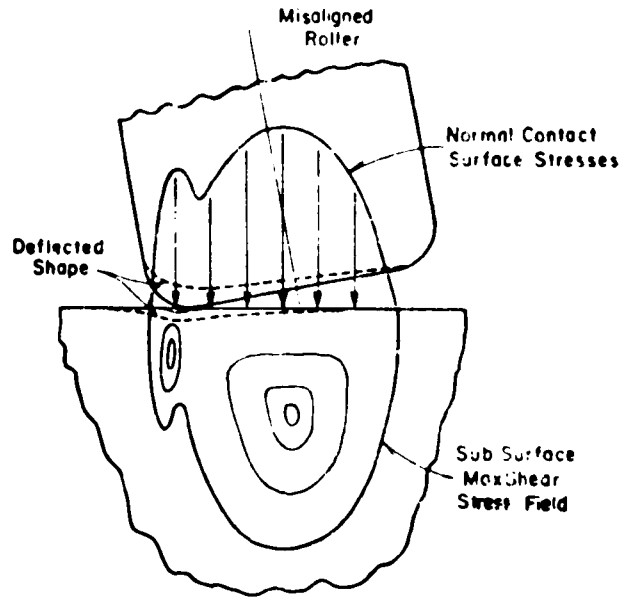


FIGURE 50. FORM OF SURFACE CONTACT STRESSES AND SUBSURFACE SHEAR FOR A MIS-ALIGNED ROLLER AND RAIL

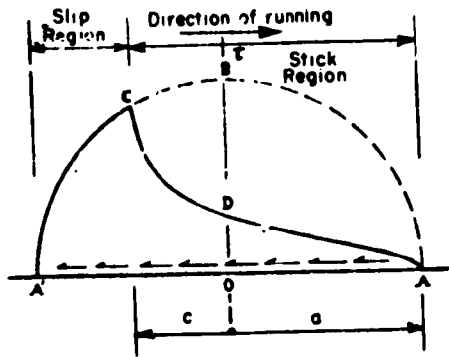


FIGURE 51. FORM OF THE SHEAR STRESS DISTRIBUTION FOUND BY CARTER FOR ROLLING CONTACT [70]

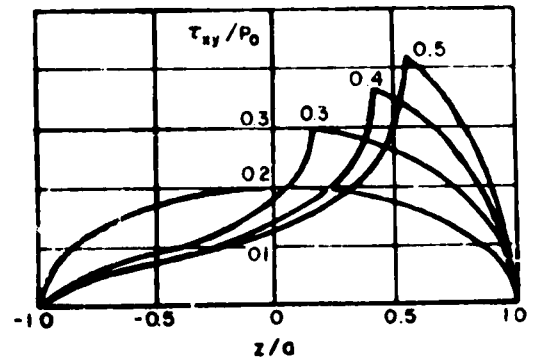


FIGURE 52. INFLUENCE OF THE COMPONENT OF FRICTION IN THE PARTIAL SLIP OF CYLINDERS [77]

where

$$c = a \left[1 - 2 \left(1 - \frac{T}{\mu P} \right)^{\frac{1}{2}} \right] \quad (56)$$

and

$$T = \text{driving (or braking) force.} \quad (57)$$

The formulation has since been studied and extended by Mindlin^[71], Poritsky^[72], and Johnson^[73, 74, 75], with the work of Poritsky being directly applied to wheel-rail studies. Johnson^[76, 77] demonstrates the effect of the coefficient of friction on the partial slip and distribution of surface shear stress where the tangential force is maintained at $T = 0.2P$, Figure 52.

A combined analytical and experimental photoelastic study was performed by Haines and Ollerton^[78]. Bazergui and Meyer^[55] have presented subsurface strain distributions for the same situations. Haines and Ollerton performed a photoelastic analysis using two 5.0 inch araldite casting resin B, spheres. The experimental technique used involved rolling the spheres together in a stress-freezing oven and stopping them in such a way that the tangential tractions established during rolling were preserved. Figure 53 shows the experimentally determined shearing stress versus calculated values as determined by Haines and Ollerton.

More rigorous mathematical investigations have been more recently performed by Kalker^[79] and Mow, et al^[80].

It has been demonstrated by Smith and Liu^[81], Hamilton and Goodman^[82], Lawn^[83], and again by Poritsky^[72] that the location of highest shearing stress in rolling contact due to full slip surface traction can occur on the surface at the rear of the contact region. This is seen from Figure 54 in which is plotted the octahedral shearing stress beneath cylindrical rollers. The critical value of coefficient of friction above which the greatest shear occurs on the surface is approximately $\mu = 0.27$. Although cylindrical contact assumptions and results are often used to describe wheel-rail contact stresses for new wheel and rail the true contact area may be more closely represented by a circle. This was seen in the example given in Figure 38 where $B/A = 1.16$. Therefore, the results are also presented for contacting spheres, Figure 55.

The form of the stress distributions closely resemble photoelastic results of Hamilton^[84] who investigated normal and tangentially loaded discs of glass against aluminum plates. Lawn went on to also obtain excellent agreement between his predictions and experiments. His experiment created surface

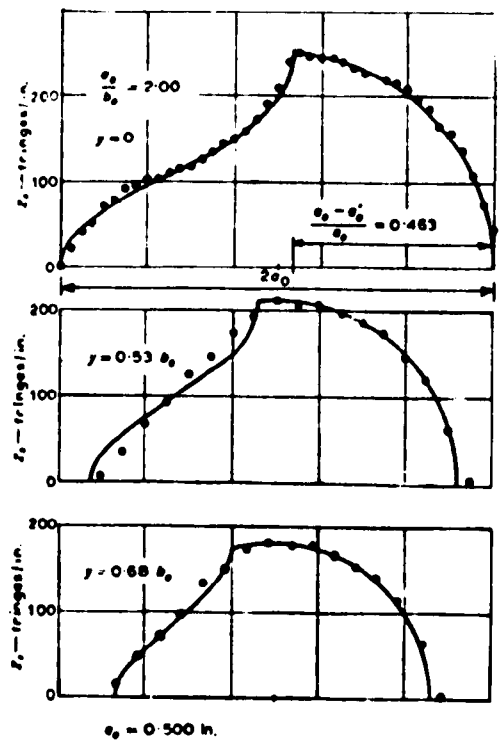
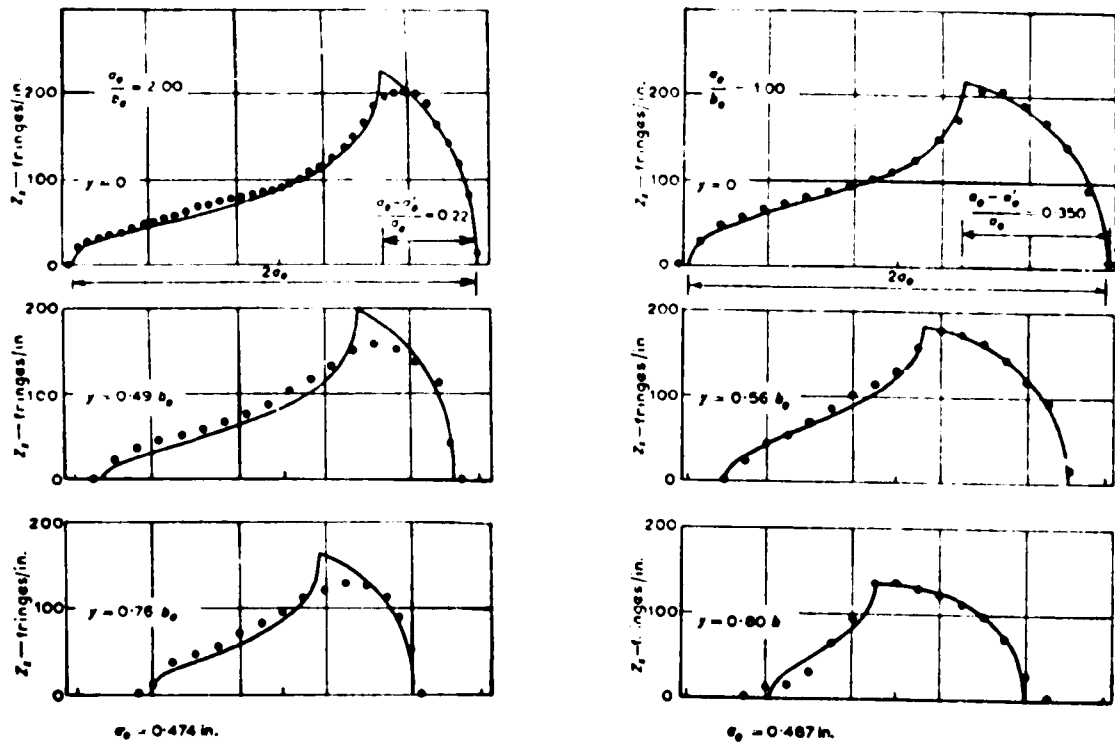


FIGURE 53. MEASURED AND THEORETICAL SURFACE TRACTION STRESSES

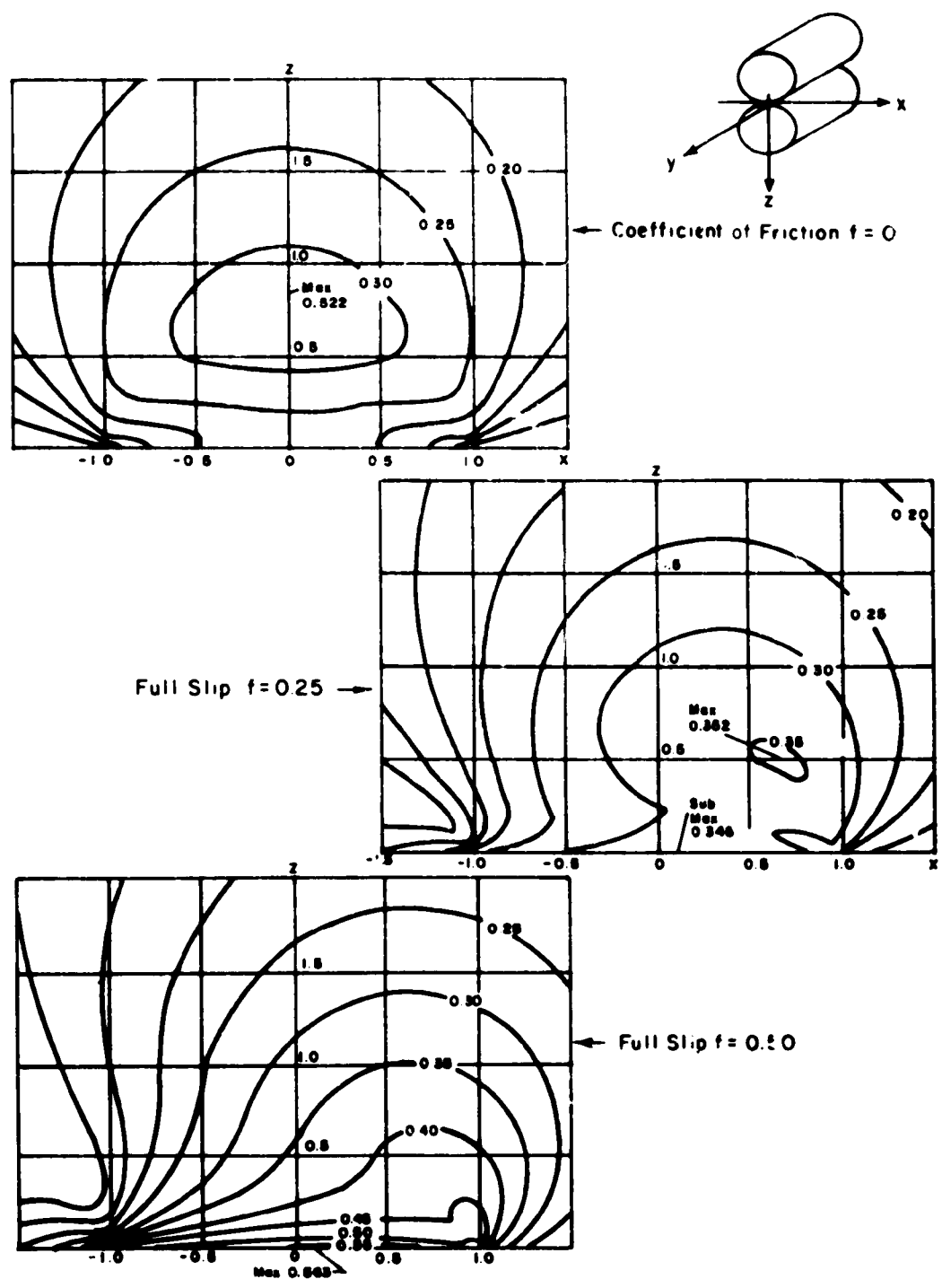


FIGURE 54. LINES OF CONSTANT OCTAHEDRAL SHEARING STRESS τ_G/σ_{max} BENEATH THE CONTACT AREA BETWEEN THE CYLINDERS [82]

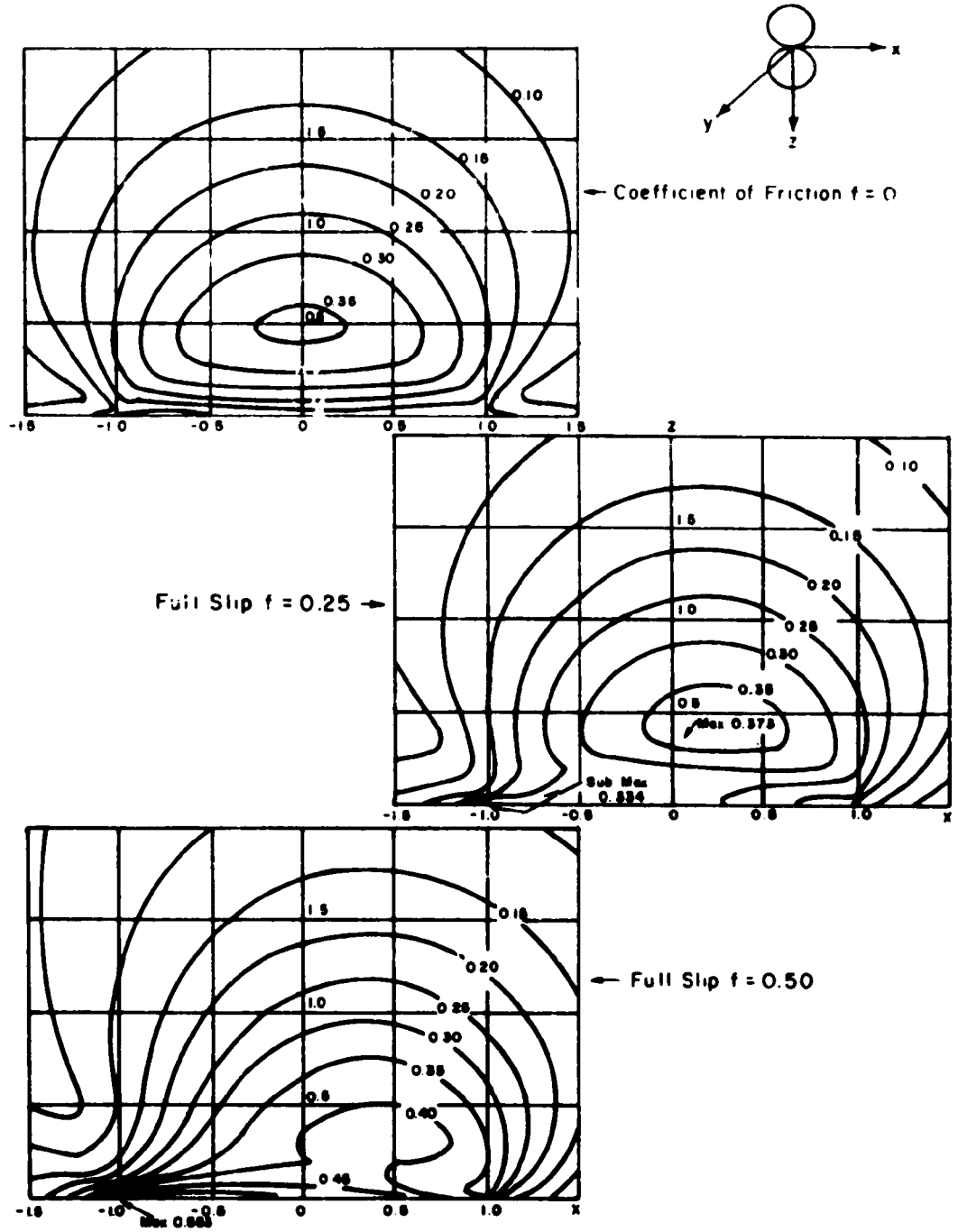


FIGURE 55. LINES OF CONSTANT OCTAHEDRAL SHEAR STRESS, τ_G / σ_{\max} BENEATH THE CONTACT AREA BETWEEN THE SPHERES [82]

cracks by sliding a steel ball across unlubricated glass. He postulated that the formation of surface cracks was due to the ultimate strength in shear being exceeded, therefore, demonstrating the existence of very high shearing stresses at the surface as a result of the surface traction.

In characterizing shelly failures in Japan, Nakamura, et al.^[85], describe surface cracks that were found to occur on both curved and tangent track. They suggested that the cracks are formed by slip between the wheel and rail. The fatigue crack pattern was found to closely resemble those formed in the laboratory by Lawn under controlled conditions of sliding. Nakamura, et al., also reproduced these cracks under a somewhat controlled experiment that involved sliding. They further concluded from their investigation that the existence of ferrite in the surface layer of the rail seems to encourage this mode of failure. Further, wearing off any plastically deformed surface layer was found to retard the growth of cracks. Several mechanisms are a possible cause of this phenomenon.

Smith and Liu^[81] presents a compact formulation for computing the stresses with contacting rollers due to both normal Hertzian loads and tangential loads resulting from full slip conditions. The normal, longitudinal and transverse shearing stress respectively given for normal loading are

$$\begin{aligned}\sigma_{zn} &= -\frac{\sigma_{\max} z}{\pi} \left[a\bar{\Psi} - x\Psi \right] \\ \sigma_{xn} &= -\frac{\sigma_{\max} z}{\pi} \left[\frac{a^2 + 2x^2 + 2z^2}{a} \Psi - \frac{2\pi}{a} - 3x\Psi \right] \\ \tau_{xzn} &= -\frac{\sigma_{\max} z^2}{\pi} \Psi\end{aligned}\quad (58)$$

and for tangential loading

$$\begin{aligned}\sigma_{zt} &= \frac{\sigma_{\max}}{\pi} z^2 \Psi \\ \sigma_{xt} &= \frac{\sigma_{\max}}{\pi} \left[\left(2x^2 - 2a^2 - 3z^2 \right) \Psi + 2\pi \frac{x}{a} + 2 \left(a^2 - x^2 - z^2 \right) \frac{x}{a} \Psi \right] \\ \tau_{xzt} &= -\frac{\sigma_{\max}}{\pi} \left[\left(a^2 + 2x^2 + 2z^2 \right) \frac{z}{a} \bar{\Psi} - 2\pi \frac{z}{a} - 3xz\Psi \right]\end{aligned}\quad (59)$$

where

$$\bar{\Psi}, \Psi = \frac{\pi}{K_1} \left[\frac{K_2}{K_1} \right]^{\frac{1}{2}} \left\{ 2 \left[\frac{K_2}{K_1} \right]^{\frac{1}{2}} + \left[\frac{K_1 + K_2 - 4a^2}{K_1} \right]^{\frac{1}{2}} \right\}^{\frac{1}{2}} \left(1 \pm \left[\frac{K_2}{K_1} \right]^{\frac{1}{2}} \right)^{\frac{1}{2}}$$

where $\bar{\Psi}$ corresponds to the + sign, and Ψ the - sign.

$$K_1 = (a + x)^2 + z^2$$

$$K_2 = (a - x)^2 + z^2$$

(60)

6. RESIDUAL STRESSES IN RAILS

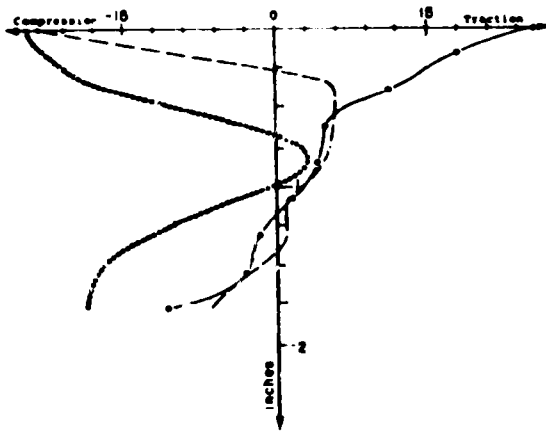
6.1 DEVELOPMENT OF RESIDUAL STRESSES IN RAIL HEADS

At wheel loads in excess of approximately 19,000 lbs new rails plastically deform upon passage of the first vehicle. At larger wheel loads residual stresses are known to build up in a region adjacent to the head surface that extends to nearly a quarter of the depth of the head. The residual stress build up results in a zone directly beneath the tread surface of compressive stresses and a deeper adjacent region of tensile stress. In Figure 56 are shown the distributions of residual stresses within the rail head as determined experimentally^[86]. Although the load history is not well known, the residual stress state is considerably different from the initial stress state.

Horizontal cracks and split heads are known to initiate in the zone of residual tensile stresses within the rail head^[87], Figure 57. Hardness profiles similar to those in Figure 57 of rail heads for a range of cycles, loads, and wheel diameters are given by Alleman^[88,89]. Almen^[90] also relates rail shelly failures to residual stresses in the rail head. He theorized that microcracks are formed by tensile stress fields present around metallurgical defects, such as inclusions or voids. These microcracks then grow along the junction between the elastic and plastic zones due to the residual stress field caused by the plastic deformation of the rail. Cracks occurring closer to the surface of the rail would arrest or turn due to the residual compressive fields.

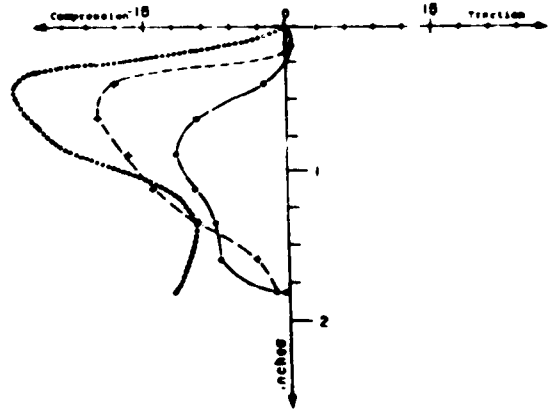
When plastic deformation occurs, the residual stresses that remain upon unloading make yield during subsequent loading cycles more difficult. If the loading remains below a limit load called the shakedown limit, after repeated load applications, the residual stresses will increase sufficiently that plastic deformation ceases to occur, and subsequent load cycles will be totally elastic. When this occurs, the stresses are said to have "shakedown" to within the elastic limit. For some cases it is theoretically possible to determine if shakedown can and will occur. Unfortunately, however, it is not possible to determine how many load cycles will be necessary for the plastic flow to cease.

Another interesting result of the forementioned experimental studies is buildup in residual stress over a large number of cycles. In this work, U36 rails were loaded by 32.5 inch diameter wheels. The wheel loads were such



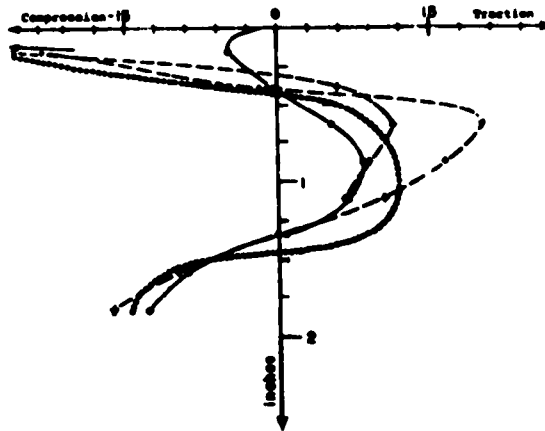
- • — New rail made of standard-grade steel (R = 70-75 hbar)
- + — Work-hardened rail made of standard-grade steel (R = 70-75 hbar)
- Work-hardened rail made of hard-grade steel (R = 87-92 hbar)

a. Longitudinal Stress (ksi)



- • — New rail made of standard-grade steel (R = 70-75 hbar)
- + — Work-hardened rail made of standard-grade steel (R = 70-75 hbar)
- Work-hardened rail made of hard-grade steel (R = 87-92 hbar)

b. Vertical Stress (ksi)



- • — New rail made of standard grade steel (R = 70-75 hbar)
- + — Work-hardened rail (two series of measurements) made of standard grade steel
- Work-hardened rail made of hard-grade steel (R = 87-92 hbar)

c. Transverse Stress (ksi)

FIGURE 56. LONGITUDINAL, VERTICAL, AND TRANSVERSE RESIDUAL STRESS IN NEW AND USED RAIL BENEATH THE CENTERLINE OF CONTACT

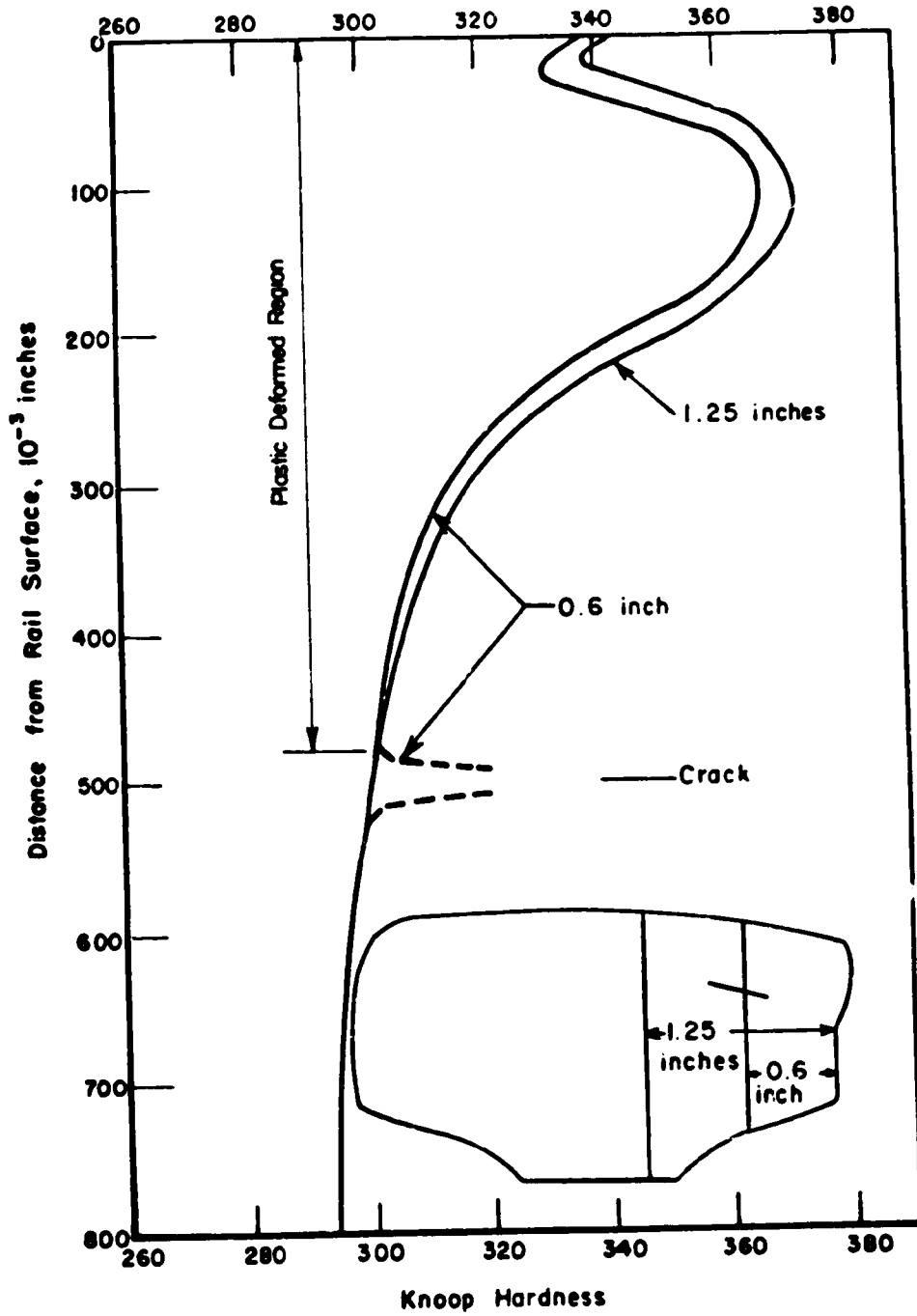


FIGURE 57. HARDNESS PROFILE OF NONHEAT-TREATED STANDARD RAIL SPECIMEN NO. 828 [87]

that the 21,000 lb wheel load should have been at approximately the shakedown limit; however, flow was observed until 10^5 cycles, as was also the case with lower load. Figure 58 summarizes the available data on buildup of residual stresses in rails. Therefore, it is quite possible that although shakedown is predicted to occur for rails, the plastic flow continues through a large number of wheel passes.

6.2 DETERMINATION OF STRESSES DUE TO PLASTIC DEFORMATION

For the passage of heavily loaded railroad cars, the stresses developed within the rails may exceed the elastic limit. In such cases, the material near the contact region deforms plastically. This increases the contact area needed to support the load.

The problem of determining the stresses resulting from plastic deformations during rolling has not been widely treated in the literature, although a few investigations have contributed to the understanding of development of these stresses in rails. The primary contributions are due to Johnson (University of Cambridge), Radenkovic (Ecole Polytechnique in Paris), Hardy and Tordion (Laval University of Quebec), and Martin (at AAR). One of the first attempts to identify the fundamental mechanisms associated with plastic flow was due to Johnson^[91]. In this study of cylindrical rollers, it was shown that residual stresses must be of the form such that they are a function only of depth, z ,

$$\sigma_x^r = f_1(z) \quad \sigma_y^r = f_2(z) \quad (61)$$

and due to symmetry conditions

$$\sigma_z^r = \tau_{xz}^r = \tau_{xy}^r = \tau_{zx}^r = 0 \quad (62)$$

If a shakedown limit is to exist after rolling contact, Melan's theorem^[92] requires that when a roller passes a point, the sum of the contact stresses and the residual stresses of Equation (61) must be elastic. When a roller and a plane make normal contact in the absence of residual stresses, the stresses will be completely elastic according to the von Mises criterion

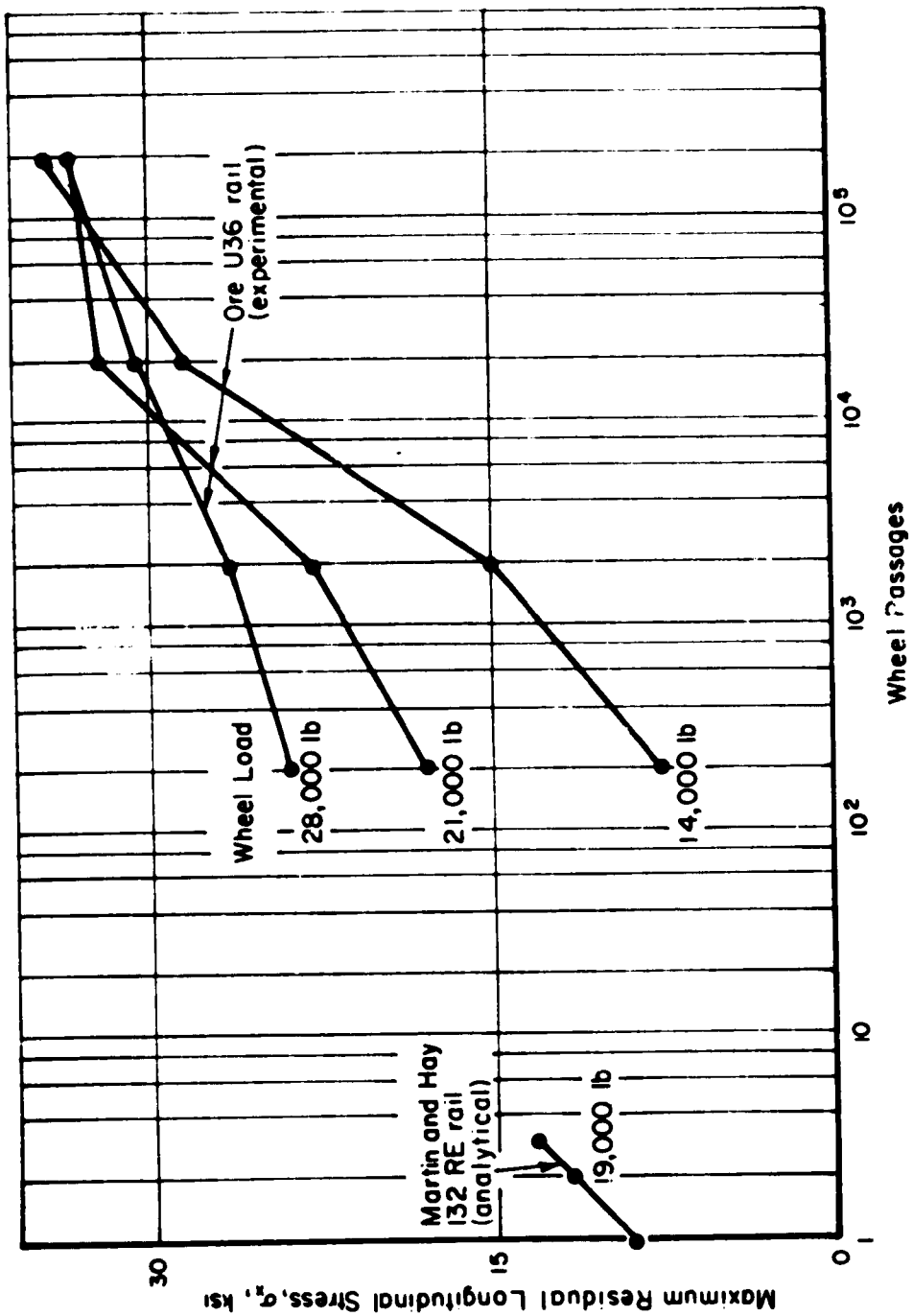


FIGURE 58. RESIDUAL LONGITUDINAL STRESS FOR ANALYTICAL AND EXPERIMENTAL RAIL MODELS

of yielding as long as the maximum compressive stress is

$$\sigma_{\max} \leq 3.10k \quad (63)$$

and according to the Tresca criterion

$$\sigma_{\max} \leq 3.3k \quad (64)$$

where k is the yield stress of the material in simple shear. It is generally accepted^[92] for steels^[93] that the von Mises yield criterion presents the most valid method of determining the onset of yielding. It is well known that for rollers this elastic limit stress is first reached at a point beneath the surface on the axis of symmetry at a depth $z = 0.78a$. For contact of an elastic sphere with a plane, the maximum compressive stress according to the von Mises criterion is

$$\sigma_{\max} \leq 3.0k \quad (65)$$

According to the above requirement for shakedown according to the Tresca yield condition

$$\frac{1}{4} \left(\sigma_x^e + \sigma_x^r - \sigma_z^e \right)^2 + \tau_{xz}^e \leq k^2 \quad (66)$$

in which σ_x^e , τ_{xz}^e are the elastic components of stress. Here σ_x^r can be chosen to have any value. It is immediately apparent that no value of σ_x^r will satisfy (66) if τ_{xz}^e at any point in the rail exceeds k . The result is that the stress component that determines if shakedown will occur is the transverse shear τ_{xz} and that for a cylinder on a plane shakedown is theoretically predicted if

$$\sigma_{\max} \leq 4.0k \quad (67)$$

and for a sphere on a plane if

$$\sigma_{\max} \leq 4.8k \quad (68)$$

It can be shown that this relationship is independent of the choice of yield criterion. The maximum rolling load P for shakedown to occur is 1.66 times that required to initiate plastic flow, i.e.,

$$\frac{P_{\text{shakedown}}}{P_{\text{elastic}}} = 1.66 \quad (69)$$

for a roller on a plane.

According to the Tresca criterion, plastic flow is restricted to shear in the x - z plane so that σ_y^r takes the value $\nu\sigma_x^r$. The von Mises criterion, on the other hand, predicts axial flow and so builds up a high value σ_y^r . Johnson goes on to show the form the stress field assumes at the shakedown level, Figure 59.

In order to determine cumulative plastic deformation under the action of loads greater than shakedown, Merwin and Johnson^[10] introduced the assumption that each strain cycle remains identical with the elastic strain cycle. The strain at each location is assumed to be incrementally advanced through the strain cycle in this way. If yielding occurs at any point in the cycle, the Prandtl-Reuss equations are applied to determine the stress at the next increment in the strain cycle. This procedure is continued through the cycle. In this way, these strains constitute a compatible system, where the boundary conditions are satisfied. The solution is inexact to the extent to which the stresses do not satisfy the equilibrium equations. Merwin and Johnson do, however make some attempt to restore equilibrium at the end of each cycle. Typical elastic-plastic stress cycles obtained for an elastic-perfectly plastic material from the numerical analysis are shown in Figure 60. It was found in all cases examined that above the shakedown limit a steady state condition was quickly reached in which additional shearing strain of the surface in the forward direction was incurred upon each cycle. Figure 61 shows the variation of the residual stress with different load levels. The effect of surface tractions were added to the methods of Merwin and Johnson by Johnson and Jefferis^[77]. In the presence of increasing surface tractions under full slip, the shakedown limit load gradually decreases, Table 6 and its location slowly decreases in depth. When the tangential force T exceeds $0.367P$ a second region on the surface exceeds the subsurface maximum so that shakedown is then controlled by surface stresses. Figure 62 shows how the subsurface

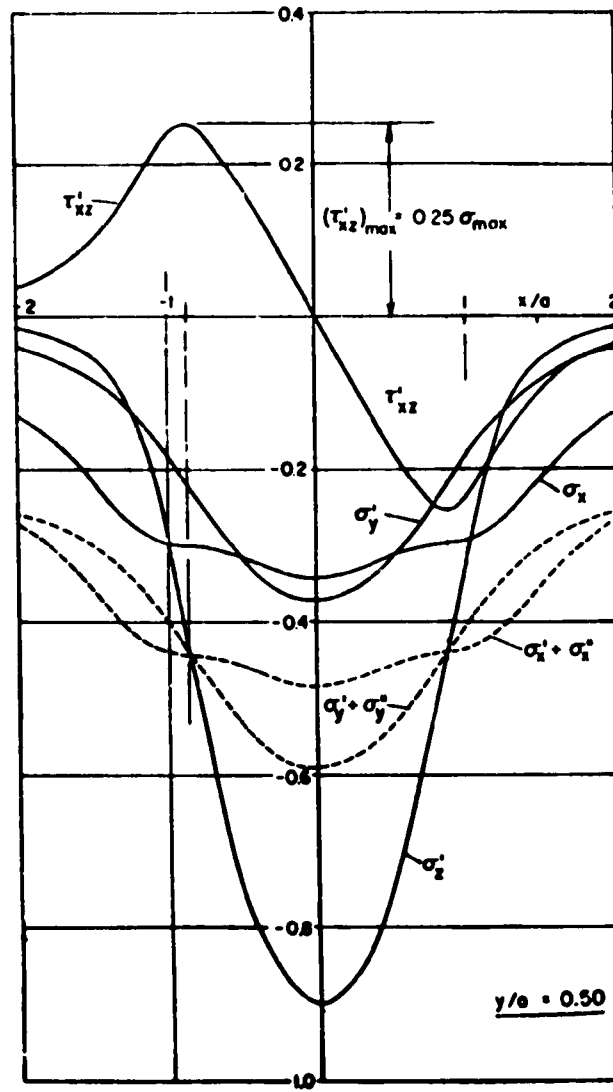


FIGURE 59. STRESS FIELD AT SHAKEDOWN LIMIT IN CYLINDER CONTACTING A PLANE [79]

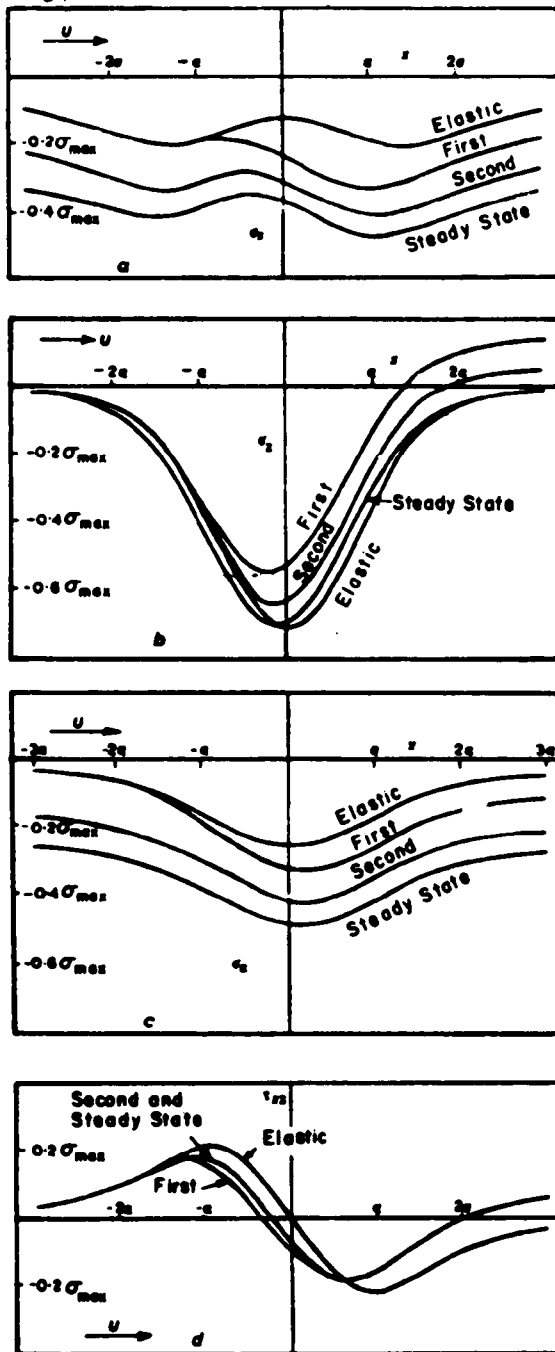


FIGURE 60. VARIATIONS OF THE STRESS COMPONENTS (a) σ_{x1} , (b) σ_y , (c) σ_z , AND (d) τ_{xy} WITH x AT A CONSTANT DEPTH, $y = -a$, AND LOAD $p_0 = 5.5k$

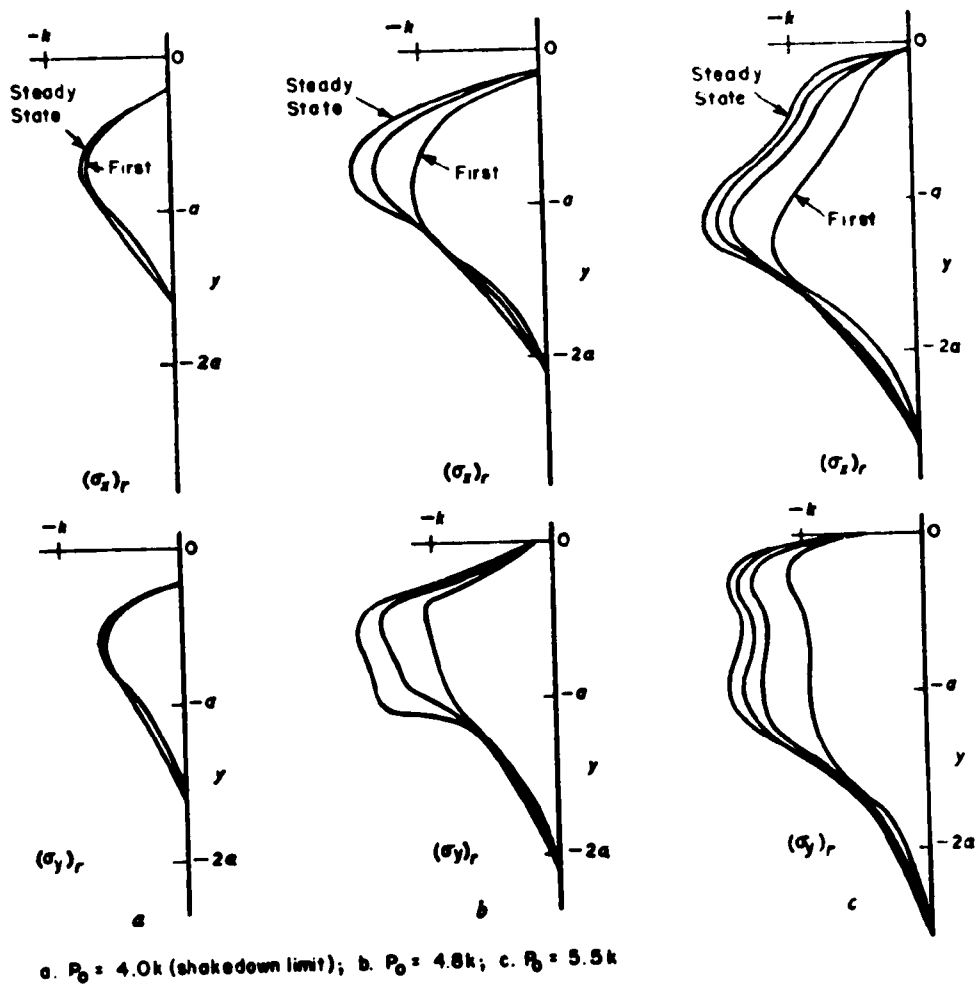


FIGURE 61. BUILDUP OF RESIDUAL STRESS $(\sigma_x)_r$ AND $(\sigma_y)_r$ WITH REPEATED PASSAGE OF THE LOAD

TABLE 6. THEORETICAL SHAKEDOWN LOAD FOR
VARIOUS SURFACE TRACTIONS T

T/P	Shakedown Load, K
0.000	4.00
0.100	3.56
0.200	3.21
0.300	2.90
0.367	2.75

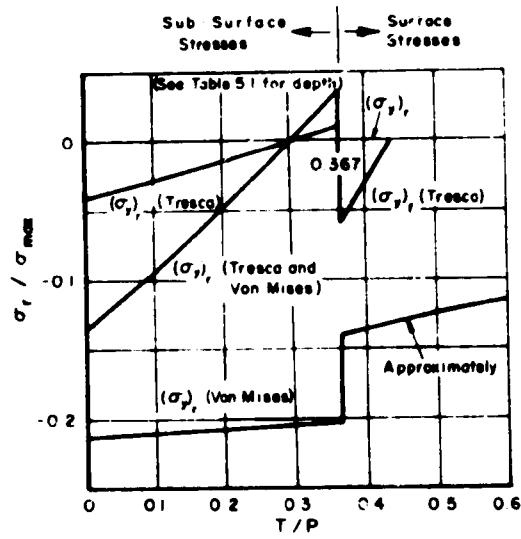


FIGURE 62. CRITICAL RESIDUAL STRESSES NECESSARY TO PRODUCE SHAKEDOWN [83]

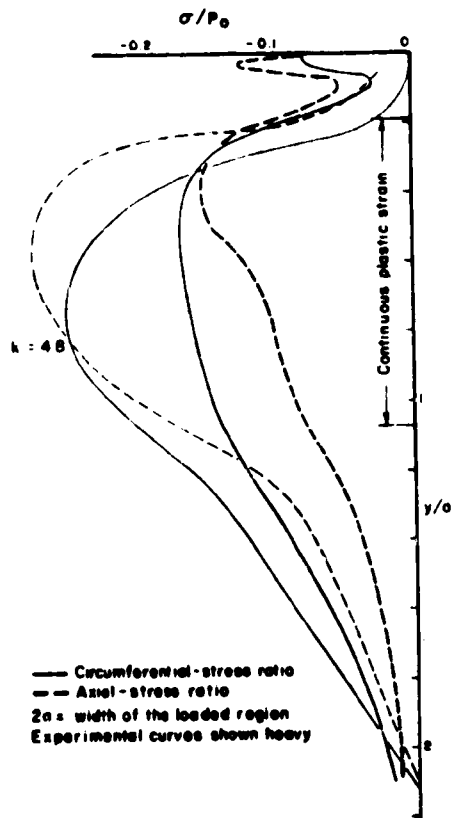


FIGURE 63. STRESS RATIO PLOTTED AGAINST DEPTH COMPARISON OF EXPERIMENTAL RESULTS WITH THEORETICAL PREDICTIONS [84]

stress changes with the ratio of T/P at the shakedown limit using both Tresca and von Mises yield criteria. There is substantial difference in computed σ_y^r depending upon the yield criteria used. This stress is likely to be one of the most important stresses in propagation of some fatigue flaws.

An experimental analysis was performed to verify the results of Johnson and Jefferis by Pomeroy and Johnson^[94]. In their work, residual stresses were determined in aluminum and steel rollers. In that Johnson assumed no work hardening, the aluminum tests provide the best comparisons to theory. Using a measurement technique similar to Sach's technique good correlation was found between experimental data and the analytical results of Johnson and Jefferis, Figure 63.

Results were also obtained after 10 and 100 rolling contact cycles for steel rollers with $\sigma_{max} = 4.8k$. Measurements were made again at 100,000 cycles. No appreciable differences were found, indicating that the residual stress state had shaken down.

The deficiencies of the Johnson approach making it unsuitable to be quantitatively applied to rails are

1. The model does not account for change in surface contour and, therefore, a change in contact stress.
2. The model is two-dimensional.
3. The material behavior is elastic, perfectly plastic.

In the two-dimensional problem of a roller on a plane, the surface after deformation can, with reasonable justification, be assumed flat. Therefore the shape of the contact area and the Hertz elastic contact stress are not affected by previous plastic flow. In the case of a heavily loaded wheel causing plastic deformation of a rail, this fails to be true. Upon yielding of the rail, the deformation will result in a slight flattening of the contact surface. It is shown in Figure 64 for deformed indentors that this type of deformation greatly reduces the normal contact stress. The shape of the distribution upon subsequent passages must also change, therefore, causing a change in the plastic strain field. It is likely, but yet unproven, that an analysis which recomputes the contact stress distribution after each pass will show that the actual flow per pass is greatly decreased.

Two-dimensional finite element models have been developed by both Hardy and Tordion^[95] and ORE. The ORE developed a two-dimensional model,

Figure 65, in which plastic deformations were specified. They assumed that the permanent deformation occurred only to a depth of 0.394-inch and over a total width of 0.788-inch of the rail head. It was further assumed that

$$\epsilon_z^P \sim -\epsilon_y^P \quad (70)$$

Similar assumptions were made upon the shearing strain γ_{yz}^P . The two-dimensional analytical stress results are shown for a U36 rail and 20,000-lb wheel load in Figure 66. Also shown in this figure are the results of "hole drilling" residual stress measurement technique. The comparisons are seemingly good. However, in view of the questionable accuracy of both the analytical and experimental results, these findings still seem questionable.

In attempting to determine the residual stresses in rails, ORE admittedly presented erroneous experimental results in ORE C53 reports 4, 6, and 7. Figure 67 shows the residual σ_z (perhaps the most difficult to determine) stress determined by ORE with three different procedures. In ORE C53 Report 9, more reliable results were obtained and were shown earlier.

In order to determine the three-dimensional residual stresses due to rolling contact, Martin, using his three-dimensional finite element code and 132-lb RE rail head model, computed the stress history for repeated rolling contact in which plastic flow was permitted to occur. Martin assumed that as long as the plastic deformations were not excessive, the plastic and elastic strain fields in the contact region were identical. This assumption was that made by Johnson^[10, 77, 91]. Martin assumed that this was valid for the three-dimensional case as well. While this may be a reasonable assumption, it is yet to be proven. One advantage of the finite element model of Martin, besides the three-dimensionality, was that equilibrium could be re-established after each increment of motion of the plastic strain field. In Figure 68 are shown residual stress contours computed by Martin and Hay for a 132-lb RE rail and a 19,000-lb wheel load. In all cases in which the theoretical shakedown limit was exceeded, steady state plastic flow was attained within 3-5 cycles. This was also observed in the work of Merwin and Johnson^[10]. Figure 69 shows the stress rise with cycles. This was also shown in Figure 68 along with the ORE test results. It would appear that for the limited cycles of Martin and Hay, that the increase in longitudinal stress was similar to that obtained by ORE. Martin and Hay suggest that fatigue failures may be related to the existence of such residual stresses. Martin and Hay's treatment of residual stress in rails remains the most rigorous treatment yet developed.

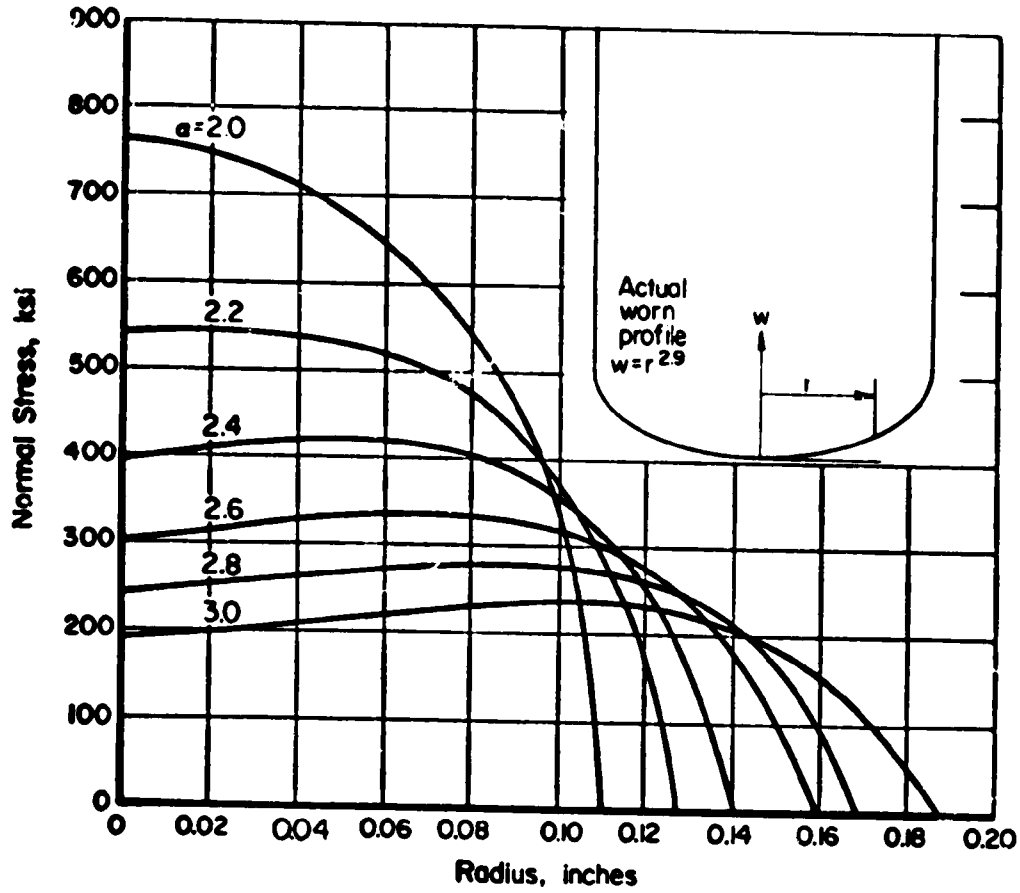


FIGURE 64. CONTACT STRESS DISTRIBUTION BETWEEN INDENTOR HAVING SURFACE CONTOURS IN VARIOUS STAGES OF DEFORMATION OR WEAR $w = r^a$

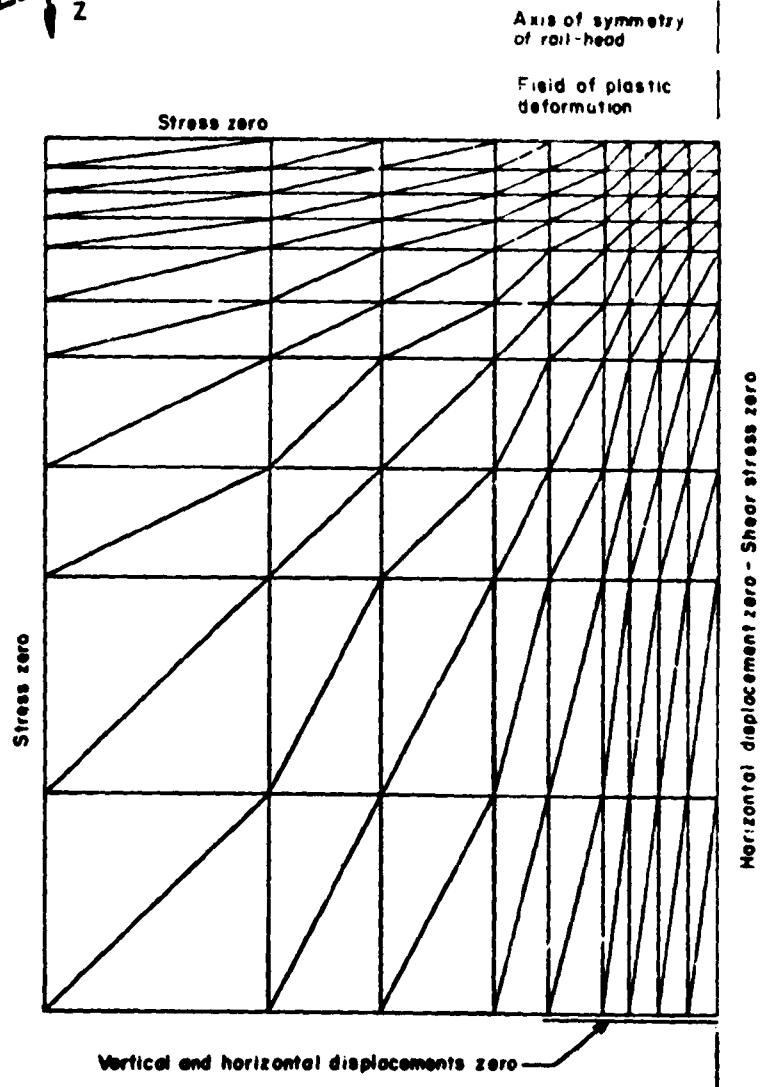
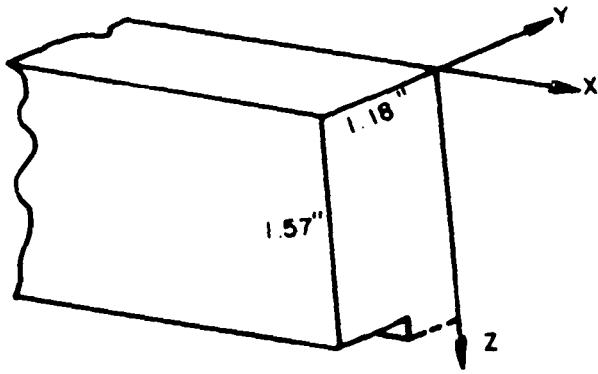


FIGURE 65. FINITE ELEMENT MODEL OF RAIL HEAD (ORE C53/RP9)

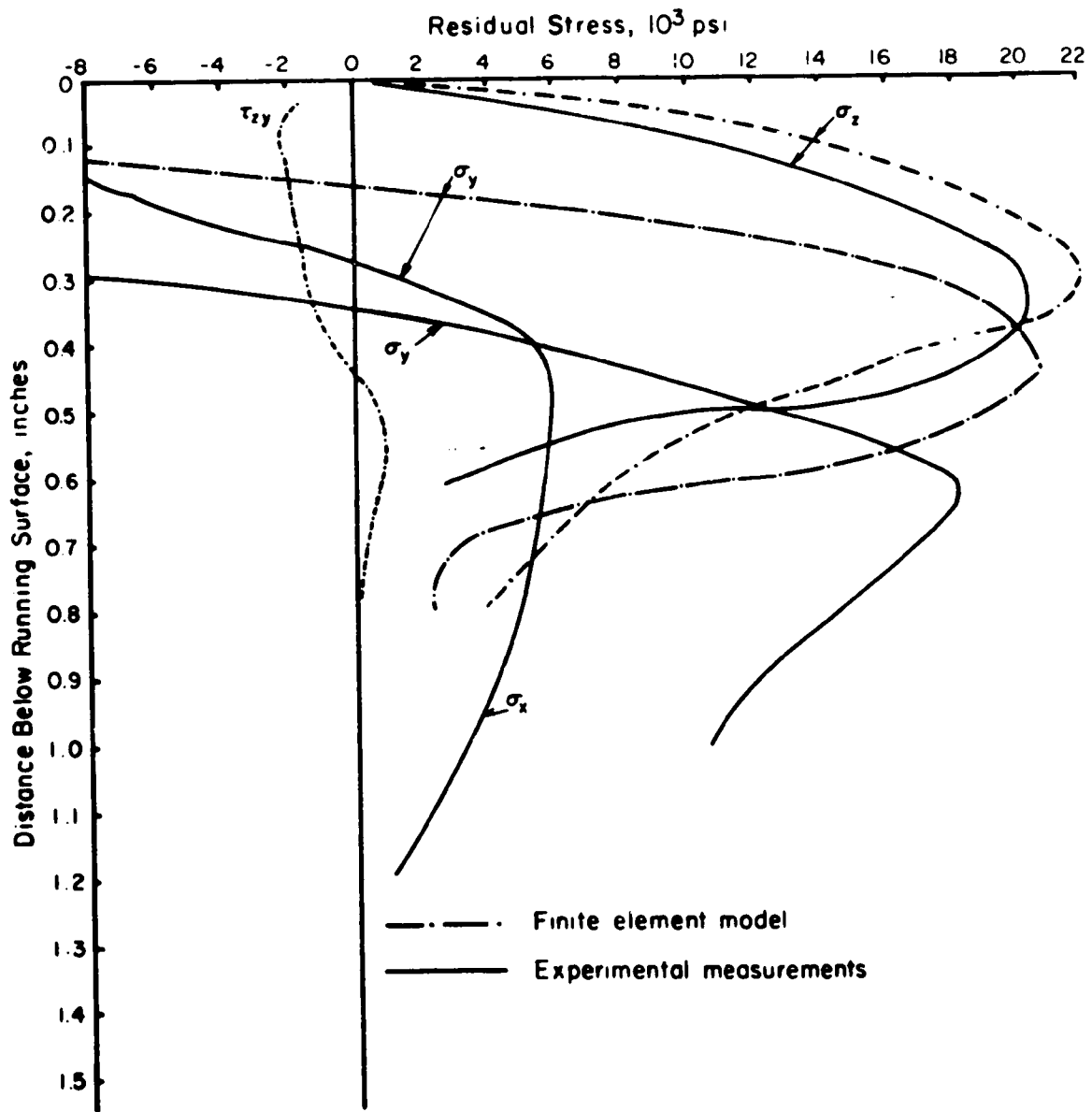


FIGURE 66. RESIDUAL STRESS AS A FUNCTION OF DEPTH BELOW SURFACE (ORE C53/RP9)

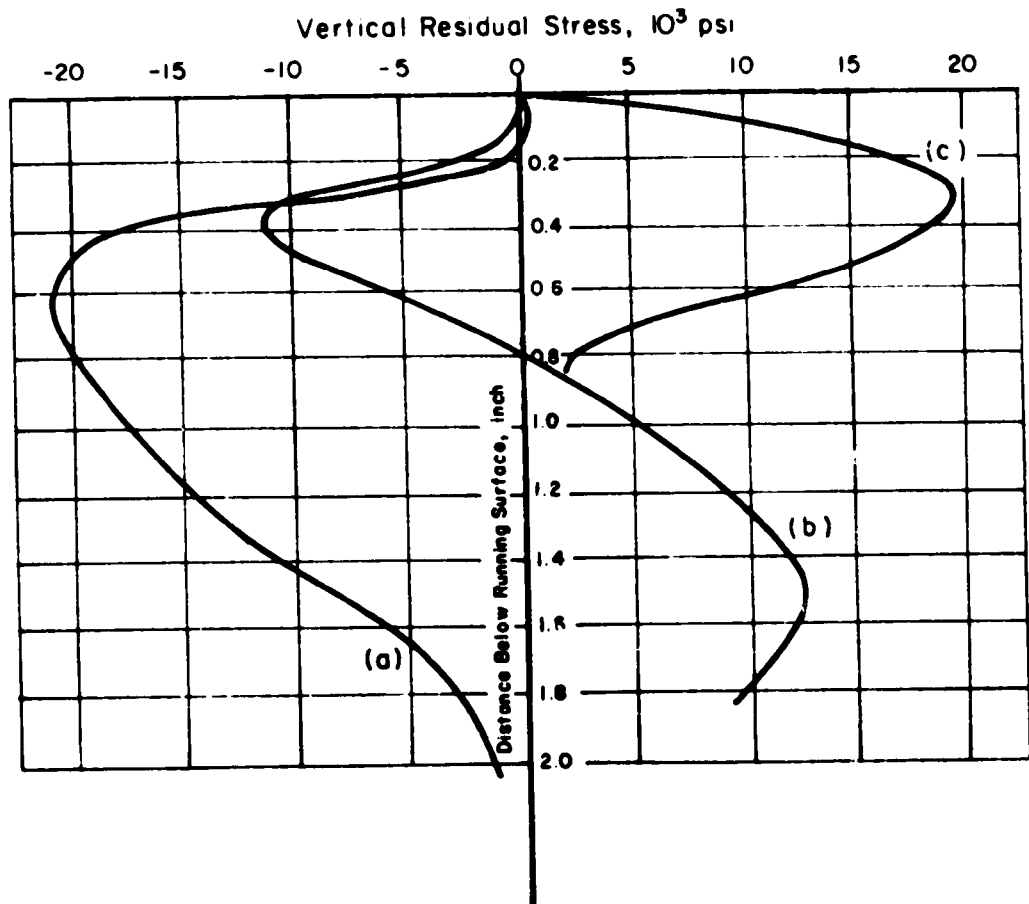
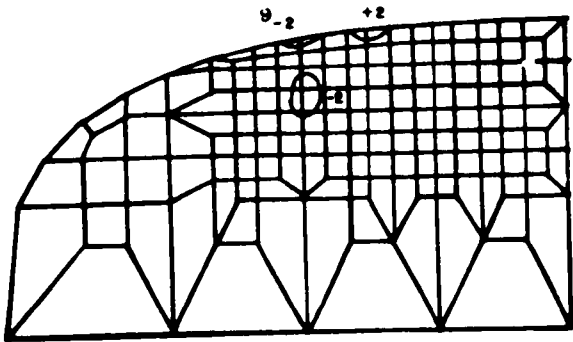
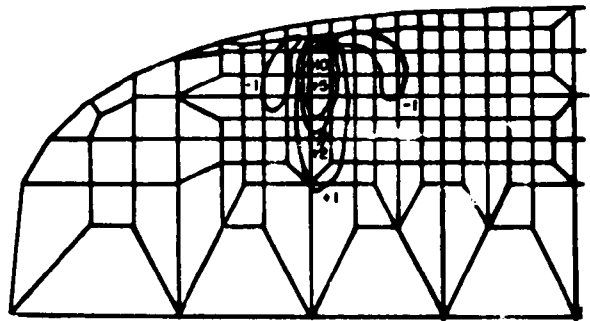


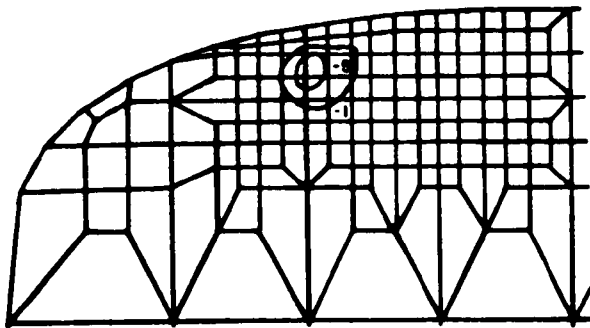
FIGURE 67. RESIDUAL STRESSES DEVELOPED USING (a) STABLIEN, (b) ROSENTHAL-NORTEN, (c) ORE HOLE DRILLING TECHNIQUE.



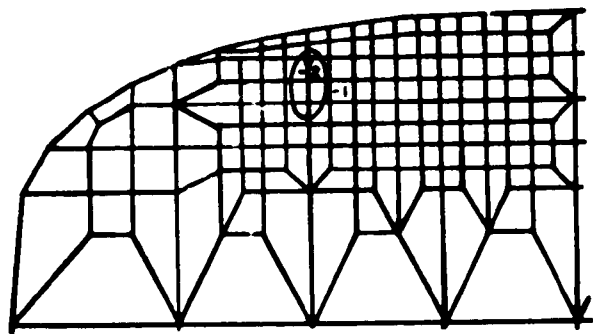
Lateral Stress σ_y (psi)



Vertical Stress σ_z (psi)



Longitudinal Stress σ_x (psi)



Shearing Stress τ_{yz} (psi)

FIGURE 68. RESIDUAL STRESS COMPONENTS IN 132-LB RE RAIL HEAD, $P = 19,000$ LB,
 $K = 55,000$ PSI

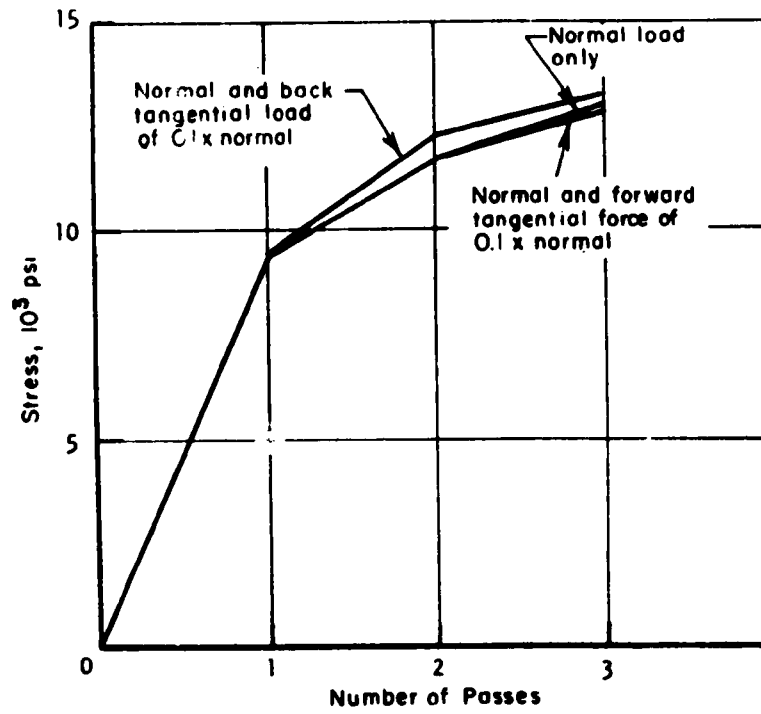


FIGURE 69. BUILDUP OF σ_x RESIDUAL STRESS AT NODE A^[9]

7. A DESCRIPTION OF METHODOLOGY FOR THE DEVELOPMENT OF A RAIL STRESS MODEL

The most important component of a railroad track structure is the rail. It is the hope of the industry that once installed, the rail need only be replaced when it has "worn out". Unfortunately, this is not always the case, and rails frequently fail prematurely. There are many kinds of failures. Typical failures are transverse breaks, horizontal and vertical splits, and breakout of sections of rail at bolted rail joints. Depending on the type of rail failure, the rail should usually be removed from the track at some time after detection to prevent a catastrophe.

Theories, based primarily on experimental analyses of stresses arising from service loads, have been advanced over the last 50 years to account for the development and growth of flaws in rails. A complementary analytical study of stresses in rails has not yet been made. This is necessary to form a comprehensive basis for a quantitative understanding of flaw initiation and growth and for the development of a rail stress model component in an overall reliability model for track structures.

Figure 70 is a flow diagram showing the various components of a track structures reliability model. Also shown are the Tie and Ballast model, Load Environmental Definitions, Material Failure Characterizations, and the Reliability Analysis Component. Across the top of the diagram are shown the variables describing the track structure.

It is planned that the rail stress model be composed of five subcomponents. These subcomponents are described in the following paragraphs.

7.1 FULL RAIL MODEL

This model will be a three-dimensional finite element elastic model of a whole rail section of length, somewhat over two-ties long. The purpose of the model is to develop flexural and thermal stresses in the rail section in regions away from the contact zone, i.e., fillet, web, and base regions. Further, the model will develop boundary conditions for both the rail head model used for residual stress determination and the finite element head model in which the crack analysis is performed.

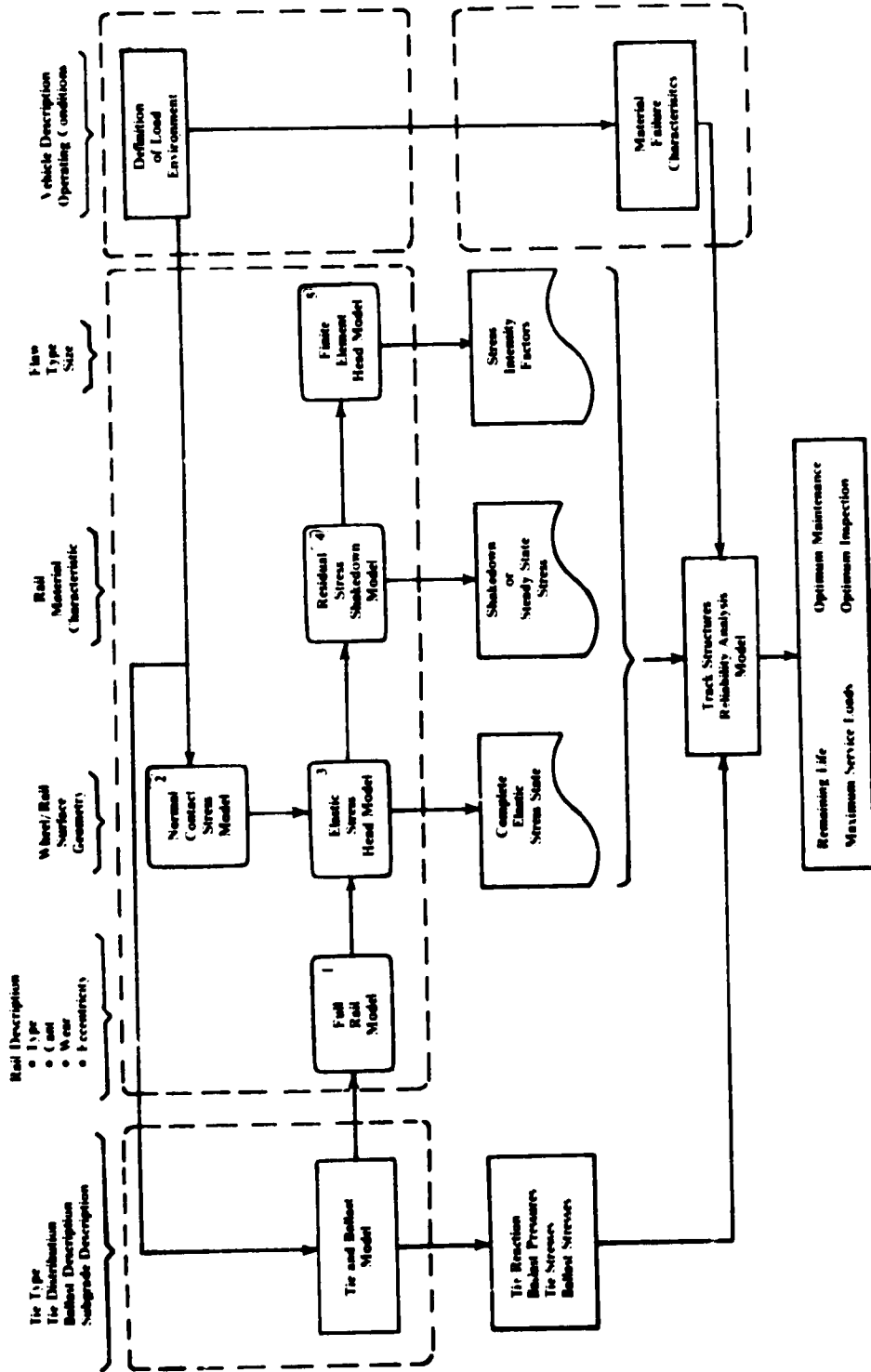


FIGURE 70. FLOW DIAGRAM FOR TRACK STRUCTURES RELIABILITY MODEL

This model will be similar to the model shown in Figure 71 which was used to determine the stresses around bolt holes in the web at a rail end. The full rail model will, however, require meshing down in the fillet regions. Tie reactions and boundary conditions for the full rail model will be obtained from the tie and ballast model. Although the tie and ballast model represents the rail as an elastic beam, beam theory has been found to yield inaccurate results away from the region where additional stresses are introduced into the head by the in-plane compliance of the web and the contact stresses in the vicinity of the contact area.

The computer code to be incorporated for this model is ADINA. This code was an extension of SAP IV which was developed under the direction of Wilson at Berkley and contains 20 node isoparametric elastic brick elements. These elements will facilitate meshing down in the fillet regions.

7.2 NORMAL CONTACT STRESS MODEL

This model will be used to determine the normal stresses at the interface between the wheel and rail where each have arbitrary surface geometry. This normal contact stress is used as input into an elastic head stress model to determine stress throughout the head of the rail. Lateral and longitudinal surface tractions are assumed to be under full slip conditions. The normal contact stress distribution is assumed to be uncoupled from the surface traction distribution.

The surface of the wheel and rail is divided into a regular array of potential contact spots or nodes^[66]. At any node in the proposed zone of contact, the sum of the elastic deformations and any initial separations must be greater than or equal to the rigid body approach. The distribution of pressure over the finite proposed contact zone is represented by a system of discrete forces at the nodes. The sum of all the forces acting at the nodes must balance the component of the applied load normal to the surface. The program utilizes a simplex-type algorithm in solving the system of equations that formulate the general problem of elastic bodies.

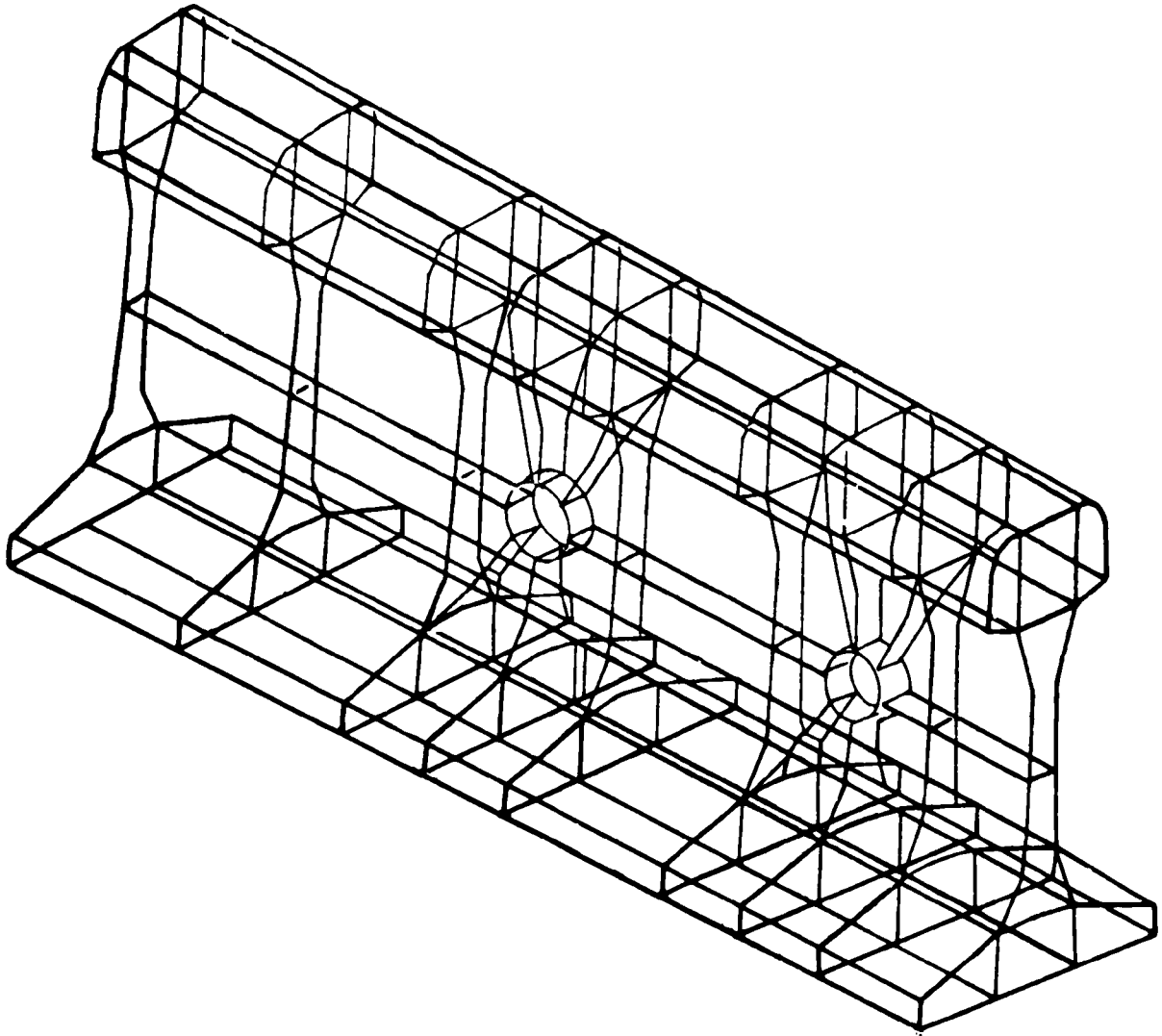


FIGURE 71. THREE-DIMENSIONAL FINITE-ELEMENT MESH OF RAIL END

7.3 ELASTIC AND ELASTIC-PLASTIC HEAD MODELS

The elastic model will be a six-sided elastic brick having the vertical and lateral dimensions of a rail head. The purpose of the model is to develop the complete elastic stress and strain within the rail given the normal contact stress and surface tractions and the boundary conditions at the ends and between the head and web. The solution technique for the model, developed by Bell^[96], assumes the brick to be composed of six half spaces. The boundary conditions are satisfied on the six faces of the brick in the least squares sense. This solution technique has been shown to possess a high degree of accuracy.

It is planned that the elastic head model will model the complete elastic stress state and provide a check on the accuracy of the elastic-plastic finite element model to be used in calculating residual stress shakedown.

The elastic-plastic head model will consist of a three-dimensional ADINA model of the rail head. It will be loaded with Hertzian or non-Hertzian contact stress distributions. The model will be finely enough meshed to provide an accurate description of plastic strain resulting from a stationary central load. The stress-strain description of the rail head will be formulated from actual laboratory data on specimens cut from rails. These data will be represented by a bilinear stress-strain curve.

7.4 RESIDUAL STRESS SHAKEDOWN MODEL

It is planned that this model will enable the residual stresses and shakedown state within the rail head to be determined. The model will use as input for the first cycle of loading, the elastic-plastic strain fields from the finite-element head model. Thereafter, the assumption that during each wheel passage the range of strain is identical to the elastic strain cycle for the same wheel passage will be made.

For the first load cycle the residuals will be assumed to be zero. The head is divided into subintervals Δx thick. The wheel load is moved longitudinally, incrementally a distance Δx at a time. Each

time yielding is checked according to the von Mises criterion. If yielding is found to have occurred, the Prandtl-Reuss flow rules are applied to each point where yielding has occurred. Stresses are cumulatively added. A flow diagram for the procedure is shown in Figure 72. At the end of each passage of the wheel, the stresses in the rail will not be in equilibrium. Nodal force will be calculated to force the body back into equilibrium. The residual stresses will be computed and the procedure repeated for successive cycles. This code will output the residual stresses within the head and the shakedown state, if it exists, to be used directly in the reliability analysis and the cracked head analysis.

7.5 FINITE ELEMENT HEAD MODEL

This will consist of a finite element model of a portion of the rail into which particular crack configurations can be introduced. These cracks are to be characteristic of the three central rail defects shown in Figure 73. It is possible that this model may incorporate both three-dimensional and two-dimensional finite element techniques of determining stress intensity factors for cracks at particular stages of development. These stress intensity factors along with the associated loads would then be input into the reliability analysis model.

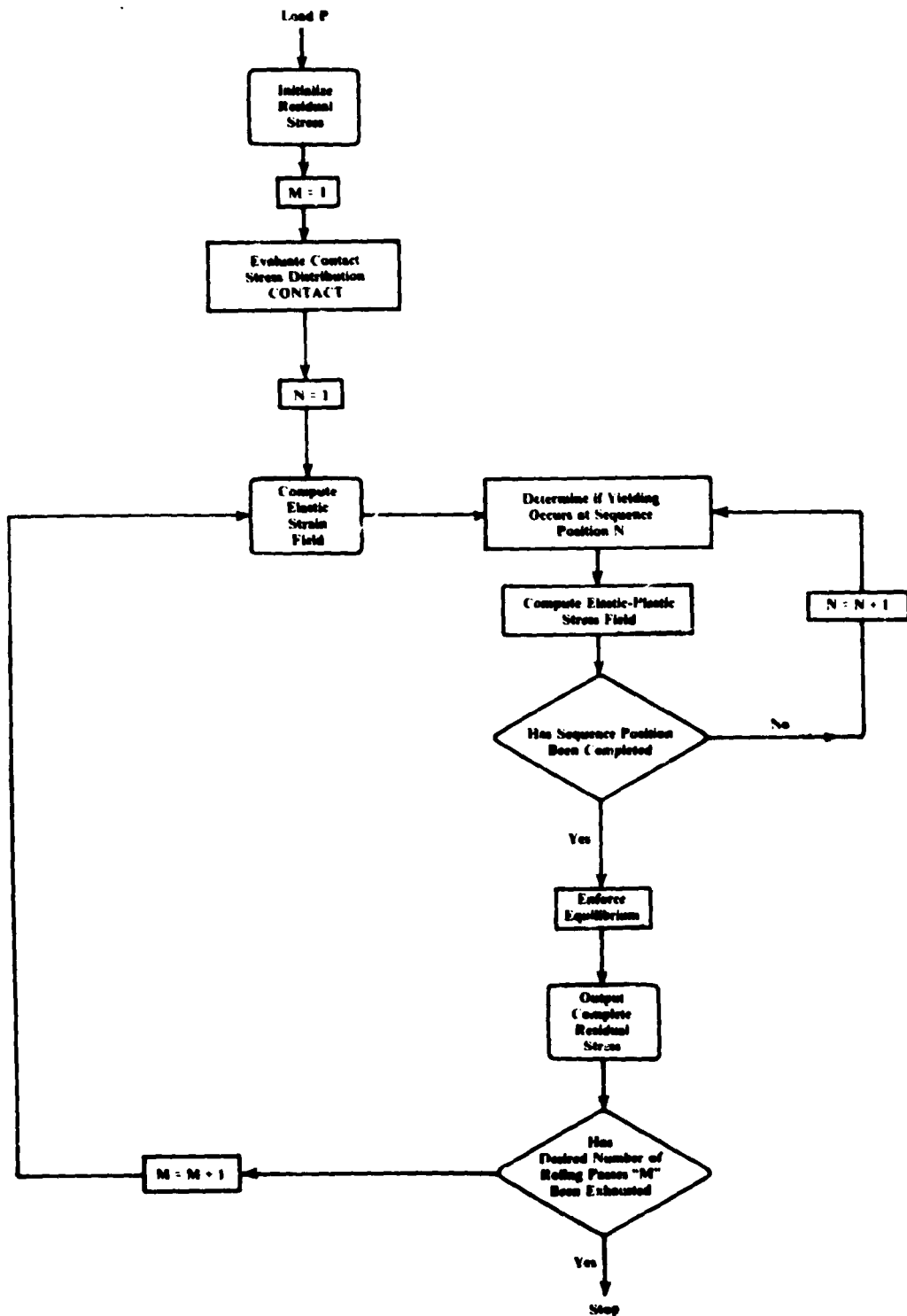
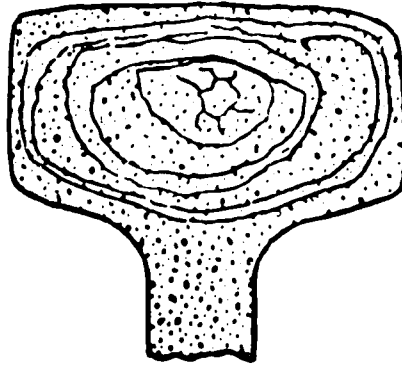
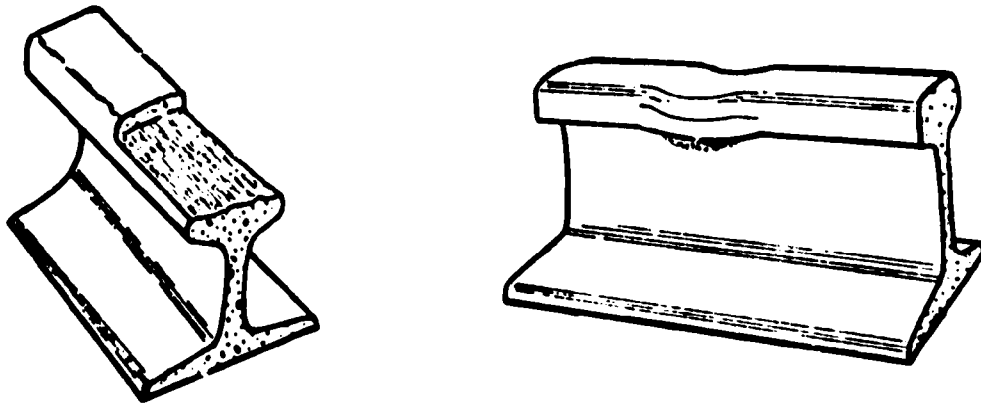


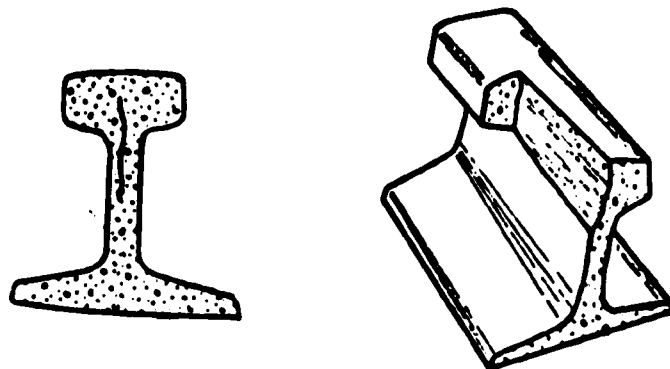
FIGURE 72. LOGIC DIAGRAM OF LOADING SEQUENCES FOR RESIDUAL STRESS RAIL MODEL



a. Rail Head Showing Transverse Fissure Defect



b. Horizontal Split-Head Defect



c. Vertical Split Head

FIGURE 73. CENTRAL RAIL DEFECTS

REFERENCES

- [1] Federal Railroad Administration, "Bulletin No. 141, Summary and Analysis of Accidents on Railroads in the United States," Office of Safety, December 1972.
- [2] NTSB-RSS-74-1, "Broken Rails: A Major Cause of Train Accidents," National Transportation Safety Board, Jan. 1974.
- [3] Railway Track & Structures, Jan. 1974, pp. 18-20.
- [4] O.S. Kecskes, Rail International, September 1972, pp 493-506.
- [5] Summary of Rail Failures, prepared by Sperry Rail Service, 1974.
- [6] "Track Safety Standard," Federal Railroad Administration, Office of Safety, December 22, 1972.
- [7] Rail Defect Manual, Sperry Rail Service, 1964.
- [8] E. I. Radzimovsky, "Stress Distribution and Strength Condition of Two Rolling Cylinders Pressed Together," Univ. Illinois Eng. Expt. Sta. Bull., 408 (1953)
- [9] G. C. Martin and W. W. Hay, "The Influence of Wheel-Rail Contact Forces on the Formation of Rail Shells," Trans. ASME, 72-WA/RT-8, 1972.
- [10] J. E. Merwin and K. L. Johnson, "An Analysis of Plastic Deformation in Rolling Contact," Proc. Symp. Fatigue in Rolling Contact, Vol. 177, No. 24, Inst. of Mech. Engrs., London, England, 1963, pp. 676-688.
- [11] E. Winkler, "Die Lehr von der Elastigkeit und Festigkeit," Verlag H. Dominikus, Prag, 1867.
- [12] J. W. Schwedler, "On Iron Permanent Way," Proceedings, Institution of Civil Engineers, London, 1882, pp. 95-118.
- [13] H. Zimmerman, Die Berechnung des Eisenbahnoberbaues, Verlag W. Ernst & Sohn, Berlin, 1888.
- [14] S. Timoshenko, "Method of Analysis of Static and Dynamical Stresses in Rail," Proceedings of the Second International Congress for Applied Mechanics, Zurich, 1927.
- [15] M. Hetenyi, Beams on Elastic Foundations, University of Michigan Press, 1946.
- [16] "Progress Report on the Special Committee on Stresses in Track," AREA Proceedings, Vol. 18, 21, 24, 26, 31, 35, 42, Chicago, Illinois.

- [17] S. Timoshenko and B. F. Langer, "Stresses in Railroad Track," ASME Transactions, Vol. 54, 1932, pp. 277-293.
- [18] J. Eisenmann, "Stress Distribution in the Permanent Way Due to Heavy Axle Loads and High Speeds," AREA, Bulletin 622, Sept-Oct 1964, pp. 24-59.
- [19] A. D. Kerr, "The Stress and Stability Analyses of Railroad Tracks," Journal of Applied Mechanics, December 1974, pp. 841-848.
- [20] C. W. Clarke, "Track Loading Fundamentals, Parts 1-7," Railway Gazette, 106, 1957.
- [21] R. N. Prause, et al., "Assessment of Design Tools and Criteria for Urban Track Structures," Report No. UMTA-MA-06-0025-74-3, Urban Mass Transportation Administration, July 1974.
- [22] R. Harker, Eisenbahnoberbau, Springer Wien, 1952.
- [23] Y. Weitsman, "On Foundations That React in Compression Only," Journal of Applied Mechanics, Vol 37, No. 4, Trans. ASME, Vol 92, Series E, Dec 1970, pp. 1019-1030.
- [24] J. R. Lundgren, G. C. Martin, and W. W. Hay, "A Simulation Model of Ballast Support and the Modules of Track Elasticity," Univ. of Illinois Exp. Sta., Transportation Series No. 4, 1970.
- [25] M. D. Kilmartin, "A Numerical Discrete Element Analysis of Railroad Track," M.S. Thesis, Tufts University, Nov. 1972.
- [26] A. B. Butler, "An Analysis of Bending Stresses and Deflections in Railroad Rails," M.S. Thesis, University of Illinois, 1969.
- [27] S. Timoshenko and J. M. Lessels, Applied Elasticity, Westinghouse Technical Night School Press, 1925, p. 334.
- [28] T. E. Luco and R. A. Westman, "Dynamic Response of Circular Footings," Engineering Div., U.C.L.A., Los Angeles, April 1971, Report 7113.
- [29] G. L. Nessler, R. H. Prause, and W. D. Kaiser, "An Experimental Evaluation of Techniques for Measuring the Dynamic Compliance of Railroad Track," Interim Report, Contract DOT-FR-3005i, June 1975.
- [30] G. M. Magee and E. E. Cress, "Investigation of the Impact Effect of Flat Wheels," Proc 44th AREA, Vol 45, 1944, pp. 9-23.
- [31] A. Talbot, "1st Progress Report Special Committee in Stresses in Rail Load Track," AREA, Vol 19, 1918, p. 873.
- [32] "Effect of Flat Wheels," Proc. 51st Convention AREA, Vol 53, 1952, pp. 428-448.

- [33] W. Leaf, "Research on Rail Section", Western Metals, September 1947, pp. 20-24.
- [34] M. Mayairi and N. Sasaki, "Two Dimensional Photoelastic Experiments on Several Rail Section," JNR Quarterly Reports, Vol 2, No. 3, 1961.
- [35] "Static Stress Measurements on Five Rails in Special Tangent Track Under Controlled Loading Conditions, Proviso Tests of 1943," Proceedings AREA, Vol 46, 1945, pp. 660-692.
- [36] C. J. Code, "A Method of Calculating the Maximum Stress in the Web of Rail Due to an Essentric Vertical Load," Proc. 46th Convention AREA, Vol 48, 1947, pp. 987-991.
- [37] A. S. Babb, "Experimental Stress Analysis of Rails," Proc Inst. of Mech Engineers, Vol 180, Part 1, No. 41, 1965-1966
- [38] Association of American Railroads, "Engineering Aspects of Current Rail Sections," Report No. ER-15, September 1961.
- [39] A. Wohrl, "Experimental Grundlagen der Thermit-Schrenenschweissung auf freier Strecken," Organ fur die Fortschritte des Eisenbahnwesens, 1927, H.2., p. 23.
- [40] A. D. Kerr, "On the Stability of the Railroad Track in the Vertical Plane," Rail International, Nr. 2, 1974.
- [41] A. D. Kerr, "On the Stability of the Railroad Track in the Horizontal Plane," Princeton University, DOT/FRA Report, December 1974.
- [42] O. H. Varga, "The Thermal Elongation of Rails on Elastic Mountings," Archiv. fur Eisenbahntechnik et the Eisenbahntechnische Rundschau, 1970.
- [43] H. Hertz, "Uber die Beruhring fester elastischer Korper," 1881, reprinted in Gesammelte Werke von Heinrich Hertz, Vol 1, pp 155-173.
- [44] N. M. Belyayev, "Application of Hertz' Theory to the Calculation of Local Stresses at the Contact Point of Wheels and Rails," (in Russian), Vesnik Inzhenerov i Tekh., Memoirs on the Theory of Structures, Petrograd, 1924.
- [45] A. N. Dinnik, "Hertz' Formula and Its Experimental Verification," (in Russian), Zhurnal russk. fiz.-khn. ob-va, fiz., otd., Vol 38, 1906, Part 1, No. 4, pp. 242-249.
- [46] S. Way, "Pitting Due to Rolling Contact," J. Appl. Mech., Vol 2, 1935, pp. 110-114.
- [47] F. Karas, "Werkstoffnaestregung beim Druck Achsenparalleler Walzen nach den gebrauchlichen Festigkeitshypothesen," Forsch. Ingenieurw. Vol 11, 1940, pp. 334-339.

- [48] E. I. Radzimovsky, "Stress Distribution," *op. cit.*
- [49] A. Palmgren and K. Sundberg, "Once Again on the Subject of Ball Bearing Load Capacity," (in Swedish), Tek. Tidskr. (Mekanik), Vol 49, 1919, pp 57-67.
- [50] H. R. Thomas and V. S. Hoersch, "Stresses Due to the Pressure of One Elastic Solid Upon Another," Univ. Illinois Eng. Expt. Sta. Bull., Vol 212, 1930, pp. 54.
- [51] W. Weibull, "Stresses in the Contact of Elastic Bodies," (in Swedish), Tek. Tidskr. (Mekanik), Vol 49, 1919, pp. 16-163.
- [52] G. Lundberg and F. K. G. Odqvist, "Studies on Stress Distributions in the Vicinity of the Contact Region Between Bodies, With Applications," (in Swedish, English Summary), Ing. Vetenskaps Akad. Handl., Vol 116, 1932, pp. 64.
- [53] H. Fessler and E. Ollerton, "Contact Stresses in Toroids Under Radial Loads," Brit. J. Appl. Phys., Vol 8, 1957, pp. 387-393.
- [54] F. B. Seely and J. O. Smith, Advanced Mechanics of Materials, 2nd edition, John Wiley and Sons, 1967, pp. 342-378.
- [55] A. Bazergui and M. L. Meyer, "Embedded Strain Gage for the Measurement of Strains in Rolling Contact," Experimental Mechanics, SESA, 1968, pp. 433-441.
- [56] E. Ollerton, "Stresses in the Contact Zone," Proc Inst. Mech. Engineers, Vol 178, 1964, pp. 161-171.
- [57] H. I. Andrews, "The Creep of Locomotive Driving Wheels, Part I," Rail Engineering International, Vol 5, No. 1, 1975, pp. 8-10.
- [58] C. J. Code, "Wheel Load, Wheel Diameter and Rail Damage," AREA Proceedings, Vol. 39, 1938, p. 839.
- [59] B. Paul, "Review of Wheel Rail Contact Stresses," Symposium on Railroad Track Mechanics, Princeton, April 21-23, 1975.
- [60] C. Storey, "Contact Between Wheel and Rail," Bulletin of the International Railway Congress, Vol. 34, No. 6, June 1957, pp. 434-441.
- [61] M. Srinivasan, Modern Permanent Way, Smaiya Publications, PVT LTD, Bombay, 1969.
- [62] E. Buckingham, "Surface Fatigue of Plastic Materials," Trans. ASME, Vol. 66, May 1944, pp. 297-306.

- [63] M. M. Frocht, "A Three-Dimensional Photoelastic Study of Contact Stresses in the Head of a Model of a Railroad Rail," Proc. S.E.S.A., 1956, Vol. 14, No. 1.
- [64] M. M. Frocht and B. C. Wang, "A Three-Dimensional Photoelastic Study of Interior Stresses in the Head of a Railroad Rail in the Region Under a Wheel," ASME Proc. Fourth U.S. Congress of Applied Mechanics, Vol. 1, 1962, pp. 603-609.
- [65] T. F. Conry and A. Seireg, "A Mathematical Programming Method for Design of Elastic Bodies in Contact," J. Appl. Mech., 70 WA/APM-52, 1970.
- [66] T. G. Johns and A. W. Leissa, "The Normal Contact of Arbitrarily Shaped Multilayered Elastic Bodies," Symposium on the Contact of Deformable Bodies, IUTAM, Univer. of Twente, Enschede, August, 1974.
- [67] T. G. Johns, et al., "Design Analysis of Roller-Track System for Large Steerable Antenna," Report to U.S.N.R.L., by Battelle Memorial Institute, May 11, 1973.
- [68] K. Singh and B. Paul, "Numerical Solution of Non Hertzian Elastic Contact Problems," Jour. Appl. Mech., Trans ASME, 73-WA/APM-11, 1974.
- [69] J. Kannel, "Comparison Between Predicted and Measured Axial Pressure Distribution Between Cylinder," Trans. ASME Journ. Lubricating Technology, July 1974, pp. 508-514.
- [70] F. W. Carter, "On the Action of a Locomotive Driving Wheel," Proc. Roy. Soc., London, Vol. 117, October 1926, pp. 151-157.
- [71] R. D. Mindlin, "Compliance of Elastic Bodies in Contact," J. Appl. Mech., Vol. 16, 1949, pp. 259-268.
- [72] H. Poritsky, "Stresses and Deflections of Cylindrical Bodies on Contact with Application to Contact of Gears and of Locomotive Wheels," J. Appl. Mech., Vol 72, 1950, pp. 191-201.
- [73] K. L. Johnson, "Surface Interaction Between Elastically Loaded Bodies Under Tangential Forces," Proc. Roy. Soc. A, Vol. 230, 1955, pp. 531-549.
- [74] K. L. Johnson, "Energy Dissipation at Spherical Surfaces in Contact Transmitting Oscillating Forces," J. Mech. Engr. Sci., Vol 3, No. 4, 1961, pp. 362-369.
- [75] K. L. Johnson, "Tangential Traction and Micro-slip in Rolling Contact," included in Rolling Contact Phenomena, T. Bidwell, editor, Elsevier, ASME, 1962, pp. 6-28.

- [76] K. L. Johnson, "A Shakedown Limit in Rolling Contact," Proceedings Fourth U.S. National Congress Applied Mechanics, ASME, Berkeley, California, 1962, pp. 971-975.
- [77] K. L. Johnson and Jefferis, J. A., "Plastic Flow and Residual Stresses in Rolling and Sliding Contact," Proc. Symp. Fatigue in Rolling Contact, Inst. Mech. Engrs., (London) Vol. 177, 1963, p. 95.
- [78] D. J. Haines and E. Ollerton, "Contact Stress Distributions on Elliptical Contact Surfaces Subjected to Radial and Tangential Forces," Proc. Inst. Mech. Engrs., (London), Vol. 177, 1963, p. 95.
- [79] J. J. Kalker, "Rolling With Slip and Spin in the Presence of Dry Friction," Wear, 1966, p. 20.
- [80] V. C. Mow, P. L. Chow, and F. F. Ling, "Microslip Between Contacting Paraboloids," J. Appl. Mech., June 1967, pp. 321-327.
- [81] J. O. Smith, Chang Keng Lui, "Stresses Due to Tangential and Normal Loads on an Elastic Solid with Application to Some Contact Stress Problem," Trans. ASME, J. Appl. Mech., Vol. 75, No. 6, June 1953, pp. 157-166.
- [82] G. M. Hamilton, "The Stress Field Created by a Circular Sliding Contact," J. Appl. Mech., Vol. 33, 1966, pp. 371-376.
- [83] B. R. Lawn, "Partial Cone Crack Formation in a Brittle Material Loaded with a Sliding Spherical Indenter," Proc. Roy. Soc. A, Vol. 299, 1967, pp. 307-316.
- [84] G. M. Hamilton and L. E. Goodman, "The Stress Field Created by a Circular Sliding Contact," J. Appl. Mech. Trans ASME, June 1966, pp. 371-376.
- [85] R. Nakamura, et al., "The Rail Shelly Crack in Japan," Quarterly Report RTRI, Vol. 6, No. 3, 1965, pp. 34-44.
- [86] Office for Research and Experiments of the International Union of Railways, "Study of Fatigue Phenomena of the Rail in the Contact Zone with the Wheel," Rail International, Vol. 3, No. 13, September 1973, pp. 741-794.
- [87] W. S. Hyler and H. J. Grover, "The Study of Simulated Rails Under Repeated Rolling Loads," Final Report to AAR and AISI, Battelle Memorial Institute, Aug 31, 1953.
- [88] N. J. Alleman, "Effect of Wheel Size," AREA Bulletin 453, June 1945, pp. 3-8.

- [89] N. J. Alleman, "The Effect of the Ratio of Wheel Diameter to Wheel Load on Extent of Rail Damage," Proc. 45th Convention AREA, Vol. 47, 1946, pp. 725-741.
- [90] J. O. Almen, "Effects of Residual Stresses on Rolling Bodies," included in "Rolling Contact Phenomena," Edited by J. B. Bidwell, Elsevier, AMSE, 1942, pp. 400-424.
- [91] K. L. Johnson, "A Shakedown Limit in Rolling Contact," op. cit.
- [92] A. W. Crooks, Proc. Inst. of Mech. Engineers, London, Vol. 171, 1957, p. 187.
- [93] A. Mendelson, Plasticity: Theory and Application, Macmillan Co., New Yor, 1968, p. 109.
- [94] R. J. Pomeroy, K. L. Johnson, "Residual Stresses in Rolling Contact," J. Strain Analysis, Vol. 4, No. 3, 1969, pp. 208-218.
- [95] C. Hardy, "Contraintes et Deformations au Contact de Corps Bombs Elasto-Plastiques Changes Normalement au Repos et en Roulement," Ph.D. dissertation, Department Engr. Mech., Univ. of Laval, 1970.
- [96] J. C. Bell and S. K. Bartra, "An Approximate Method for Evaluating Stresses Caused by an Arbitrary Pressure Distribution on the Surface of an Elastic Half Space," Surface Mechanics, ASME, 1974, pp. 144-163.
- [97] T. G. Johns, "The Stress Field Generated in an Elastic Layer by Normally Loaded, Periodically Spaced Circular Contacts," J. Lubrication Technology, ASME, 1974, Paper No, 74-Lub-G.

APPENDIX - REPORT OF INVENTIONS

This report contains a comprehensive review of the current information on the stresses to which railroad rails are subjected in service. We believe that this represents a unique compilation of data important to the safety and performance of rails. However, after a diligent review of the work performed under this contract, it is believed that no patentable innovation, improvement or invention was made.

310 copies